Synchrotron Based *Operando* Methods for Characterization of Non-Aqueous Rechargeable Battery Electrode Materials

Jonas Sottmann

Dissertation for the degree of Philosophiæ Doctor

Department of Chemistry
Faculty of Mathematics and Natural Sciences

University of Oslo

31st January 2017

Series of dissertations submitted to the
Faculty of Mathematics and Natural Sciences, University of Oslo
No. 1834

ISSN 1501-7710

Cover: Hanne Baadsgaard Utigard.
Print production: Reprosentralen, University of Oslo.

To my grandfather,
Georg Gerhardt Freund.

Acknowledgements

During the last four years, in which I conducted the research presented in this dissertation, I have been shown great signs of support from many colleagues and friends whom I would like to thank here.

I am sincerely grateful to my supervisors Helmer Fjellvåg (University of Oslo (UiO)), David Wragg (UiO) and Sabrina Sartori (UiO) for allowing me to work independently and letting me explore freely while providing me with the necessary support and guidance whenever needed. In particular I am grateful to David Wragg for his great commitment. I also thank my former supervisor Serena Margadonna (now working at Swansea University) for initiating this project.

My special thanks to Hermann Emerich with whom I designed the *operando* electrochemical cells and the sample changer at the Swiss-Norwegian Beamlines (SNBL) at the European Synchrotron (ESRF, Grenoble) and for his outstanding support and help during many beamtimes so that we could bring back the best possible data to Oslo. I am also grateful to Wouter van Beek (SNBL) for his help during beamtimes and for his valuable suggestions regarding the alignment of the *operando* cells during measurements. My sincere thanks to Christina Drathen for advice in many aspects and help with the collection of high resolution powder patterns at beamline ID22 at ESRF. I thank Roberto Homs-Regojo (ESRF) for his advice with the python battery readout code and for writing the interfacing software for the *operando* battery measurements. I am grateful to Geir Wiker (SNBL) for building many prototype cells and the sample changer. I am also grateful to Per-Olav Korsmo (UiO) for building more cells and many tools for the home laboratory. I further thank Elijah J. Aller for preparing all that useful glassware for

our laboratory.

I thank Fleur Legrain (University of Singapore) and Sergei Manzhos (University of Singapore) for the fruitful collaboration on the amorphous carbon. I also thank Sébastien Sallard (Paul Scherrer Institute, Villigen) for valuable suggestions regarding the analysis of the Prussian blue system.

My sincere thanks to my colleagues at UiO: Matthias Herrmann for extended discussions of various electrochemical systems and help during experiments; Fabian Bernal for going through the ups and downs of PhD-life side by side and for providing me with the Prussian blue samples; Kirill Yusenko for valuable discussions, suggestions and help; Pushpaka Samarasingha for introducing me to electrochemistry when I started with sodium-ion batteries at UiO and collaborating with me on the spinel system; Amund Ruud, Yang Hu, Fredrik Lundvall and Georgios Kalantzopoulos for their assistance on numerous occasions (especially the late night assistance during beamtimes shall be acknowledged here); Kristian B. Lausund for collecting SEM images and EDX maps of the Bi metalate samples; and Ponniah Vajeeston for providing theoretical analysis of Bi-based systems. I thank Ole-Bjørn Karlsen for providing practical advice and supply of equipment and materials in urgent situations.

I am grateful to Johan Taftø for his support and advice long after supervising me during my Master project.

My special thanks to Matthias S., Thomas, Anke, Pim, Danka, Mari W., Martin, Mari K., John, Alex, Amélie, Guillaume, Aline, les Féraux, Sven, Max, Laura, Andreas, Tim and Felix for sharing many passions and for lending me an ear in difficult situations. I am grateful for the *energi fotball* sessions providing a place where to discharge and charge energy simultaneously and the enjoyable soup lunches in our group.

I am deeply grateful to Solène for her support and love. I also thank my family for their confidence and support.

Funding was received from the University of Oslo. This work was also supported by the synchrotron and neutron travel grant (Research Council of Norway, No. 216625). I thank ESRF and SNBL for granting beamtime. I acknowledge use of the Electrochemistry Laboratory at ESRF and the Norwegian national infrastructure for X-ray diffraction and Scattering (RECX).

Adjudication committee

The adjudication committee for the evaluation of this dissertation has had the following members:

- Dr. Laurence Croguennec, Institut de la Matière Condensée de Bordeaux, CNRS / Université de Bordeaux, France.
- Dr. Valerie Pralong, CRISTMAT, CNRS, Caen, France.
- Prof. Harald Walderhaug (administrator), Department of Chemistry, University of Oslo, Norway.

Abstract

Rechargeable non-aqueous lithium-ion batteries (LIBs) are central to our way of life. They are the power source of choice for portable devices and electric vehicles. The technology is likely to become even more important as the use of intermittent renewable energy increases and electrochemical energy storage could serve a broad range of grid scale applications to balance energy supply and demand. Limited and locally restricted Li resources may, however, be insufficient for the massive deployment of LIB technology. In this respect sodium-ion batteries (SIBs) may become a promising alternative to LIBs. The wide-spread abundance and low cost of Na makes this technology particularly attractive. Similarities in Li and Na chemistries should facilitate a fast and cost effective scale up of SIB technology. While the LIBs have been intensely investigated since the early 1960s, huge research efforts are currently under way to find and develop suitable SIB materials. This has been the topic of the four research papers of this dissertation, with respect to measurement techniques and materials.

Understanding the working and degradation mechanisms of electrode materials at the atomic scale is fundamental to optimize battery materials. The key to this is investigation *in situ* during operation (also called *operando*). For this purpose a fully operational set-up (electrochemical cells, sample changer and interfacing software) that enables combined quasi-simultaneous *operando* X-ray diffraction (XRD) and X-ray absorption (XAS such as XANES and EXAFS) measurements coupled with electrochemical characterization was developed. The combined approach of *operando* XRD and XAS enables deep insights into electrochemical reaction processes (*e.g.* insertion, alloying, conversion), structural stability (*e.g.* pulverization, amorphization) and

voltage-composition profiles (single phase *vs.* multi-phase) along with details on the oxidation state and the local environment of the redox-active species.

In this dissertation the working and degradation mechanisms of several SIB electrode materials were studied with the emphasis on negative electrode (anode) materials. Various material-related properties such as vacancy and water content, crystallite size and nanostructuring were found to affect the structural chemistry during cycling, which was put into context with the electrochemical properties of the battery system.

Desodiation and sodiation of the Prussian blue analogue $Na_{1.32}Mn[Fe(CN)_6]_{0.83} \cdot z\,H_2O$ in a sodium cathode were found to follow different routes which gives rise to pronounced differences in the galvanostatic charge and discharge profiles. The presence of $[Fe(CN)_6]$ vacancies and water results in capacity degradation due to the formation of an electrochemically inactive residual phase.

Sodiation and desodiation of microcrystalline Bi as an alloying anode material for SIBs follows the reaction path predicted by the equilibrium phase diagram. Low cycling stability is attributed to pronounced breaking-up (pulverization) of the microcrystalline Na−Bi alloy particles which leads to formation of inactive residual phases. Nanocrystalline Bi on the other hand shows much more stable cycling behaviour because a deviation in the structural chemistry from the equilibrium reaction path gives rise to smoother structural transformations.

The conversion anode material Bi_2S_3 was found to form nanocrystallites of Bi which are further alloyed with Na during the initial sodiation. During further cycling agglomeration of the Bi particles gives rise to a reduction of the active surface area which leads to loss of the reversibility of the conversion reaction.

Ternary metalates such as $BiVO_4$ and $Bi_2(MoO_4)_3$ were identified as a novel class of high performance SIB anode materials. During the first cycle the initial compounds are converted into alloying Bi nanocrystallites confined in a matrix of electrochemically active insertion hosts ($Na_{3+x}VO_4$ and $Na_{2+x}(MoO_4)$, respectively). The nanostructured composite anode thus obtained enables excellent high rate performance and very stable capacity retention over hundreds of cycles.

List of research papers

The main findings of this dissertation are presented on the basis of the following four main research papers which can be found in Appendix A. These *operando* X-ray studies of sodium ion battery materials, with an emphasis on anode materials, are summarised, discussed and viewed within a larger frame of reference in Chapter 5.

I **Versatile electrochemical cell for Li-/Na-ion batteries and high-throughput setup for combined *operando* X-ray diffraction and absorption spectroscopy**
J. Sottmann, R. Homs-Regojo, D. S. Wragg, H. Fjellvåg, S. Margadonna, H. Emerich
J. Appl. Crystallogr. **2016**, 49, 1972-1981

II ***In operando* Synchrotron XRD/XAS Investigation of Sodium Insertion into the Prussian Blue Analogue Cathode Material $Na_{1.32}Mn[Fe(CN)_6]_{0.83} \cdot z\ H_2O$**
J. Sottmann, F. L. M. Bernal, K. V. Yusenko, M. Herrmann, H. Emerich, D. S. Wragg, and S. Margadonna
Electrochimica Acta **2016**, 200, 305–313

III **How Crystallite Size Controls the Reaction Path in Nonaqueous Metal Ion Batteries: The Example of Sodium Bismuth Alloying**
J. Sottmann, M. Herrmann, P. Vajeeston, Y. Hu, A. Ruud, C. Drathen, H. Emerich, H. Fjellvåg, and D. S. Wragg
Chem. Mater. **2016**, 28, 2750-2756

IV **A new route to stable alloying anodes for sodium-ion batteries**
J. Sottmann, M. Herrmann, P. Vajeeston, A. Ruud, C. Drathen, H. Emerich, D. S. Wragg, and H. Fjellvåg
Manuscript

In addition, I have contributed to the following two research papers which are appended in Appendix A. These works are related to other aspects of non-aqueous rechargeable batteries, in terms of the metal ion system (Li instead of Na) and/or the methods used to study their working mechanisms. These supplementary research papers are relevant but not central to the main findings of this dissertation. They are therefore summarised, discussed and put into a broader context in Chapter 6.

V ***In situ*** **synchrotron study of** ***ordered*** **and** ***disordered*** **$LiMn_{1.5}Ni_{0.5}O_4$ as lithium ion battery positive electrode**
P. B. Samarasingha, J. Sottmann, S. Margadonna, H. Emerich, O. Nilsen, H. Fjellvåg
Acta Mater. **2016**, 116, 290-297

VI **Amorphous (Glassy) Carbon, a Promising Material for Sodium Ion Battery Anodes: a Combined First-Principles and Experimental Study**
F. Legrain, J. Sottmann, K. Kotsis, S. Gorantla, S. Sartori, and S. Manzhos
J. Phys. Chem. C **2015**, 119, 13496-13501

My contributions to the research papers

I Contributing to the design of *operando* electrochemical cell and sample changer; programming of the python readout code and contributing to the interfacing software; commissioning of the set-up; planning and conducting experiments, data analysis and interpretation; heading the writing process of the manuscript.

II Planning and conducting experiments; data analysis and interpretation; heading the writing process of the manuscript.

III Synthesis; planning and conducting experiments; data analysis and interpretation; heading the writing process of the manuscript.

IV Synthesis; planning and conducting experiments; data analysis and interpretation; heading the writing process of the manuscript.

V Planning and conducting the *operando* measurements; data analysis and interpretation; and thereby contributing to the writing process.

VI Conducting experimental electrochemical work; interpretation of experimental data and comparison to theoretical work; and thereby contributing to the writing process.

Abbreviations

AFM atomic force microscopy. 59

C_{SP} carbon black, Timcal Super P. 77, 78
CAES compressed air energy storage. 3
CMC carboxymethyl cellulose. 46, 47
CNT carbon nanotube. 46
CV cyclic voltammetry. 80

DEC diethyl carbonate. 24, 79
DEMS differential electrochemical mass spectrometry. 60
DFT density functional theory. 77, 103
DMC dimethyl carbonate. 24, 25, 79

EC ethylene carbonate. 24, 25, 79
EELS electron energy loss spectroscopy. 59
ESRF European Synchrotron. 80–82, 87
EV electric vehicle. 4, 5, 28, 33, 84
EXAFS extended X-ray absorption fine structure. 9, 54, 69–74, 81, 86, 87, 92, 105, 108, 117, 118

FEC fluoroethylene carbonate. 34, 46, 47, 79
FTIR Fourier transform infrared spectroscopy. 60, 112

HOMO highest occupied molecular orbital. 24, 26
HS high-spin. 41

LIB lithium-ion battery. 4–7, 10, 14–16, 21, 22, 24–26, 29, 33, 34, 37, 43, 48, 50, 51, 60, 79, 83–86, 92, 109, 111, 112, 119, 121
LS low-spin. 41
LUMO lowest unoccupied molecular orbital. 24, 25

NMR nuclear magnetic resonance spectroscopy. 54, 55, 60, 109

P23 Fritsch Mini-Mill Pulverisette 23. 77, 78
P7 Fritsch Planetary Micro Mill Pulverisette 7. 78
PAA poly(acrylic acid). 46, 78
PBA Prussian blue analogue. 9, 40–42, 77, 78, 80, 86, 92–95, 105

PDF pair distribution function. 108

PE polyethylene. 80

PFM poly(9.9-dioctylfluorene-co-fluorenone-co-methylbenzoic ester). 47

PTFE polytetrafluoroethylene. 77, 78, 95

RECX Norwegian National Resource Centre for X-ray Diffraction and Scattering. 82

SAXS small angle X-ray scattering. 54

SEI solid electrolyte interface. 25–27, 44, 46, 60, 109, 121

SEM scanning electron microscopy. 59

SIB sodium-ion battery. 6–10, 16, 24, 26, 29, 33–35, 37, 40, 42, 43, 48, 50, 51, 83–86, 92, 96, 97, 101, 104–106, 109, 111, 119, 120

SNBL Swiss-Norwegian Beam Lines. 81, 82, 87, 90, 108

TEM tunneling electron microscopy. 59, 60, 77, 109, 110, 112

TOPAS TOPAS V4.2/V5, Bruker AXS. 81, 82

VC vinylene carbonate. 25

XANES X-ray absorption near edge spectroscopy. 9, 54, 57, 69–72, 81, 86, 87, 92, 93, 100, 103, 105, 108, 117, 118

XAS X-ray absorption spectroscopy. 9, 54, 55, 60, 61, 68, 69, 71, 81, 82, 86, 87, 92, 100, 105, 106, 108, 116, 118

XRD X-ray diffraction. 8, 9, 53, 55, 58, 61, 63, 67, 80–82, 86, 87, 91–96, 98, 100, 101, 103, 105–109, 112–114, 116–119

Contents

Chapter 1

Motivation

Future energy security depends on the availability of the diminishing fossil fuel reserves and their replacement by renewable energy sources. A transition to renewable energy is further highly desirable in order to reduce greenhouse gas emissions which are held responsible for global warming and associated sea level rises. Many countries promote implementation of renewable energy sources with the intention of reducing their dependence on imported oil and gas as well as meeting environmental policy objectives. One of the great challenges in the transition towards an energy system with a high share of weather dependent, and thus intermittent, renewable energy sources (such as solar and wind power) is to balance energy supply and demand in an economically viable manner. Energy storage has the potential to buffer the surplus energy production by storing and releasing energy when required, and will therefore play a key role in the advancement of renewable energy production.

Energy storage technologies and systems are diverse. They include storing mechanical energy such as pumped hydroelectric, compressed air and flywheel energy storage; chemical energy in chemical fuels such as hydrogen using fuel cell technology; thermal energy in form of sensible heat, latent heat and thermoreversible chemical reactions; electrochemical energy in batteries; and electrical energy such as supercapacitors and superconducting magnetic energy storage [2, 3]. Electrical energy storage systems can be implemented in distributed and centralized manners on small and large scales independent

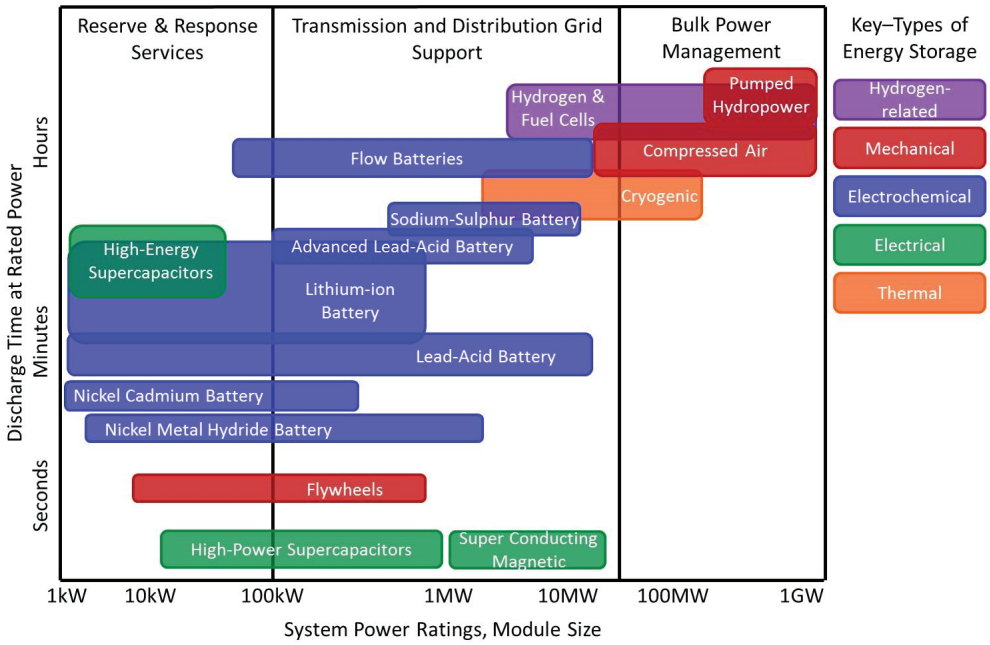

Figure 1.1: Suitability of different electrical energy storage technologies for grid-scale applications. Adapted from [1].

of and throughout the electricity grid. The various electrical energy storage systems have different power ratings and provide storage services at time scales ranging from seconds to years as compared in Figure 1.1. They could thus provide a broad range of beneficial grid-scale services. These include voltage and frequency regulation to ensure grid stability and power quality (seconds to minutes); peak shaving and load shifting (minutes to hours) to improve the efficiency of the energy system; and black start provision [3, 4]. Adding energy storage to the electricity grid furthermore reduces the dependency on energy imports and can potentially save cost by deferring oversized upgrades of distribution and transmission infrastructure [4]. Energy storage in conjunction with local generation enables the formation of micro-grids which are connected to the national electricity grid. For remote areas islanded micro-grids might be favourable with respect to the cost of transmission infrastructure.

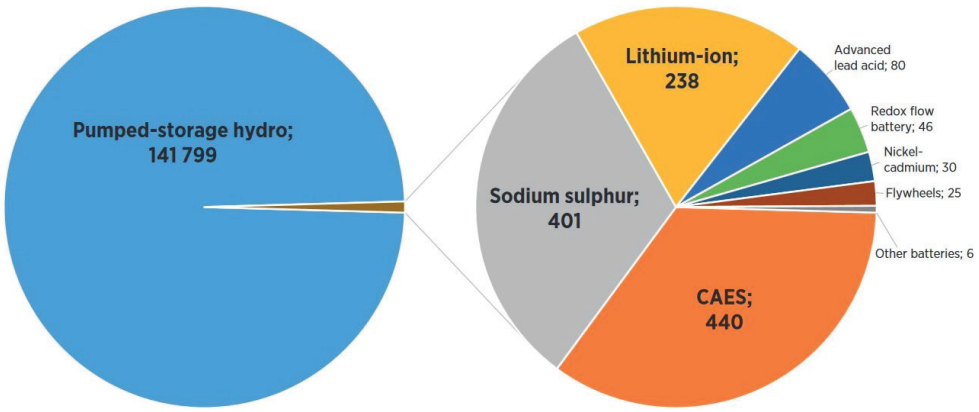

Figure 1.2: Share of energy storage technologies (in MW) in the global electrical energy storage system in 2015 [9].

The different electrical energy storage technologies have different properties and therefore aim to deliver different grid services. Their primary grid-scale applications, state of the art and current challenges were summarised in [3–6]. The most effective approach to introduce and implement electrical energy storage may thus be based on a combination of several electrical energy storage technologies. While some of these technologies are mature or near maturity, many are still under development [4, 7]. Considerable investment costs have to date restricted the implementation of energy storage for balancing consumption and production, but the situation is likely to change as storage costs fall and emphasis on grid stability increases [6, 8].

The current energy storage landscape is depicted in Figure 1.2. While pumped hydroelectric and compressed air energy storage (CAES) are geographically restricted, other technologies allow for scalable and distributed storage. Electrochemical energy storage in batteries possesses a number of desirable features, including high round-trip efficiency, flexible power and energy characteristics to meet different grid services, long cycle life, and low maintenance [5]. Their modular and scalable nature makes them well suited for voltage and frequency regulation and energy storage directly at wind and photovoltaic power stations or in stationary district storage. The main installed stationary electrochemical storage types are high temperat-

ure sodium-sulphur, lithium-ion, advanced lead-acid and flow batteries [3, 9]. Among them lithium-ion battery (LIB) technology has been one of the fastest developing battery technologies over the last decades. The trend in recent stationary battery storage installations is towards LIBs, due to cost and performance advantages over the other battery types [10].

Since their market introduction by Sony in the early 1990s LIBs have become the power source of choice in portable devices and power tools due to their superior power and energy densities, as well as affordable and still decreasing costs. LIBs are therefore also considered the most promising battery technology for powering the next generation of electric vehicles (EVs). Electrification of the transport sector (*e.g.* cars, buses, ferries, trains and planes [11–13]) helps improve local air quality and to reduce greenhouse gas emissions as well as dependency on foreign oil of most countries. EVs can further be seen as a mobile form of energy storage and can potentially be used for grid services (vehicle to grid technology) [14]. The recent emergence of LIB powered EVs is expected to contribute to the creation of a new battery market segment related to large-scale battery systems. The intermittent renewable integration sector will benefit from these developments. Home electrical energy storage solutions such as the Tesla Powerwall and the Bosch BPT-S 5 Hybrid serving to optimize electricity consumption in conjunction with variable photovoltaic electricity production and as an emergency backup in the event of utility outage are indeed already available on the market. Large-scale stationary battery power stations mainly based on LIB technology, and often used in conjunction with wind and photovoltaic power stations, have been emerging during recent years (see [15]). However, mature as the technology may seem, improvements in terms of battery performance (*e.g.* energy density, cycle life), safety and cost, are still required to fulfil the demands of these applications. For EVs the key factors are energy density and cost, while for stationary storage the emphasis will be more on cost and cycle life than on energy density [5, 16]. Battery systems for stationary storage are expected to be lower in cost because they can be designed in a modular manner. In contrast systems for EVs need to be optimized with respect to energy and power capabilities for each type of car. Lower cost can also be expected for stationary storage because safety is easier to assure than in a

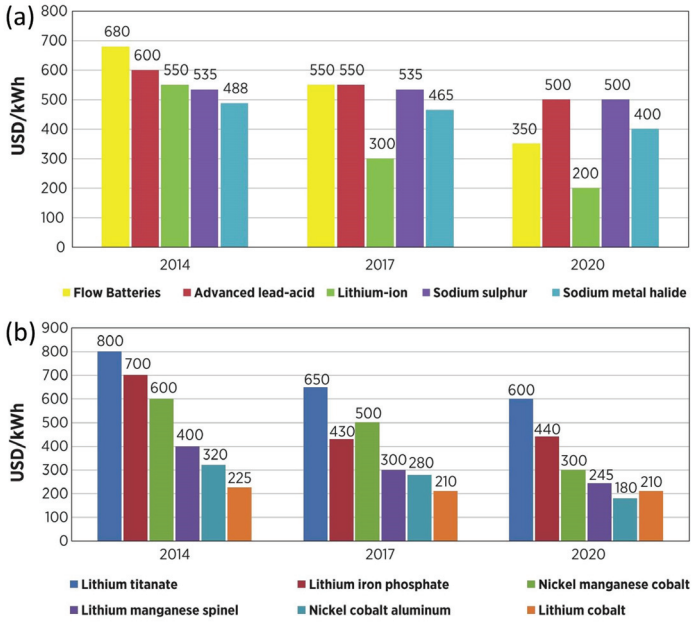

Figure 1.3: Lowest current and projected battery cell prices for (a) stationary battery storage technologies and (b) LIB systems with positive electrodes as labelled and graphite as negative electrode for stationary storage. Battery modules and containers, power components, thermal management systems and other components add to the overall cost [10].

mobile situation [5]. The improvement of LIBs and their mass production for the EV sector will reduce costs and thereby advance the implementation of LIB technology for stationary storage over other technologies (Figure 1.3(a)) [10, 17, 18].

Cell prices for most of the LIB systems are expected to drop over the coming years, while the standardised lithium cobalt system ($LiCoO_2$ *vs.* graphite) used to a large extent in portable electronics and EVs is approaching a fundamental limit because of material costs, see Figure 1.3(b) [10]. This creates doubts whether LIB technology will be able to meet the future energy storage cost requirements [19]. There are further concerns about a possible Li shortage associated with the expansion of LIB technology to large-scale applications (*i.e.* the transportation and stationary battery storage sector)

which might drive up costs for Li precursor materials considerably [17, 18]. Despite its relatively wide distribution in the Earth's crust Li cannot be considered an abundant element [20]. Li natural resources are unevenly distributed (mainly found in Bolivia, Chile, Argentina, the United States and China) and the production of LIBs in most countries therefore depends on imports [18, 20]. Li recycling has been insignificant but has increased steadily due to the growth in LIB consumption [18]. During the last decades discrepancies in supply and demand of Li-containing precursor materials (*e.g.* Li_2CO_3) for battery manufacture have led to a steep rise in prices [21, 22]. Although Li precursors currently only account for a relatively small fraction (∼3 %) of the cost at the cell level, and it is rather the costs for precursors of transition metals (*e.g.* Co, Ni, and Mn) which determine the cell prices (∼33 % of the cell cost) this situation may change in the future [23]. The cost for the Li precursor may increase the battery cost by up to 10 % [24]. The limits placed on cell price by raw material costs associated with large-scale use of LIB technology may restrict the feasibility of large-scale stationary LIB storage where cost is of primary interest [19].

In this regard sodium-ion batteries (SIBs) become a promising alternative to LIBs and renewed research interest has been devoted in the recent years to develop suitable SIB systems. Na is located below Li in the periodic table and they share similar physical and chemical properties in many aspects. The working principles of SIBs and LIBs are the same. Existing LIB technology could be readily adapted to SIBs. Unlike Li, Na is abundant and readily available worldwide. Na containing precursor materials are therefore much cheaper than their Li analogues, *e.g.* Na_2CO_3 is about 20-30 times cheaper than Li_2CO_3 [21, 25, 26]. A further, maybe even greater, cost advantage at the cell level (∼8 % if the energy density of the SIB and LIB would be the same) might be provided by the use of an inexpensive Al current collector for both electrodes in SIBs instead of an expensive Cu current collector because, unlike Li, Na does not alloy with Al [19, 23, 27]. An obvious place to look for good SIB electrode materials would be among those systems that function well in LIBs. However, if analogous electrode materials are selected in a SIB and in a LIB, respectively, lower energy densities can be expected because of some intrinsic differences between Na and Li. Na is larger (1.02 Å *vs.* 0.76 Å)

as well as heavier (6.94 g/mol *vs.* 23.00 g/mol) than Li and the standard electrochemical potential is lower for Na than for Li (-2.71 V *vs.* -3.04 V against standard hydrogen electrode). A good example is shown by Yabuuchi *et al.* [20] where the electrochemical performances of the $LiCoO_2$ and $NaCoO_2$ systems are compared, the latter showing lower energy density. Associated with the lower energy density, although partly compensated for by the lighter Al current collector instead of Cu, some of the cost advantage is lost when considering the cost per energy unit. That a LIB electrode system would also work in a SIB is, however, not always granted. Graphite for instance is the most commonly used negative electrode material in LIBs, but shows poor performance in SIBs [28]. These examples show that the strategy of adopting LIB electrode systems for SIBs will not be sufficient, as differences in behaviour have been observed and there may be SIB electrode materials with high energy densities and low costs yet to be discovered. The realization of the unique electrochemical activity of the Fe^{3+}/Fe^{4+} redox-couple in SIB positive electrodes (*e.g.* $NaFeO_2$) is an example of such a discovery [29]. The use of sustainable elements such as Fe and Mn for the positive electrode is preferred over other transition metals due to limitations in their availabilities and associated high costs (*e.g.* the $LiCoO_2$ system). Berg *et al.* presented an energy-cost comparison for current LIB and some SIB systems [19]. They concluded that SIBs can only be cost competitive if the price for Li precursors increases significantly or if the energy density of the SIBs can be increased substantially, at least to the level of common LIBs. Choi and Aurbach came to a similar conclusion and identified the poor negative electrode performance as the bottleneck [25]. It follows that there is a huge incentive to search for sustainable SIB electrode systems with long cycle life, high energy densities and/or low cost per energy unit in order to make this emerging energy storage technology available in the coming years.

In a LIB (SIB) alkali metal ions shuttle via an electrolyte and electrons via an external circuit between the positive and negative electrodes during discharge (cathode and anode) and charge. During this process redox reactions take place in tandem at both electrodes which enable the redox active electrode materials to take up and release alkali metal ions while undergoing electronic as well as structural changes. The atomic structure is either

maintained (solid solution behaviour) or transformed into a new structure (two-phase behaviour) while the concentration of alkali metal ions in the electrode increases or decreases. The number of available alkali metal ion sites in the host structure determines the theoretical material specific capacity. The energy gain when an alkali metal ion moves from the positive to the negative electrode material during discharge is related to the operation voltage. The energy density (*i.e.* the energy released per unit mass or volume) of a material is proportional to its capacity and operation voltage. A number of advances towards higher practically achievable energy densities have been made by controlling the electrode material's particle size to reduce kinetic limitations as well as composition to improve the operation voltage or the structural stability at a higher degree of alkali metal ion extraction (insertion). The cycle life of a battery is defined as the number of times it can be discharged and charged (cycled) before a certain threshold value of its nominal capacity is reached due to capacity degradation. The cycle life can be reduced because of electrolyte degradation or changes in the electrode morphology caused by large volume changes and/or pronounced phase transformations leading to a loss of contact with the electrochemically active material by partial detachment of the electrode film or breaking-up (pulverization) of the particles. Relevant electrochemical concepts and methods as well as a short review of SIB electrode materials are given in Chapter 2.

Understanding the working and degradation mechanisms of electrode materials at the atomic scale is fundamental to optimize battery materials. The key to this is the investigation of the chemical processes in the battery *in situ* during operation (also called *operando*). The study of these mechanisms has been the topic of the research papers of this dissertation, with respect to measurement techniques and materials.

A short review of advanced *operando* methods is presented in Section 2.6. The electrochemical response of a battery material is intimately linked to its structural and electronic changes upon cycling. *Operando* X-ray diffraction (XRD) is perfectly suited to pinning-down the nature of the reaction mechanism (single *vs.* multi-phase behaviour), its associated structural changes (atomic arrangement, volume) and its structural stability (*e.g.* pulverization, amorphization) upon cycling. These are critical factors for battery perform-

ance *i.e.* the voltage profile and cycle life. *Operando* X-ray absorption spectroscopy (XAS) including X-ray absorption near edge spectroscopy (XANES) and extended X-ray absorption fine structure (EXAFS) can be used to study the evolution of electronic and local structure of electrode materials upon cycling. The XANES portion of the spectrum provides information about the oxidation state variations of specific atoms and their site symmetries. EXAFS probes the short range order in the vicinity of specific elements and enables us to follow the evolution of inter-atomic distances in the electrode material. A short theoretical background of the X-ray methods (XRD and XAS) used for the *operando* analysis is introduced in Chapter 3.

With the aim of studying chemical processes in electrode materials at the atomic scale during battery operation, a fully operational set-up (electrochemical cells, sample changer and interfacing software) that enables combined quasi-simultaneous *operando* XRD and XAS (XANES and EXAFS) measurements coupled with electrochemical characterization was developed in the course of this work (`Paper I`). Relevant considerations for this cell design and implementation as well as a comparison to other set-ups are provided in Section 5.2.1.

The combined *operando* analysis provides a deep insight into the electrochemical reaction and degradation mechanisms of electrode materials during discharge and charge of the battery which is demonstrated for several SIB electrode materials in this dissertation (the main emphasis was on negative electrode materials). Various material-related properties such as vacancy and water content, crystallite size and nanostructuring were found to affect the structural chemistry during cycling, which was put into context with the electrochemical properties of the battery system. Experimental details are given in Chapter 4. The systems studied include the Prussian blue analogue (PBA) $Na_{1.32}Mn[Fe(CN)_6]_{0.83} \cdot z\,H_2O$ as SIB cathode (`Paper II`); and Bi (`Paper III`), Bi_2S_3 (`Paper I`), $BiVO_4$ and $Bi_2(MoO_4)_3$ (`Paper IV`) as SIB anodes. After the key issues in SIB research will have been addressed in Section 2.5 the reasons for the choice of these materials will be elaborated in Chapter 5. Chapter 5 further provides a summarising discussion of the main research papers which form the body of this dissertation. Therein, the key findings of the main research papers will be discussed and put into a broader

context. Chapter 5 finishes with some concluding remarks and an outlook. The main research papers can be found in Appendix A.

Chapter 6 presents contributions to other aspects of non-aqueous rechargeable batteries, in terms of the metal ion system (Li instead of Na) and/or the methods used to study their working mechanisms, based on the supplementary research papers which are also appended in Appendix A. `Paper V` reports an *operando* synchrotron study of ordered and disordered high voltage spinel $LiMn_{1.5}Ni_{0.5}O_4$ for LIB cathodes and `Paper VI` presents a combined *ab initio* computational and experimental study of the Na and Li insertion mechanism into fully amorphous (glassy) carbon. These works, in particular the structural or electrochemical data collection and analysis thereof, were important for the commissioning of the electrochemical cell (`Paper I`) and for estimating the capacity contribution of the carbon to the Bi and Bi metalate carbon composite anodes (`Paper III` and `Paper IV`). Being related but not central to the main findings of this dissertation on *operando* X-ray studies of SIB materials, with an emphasis on anode materials, the key findings of these supplementary research papers are not included in the main summarizing discussion of this dissertation (Chapter 5) but are summarised, discussed and put into a broader context in Chapter 6. Please note that list of the research papers and a statement of my contributions to these can be found in the front matter.

Chapter 2

Non-aqueous rechargeable batteries

2.1 Electrochemical cell and basic concepts

A lithium- or sodium-ion cell or battery consists of positive and negative electrode(s) and an electrolyte in a casing. The electrodes include active materials which are capable of accepting and releasing Li or Na ions; a conductive additive (*e.g.* carbon black) which electrically connects the active material with a current collector; and a suitable (usually polymeric) binder which attaches the electrode particles to the current collector. The current collectors (*e.g.* Al, Cu foil) enable connection to an external circuit. When the electrolyte is a liquid (*e.g.* Li or Na salt such as $LiPF_6$ or $NaPF_6$ dissolved in non-aqueous organic carbonate-based solvents, which were used in this work) the cell will normally also include a separator situated between the electrodes. The separator is usually a semi-permeable membrane which permits ionic charge carriers to travel through the electrolyte from one electrode to the other while separating the electrodes in order to prevent short circuits. The housing encases the components of the cell, providing a barrier between the cell and the external environment so that the electrodes and electrolyte are protected from reaction with atmospheric gases, especially moisture.

During charging and discharging of the battery over the external circuit, Li or Na ions move between the positive and negative electrodes as illustrated in Figure 2.1. When the cell is discharged, electrochemical reduction takes place at the positive electrode as electrons flow through an external elec-

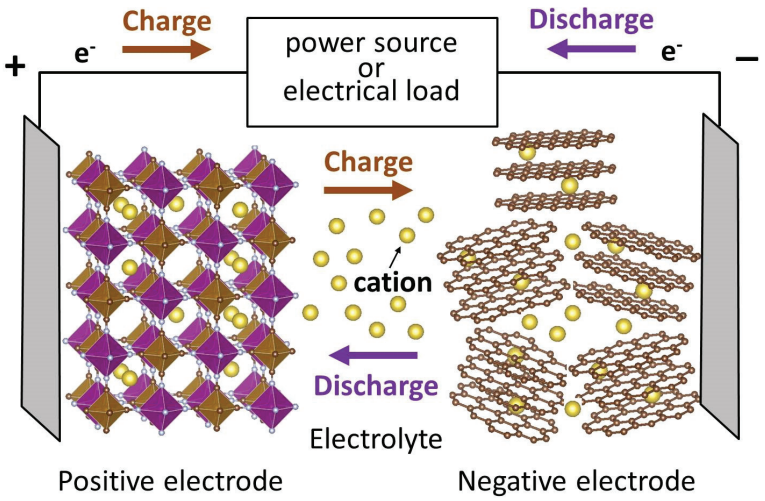

Figure 2.1: Illustration of the working principle of a rechargeable lithium- or sodium-ion battery.

trical load towards the positive electrode while cations move within the cell through the electrolyte to the positive electrode. Electrochemical oxidation correspondingly takes place at the negative electrode. The positive electrode during discharging is commonly referred to as the "cathode" and the negative electrode as the "anode". The cathode and anode materials exhibit high and low voltages *vs.* Li/Li^+ or Na/Na^+, respectively. Their voltage difference leads to a cell voltage (Section 2.2.2). The reduction of the cell voltage is the driving force for the discharge. The discharging processes are reversed when the cell is charged by an external electrical power source which applies an overpotential (a higher voltage than that produced by the cell, with the same polarity) and drives the cations and electrons in the opposite directions compared to discharging. The cathode and anode should operate at voltages within the stability range of the electrolyte, although its limits can be exceeded if a stable passivation layer at the electrode protects the electrolyte from decomposition (Section 2.2.4).

The capacity (C in Ah) of the battery is given by the number of electrons (or cations) exchanged between positive and negative electrodes and can be

stated as

$$C = \int I(t) \cdot \mathrm{d}t \tag{2.1}$$

where $I(t)$ is the current (in A) *i.e.* the number of electrons flowing over the external circuit per time interval dt which is integrated over the discharge period (in h). The capacity of an electrode material is commonly expressed with reference to the mass of the active material (in Ah/kg or alternatively in mAh/g), see Section 2.2.1. The battery can deliver a power (P in W or W/kg) and is defined as

$$P(t) = V(t)I(t) \tag{2.2}$$

where $I(t)$ is the current drawn at a certain cell voltage ($V(t)$ in V). The work delivered by a battery or the energy contained in a battery (W in Wh or Wh/kg) is given by the power ($P(t)$) delivered over the discharge period as

$$W = \int P(t) \cdot \mathrm{d}t = \int V(t)I(t) \cdot \mathrm{d}t \tag{2.3}$$

Specific capacity and energy densities of battery materials are commonly compared relative to mass, volume and cost. The more electrode material is contained in the battery the greater its capacity and energy. The higher the cell voltage the greater its power and energy.

The active materials of the electrodes allow the reversible uptake and release of Li or Na ions. This may happen by

- movement of the Li or Na ions into (*i.e.* “insertion” or “intercalation”) or out of (*i.e.* “extraction” or “deintercalation”) their chemical structures ("phases"), as appropriate;

- by conversion of the materials between Li/Na poor and rich (*e.g.* "alloying") or rich and poor (*e.g.* "dealloying") phases, as appropriate; or

- by conversion of the electrode material into other more Li /Na rich/poor chemical forms or mixtures thereof (usually referred to as "conversion" or "displacement" reaction) with the average Li/Na content of the entire electrode varying.

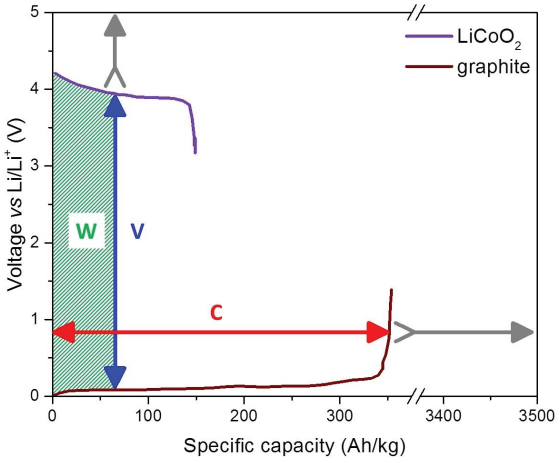

Figure 2.2: Voltage profiles *vs.* specific capacity of $Li_{1-x}CoO_2$ reduction at the cathode and Li_xC oxidation at the anode measured against a Li/Li^+ counter (reference) electrode.

The overall Li or Na content in the electrodes will thus either be varied by changing the composition of one phase ("solid solution behaviour") or the ratio between coexisting phases ("multi-phase behaviour"), see Section 2.2.2.

In a LIB the positive electrode is commonly a layered oxide such as lithium cobalt oxide ($LiCoO_2$), a polyanionic compound such as lithium iron phosphate ($LiFePO_4$) a spinel such as lithium manganese oxide ($LiMn_2O_4$) or a layered sulphide such as lithium titanium sulphide ($LiTiS_2$). Other commonly-used layered oxides include lithium nickel cobalt aluminium oxide ($LiNi_{0.8}Co_{0.15}Al_{0.05}O_2$), lithium nickel cobalt manganese oxide ($LiNi_{1/3}Co_{1/3}Mn_{1/3}O_2$) and lithium nickel oxide ($Li_{1-z}Ni_{1+z}O_2$ where $0 < z < 0.2$). Commonly studied insertion materials are $LiMnO_2$, Li_2MnO_3, $LiCo_2O_4$, $LiMn_{1.5}Ni_{0.5}O_4$, $LiMnPO_4$, $LiCoPO_4$, $LiFeSO_4F$ and $LiVPO_4F$. Commonly studied conversion cathode materials include fluorides (*e.g.* FeF_3, CuF_2, AgF), chlorides (*e.g.* $FeCl_3$, $CuCl_2$) and chalcogenides (*e.g.* S, Se, Li_2Te). The negative electrode is commonly graphite (C). Other commonly used studied negative electrode materials include insertion materials such as spinel lithium titanium oxide ($Li_4Ti_5O_{12}$) and titanium dioxide (TiO_2); alloy forming metals or metaloids such as silicon (Si), germanium (Ge) and tin

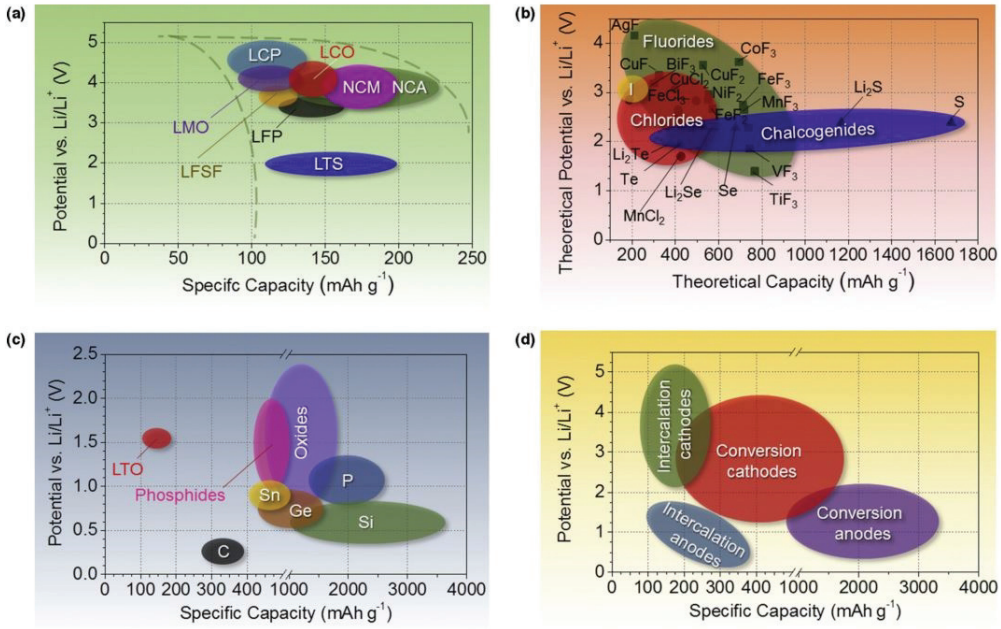

Figure 2.3: Approximate voltage and specific capacity ranges of most common LIB (a) intercalation as well as (b) conversion cathode and (c) anode materials. (d) Overview of average ranges for all types of LIB electrodes [30].

(Sn); and conversion materials such as transition metal oxides (*e.g.* Fe_2O_3, Fe_3O_4, Co_3O_4, CoO, MoO_2) and metal oxides (*e.g.* SiO, SnO) [30, 31].

The overall electrochemical cell reaction involving LiMA where MA represents the host chemistry (*e.g.* CoO_2, $FePO_4$ or Mn_2O_4 with M being the transition metal and A the anion unit) and graphite during discharge is given by addition of the two half cell reactions

$$\text{Reduction at cathode } (+): \quad \mathrm{Li_{1-x}MA + x\,Li^+ + x\,e^- \rightleftharpoons LiMA} \qquad (2.4)$$

$$\text{Oxidation at anode } (-): \quad \mathrm{Li_xC_6 - x\,Li^+ - x\,e^- \rightleftharpoons 6\,C} \qquad (2.5)$$

$$\text{Overall reaction } : \quad \mathrm{Li_{1-x}MA + Li_xC_6 \rightleftharpoons LiMA + 6\,C} \qquad (2.6)$$

Figure 2.2 compares the voltage profiles of the half cell reactions *vs.* specific capacity (Equations 2.4 and 2.5) where $\mathrm{MA} = \mathrm{CoO_2}$ and $x < 0.5$. In a full

battery the weight ratio of active materials in anode and cathode needs to be adjusted according to their specific practical capacities and irreversible capacity losses in the initial discharge and charge cycle. Figure 2.2 further illustrates that batteries with higher energy densities can be achieved by increasing the cell voltage and/or specific capacity of the active electrode materials as indicated by the grey arrows.

Approximate voltage and specific capacity ranges for common LIB materials are represented in Figure 2.3. The active materials used in cathode and anode operate commonly at voltages above and below 2 V *vs.* Li/Li^+, respectively. Conversion materials exhibit much higher specific capacities compared to intercalation materials. Further important parameters (other than voltage and specific capacity) which allow comparison of active material battery performance characteristics are presented in Section 2.3. Cathode and anode materials for SIBs are reviewed in Section 2.5.

Batteries commonly consist of several electrically interconnected cells. These may be coupled in series or in parallel in order to meet voltage and capacity requirements for technological applications. In this work, cells (hereafter also referred to as batteries) comprising one negative electrode and one positive electrode were assembled for testing purposes. As working electrode either cathode or anode material was measured against a Li or Na metal counter electrode. This cell configuration is commonly referred to as a "half cell".

2.2 Electrochemical principles

In this section the theoretical background on electrochemistry of non-aqueous rechargeable batteries will, for simplicity, be presented based on examples for LIBs. Exactly the same principles apply to SIBs.

2.2.1 Faraday's law and theoretical capacity

Faraday's law describes the quantitative relationship between the total electric charge (Q) exchanged via the external circuit and the number of moles

of electrons in an electrochemical reaction. Faraday's law can be stated as

$$Q = n\ z\ e\ N_A = n\ z\ F \tag{2.7}$$

where n is the number of moles of transferred z-valent ions ($z = 1$ for Li), e is the elementary charge ($e = 1.602 \cdot 10^{-19}\,\mathrm{C}$), N_A is the Avogadro constant ($N_A = 6.02 \cdot 10^{-23}\,\mathrm{mol}^{-1}$) and F is the Faraday constant ($F = eN_A = 26801\,\mathrm{mAh/mol}$) which is defined as the quantity of electric charge per mole of electrons (or Li ions) transferred. For the electrochemical reaction presented in Equation 2.4 the theoretical specific gravimetric and volumetric capacities of MA as a Li host can then be expressed as

$$C_t\,[\mathrm{mAh/g}] = \frac{xF}{M} \qquad \text{and} \qquad C_t\left[\mathrm{mAh/cm^3}\right] = \frac{x\rho F}{M} \tag{2.8}$$

where x is the difference in number of moles of Li atoms between the reactant ($\mathrm{Li}_{1-x}\mathrm{MA}$) and the product (LiMA), M is the molar mass of reactant (in g/mol) and ρ is its density (in $\mathrm{g/cm^3}$).

2.2.2 Gibbs free energy and cell voltage

The change in Gibbs free energy ($\Delta G < 0$) of a cell reaction is the driving force which enables a battery to deliver electrical energy to an external load during discharge.

In Equation 2.6, $\mathrm{Li}_{1-x}\mathrm{MA}$ takes up x moles of electrons to form LiMA at the cathode (+) during discharge, whilst $\mathrm{Li}_x\mathrm{C}_6$ releases x moles of electrons to form 6 moles of C at the anode (−). The change in Gibbs free energy (G in J/mol) at equilibrium (open circuit, oc) can be expressed as

$$\Delta G = x(\mu^+_{\mathrm{Li}} - \mu^-_{\mathrm{Li}}) = -xF(V^+ - V^-) = -xFV^{\mathrm{oc}} \tag{2.9}$$

where $\mu^{+,-}_{\mathrm{Li}}$ are the Li chemical potentials (in J/mol) within the cathode and anode, respectively, F is the Faraday constant ($F = 96485\,\mathrm{C/mol}$) and $V^{+,-}$ and V^{oc} are the open circuit voltages (or electromotive forces) of the half cell (*vs.* $\mathrm{Li^+/Li}$) and overall reaction, respectively. In a half cell reaction the Li chemical potential of the Li metal electrode is assumed to remain constant

during discharge and charge.

Thermodynamic quantities such as Li chemical potentials, Gibbs free energies and derived quantities such as entropies and enthalpies ($\Delta G = \Delta H - T\Delta S$) can thus indirectly be obtained by simple measurement of the voltage. Alternatively it is possible to estimate the cell voltage based on *ab initio* calculations of these thermodynamic quantities [32–34]. For *ab initio* calculations energies are commonly expressed in eV/(Li atom). Using this convention the F is replaced by e in Equation 2.9. The average voltage is then given as

$$V^{\text{oc}} = -\frac{1}{e}\frac{\Delta G}{\Delta x} \tag{2.10}$$

where Δx refers to the number of transferred Li atoms as in the generalized form of Equation 2.4 for any intermediate reduction step

$$\text{Li}_x\text{MA} + \Delta x\ \text{Li}^+ + \Delta x\ \text{e}^- \longrightarrow \text{Li}_{x+\Delta x}\text{MA} \tag{2.11}$$

Courtney *et al.* [33] suggested a further approximation for the Gibbs free energy given that

$$\Delta G = \underbrace{\Delta E}_{\substack{0.1\text{ to }4\\ \text{eV/(Li atom)}}} + \underbrace{P\Delta V}_{\substack{\sim 10^{-5}\\ \text{eV/(Li atom)}}} - \underbrace{T\Delta S}_{\substack{\approx k_B T \ll \Delta E\\ \text{at ambient T}}} \approx \Delta E \tag{2.12}$$

where the change in internal energy (ΔE) is much larger than $P\Delta V$ and $T\Delta S$. A good approximation for the voltage is thus given by

$$V^{\text{oc}} \approx -\frac{1}{e}\frac{\Delta E}{\Delta x} \tag{2.13}$$

The total internal energy (E_{total} in eV/(Li atom)) for a particular composition of Li_xMA can be obtained from *ab initio* calculations which allows us to estimate the voltage profile of an electrochemical reaction. For Equation 2.11 the half cell voltage as a function of the fraction of available interstitial Li sites (x) is given by

$$V^{\text{oc}}(x) \approx \frac{1}{e}\left(\frac{E_{\text{total}}(\text{Li}_x\text{MA}) - E_{\text{total}}(\text{Li}_{x+\Delta x}\text{MA})}{\Delta x} + E_{\text{total}}(\text{Li})\right) \tag{2.14}$$

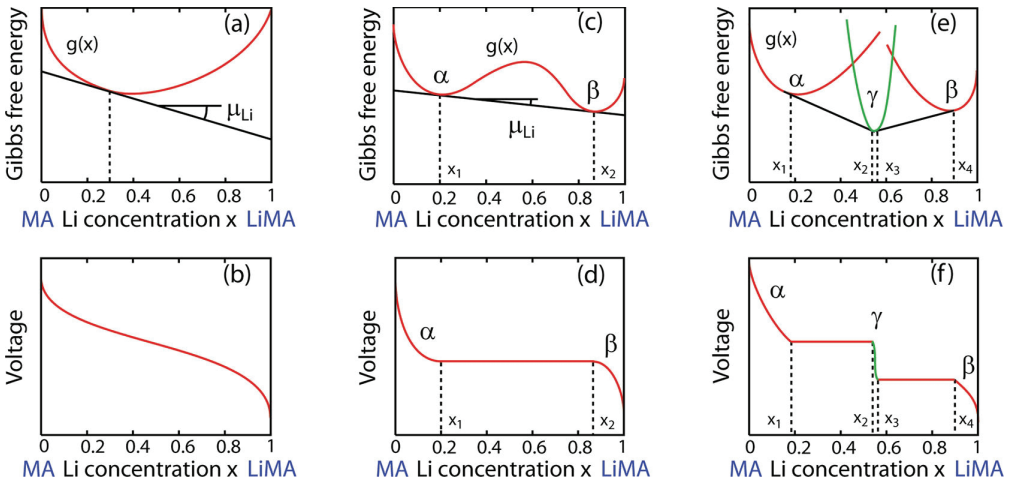

Figure 2.4: The voltage profile is linearly related to the derivative of the Gibbs free energy of an electrode material (MA) *vs.* Li concentration. (a,b) Solid solution behaviour, (c,d) two-phase behaviour with a direct transition from phase α to β and (e,f) two-phase behaviour with a stable intermediate phase γ between phases α and β [34].

Any changes in structure or chemistry of the material will affect its Gibbs free energy and thus its voltage. The nature of the phase transformations due to changes in Li content will have clear signatures in the voltage profile. Various scenarios for the Gibbs free energy ($G(x) \approx E(x)$) are presented in Figure 2.4 and can be summarised as follows [34]:

- If the host (MA) forms a solid solution with Li (single phase over the full compositional range) $G(x)$ has a single minimum. The voltage profile will be linearly related to the derivative of the Gibbs free energy ($\Delta x \rightarrow 0$) resulting in a sloping shape (Figures 2.4(a) and (b)). Examples are layered oxides Li_xCoO_2 and $Li_xNi_{1/3}Co_{1/3}Mn_{1/3}O_2$.

- If the Li insertion is accompanied by a first-order phase transformation between a Li poor (α at x_1) and Li rich (β at x_2) phase maintaining the same host structure $G(x)$ will exhibit two local minima. In the miscibility gap (between x_1 and x_2) the free energy of the two-phase mixture resides on the common tangent of the two minima which results

in a constant plateau in the voltage profile (Figures 2.4(c) and (d)). An example is olivine type Li_xFePO_4.

- Analogously, steps in voltage plateaus are observed if several first-order phase transformations involving stable intermediate phases (*e.g.* γ) take place (Figures 2.4(e) and (f)). Examples are spinel type $Li_xMn_2O_4$ and $Li_{1+x}Ti_2O_4$.

The phase transition behaviour may change when nanosized materials (one dimension <100 nm) are used. Size reduction of Li_xFePO_4 may result in increased Li solid solution behaviour in the end members and a reduced miscibility gap between the coexisting end members. The origin of the size dependency is not fully understood. It may be associated with the concomitant increase in elastic strain in coexisting phases. The miscibility gap might be reduced due to a reduction in interface coherency strain when the Li concentration difference between the end members is reduced. The coherency strain thereby acts as a barrier to phase separation. Atomic disorder (*e.g.* doping, anti-site disorder) is an other parameter which can alter the phase transition behaviour. In Li_xFePO_4 it may decrease the miscibility gap and, depending on the degree of disorder, even result in full solid solution behaviour [35, 36].

2.2.3 Electrode processes, kinetic limitations and overpotential

The maximum electric energy that can be delivered by the active electrode materials in a battery depends on the change in Gibbs free energy ($\Delta G = -C_t V^{oc}$) as defined in Equations 2.8 and 2.9 for equilibrium conditions (open circuit). However, losses will occur due to kinetic limitations if a non-negligible current passes through the electrodes and causes a shift in voltage ("overpotential", "polarization" or "hysteresis") or if an overpotential is applied and results in a current flow, accompanying the electrochemical reactions. Despite the simplicity of the electrochemical reactions (*e.g.* Equations 2.4 to 2.6), the mechanism of the overall electrochemical process is complex and each half cell reaction involves several elementary steps that

can be related to conduction phenomena. In electrochemistry the origins of overpotential are traditionally assigned to [37]

- *ohmic overpotential (or "IR-loss")* due to cell specific internal resistance (impedance) combining ionic (electrolyte within separator and porous electrode), electrical (active material, current collectors and conductive additives) and interfacial (between active material and electrical tabs) resistances;

- *activation (or charge transfer) overpotential* due to limited rate of charge transfer (adsorption/desorption of Li ions) at the electrode/ electrolyte interface; and

- *concentration (diffusion) overpotential* due to limited mass transport capabilities within electrode material or electrolyte when reactants are transported to and products away from the electrode/electrolyte interface.

Recently, more specific origins for overpotentials in LIBs were suggested. These include

- *nucleation and growth overpotential* due to nucleation barriers in binary solids at the coherent miscibility gap. The nucleation barrier is set by coherency strain energy in large particles and reduced by surface energy in nanoparticles (suggested for $LiFePO_4$) [35, 36, 38];

- *mechanical stress overpotential* due to reaction barriers induced by compressive stress in the surface layer of the electrode material (suggested for Si) [39, 40]; and

- *displacement (interdiffusion) overpotential* due to a mismatch in ionic mobilities between the electrochemically active species (*e.g.* Li) and displaced ionic species in a conversion electrode transition metal non-metal (*i.e.* F, O, P, N, S, H *etc.*) compound with lacking driving force for redistribution of the displaced ions during charge resulting in different reaction pathways during discharge and charge (suggested for FeF_3 and Co_3O_4 conversion electrodes) [41–44].

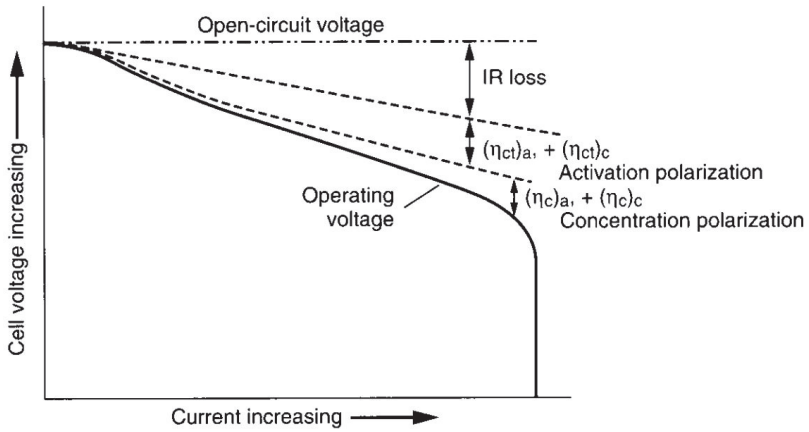

Figure 2.5: Cell overpotential (polarization) as a function of operating current during discharge [37].

The rate of the overall electrochemical process is limited to the rate of the slowest of the elementary steps. The Li diffusivity in the liquid electrolyte, for instance, is several orders of magnitude higher than in the solid state electrode material [45]. It is therefore a good approximation to neglect the mass transport limitations of Li ions in the liquid electrolyte. Overpotentials can be estimated from theoretical equations as described in [37]. Figure 2.5 illustrates the ohmic, activation, concentration and overall overpotential being the sum of the individual contributions according to these traditional models. More complex theories are required to model non-equilibrium electrochemical processes in/at electrode particles of finite size [36]. Further degrees of complexity must be introduced to describe electrochemical processes of LIB electrodes. These are typically composed of many micro- or nanocrystalline active material particles, conductive additive and binder, and are porous to some degree with certain dimensions [38].

The overpotential generally increases with the operating current (Figure 2.5). Only at very low currents can the cell operate close to the equilibrium voltage and deliver most of the theoretical capacity. Figure 2.6 illustrates how the equilibrium (open circuit) voltage *vs.* capacity profile is affected by kinetic limitations when a constant discharge current is applied. The presence of overpotentials implies that less energy is recovered and more energy

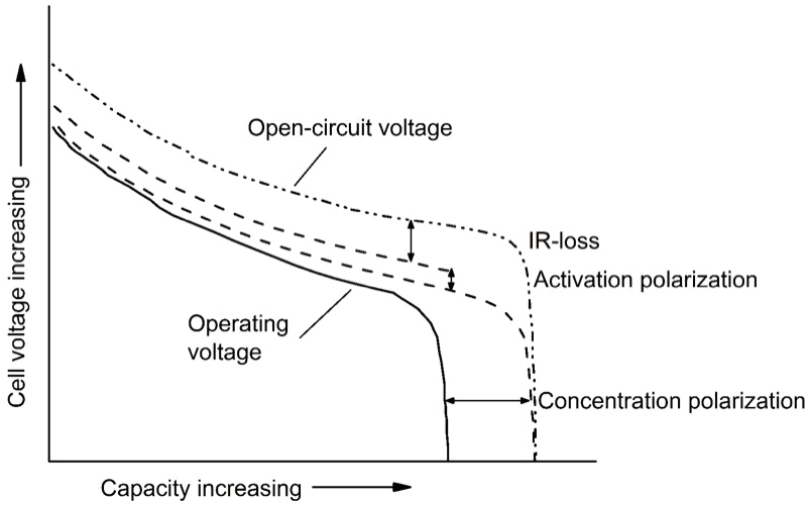

Figure 2.6: Comparison of open circuit and operating voltage at a constant discharge current as a function of capacity. Overpotential (polarization) contributions are indicated.

is required during discharge and charge, respectively, than theoretically predicted for equilibrium conditions. In both processes the overpotential will lead to energy loss in the form of waste heat. Additional energy is lost due to mass transport limitations (concentration overpotential) which give rise to saturation and depletion of Li ions within the electrode material near the electrode/electrolyte interfaces during discharge and charge respectively, and thereby reduce the available capacity.

Overpotential may also cause deviation from the reaction path predicted by equilibrium phase diagram. In Li_xFePO_4 two-phase behaviour is strongly suppressed under applied current since reaction limitation, anisotropic Li transport, elastic coherency strain and interfacial energies are enhanced [36]. For lithiation of Si the phase diagram predicts several two-phase steps between equilibrium intermetallic compounds ($Li_{12}Si_7$, Li_7Si_3, $Li_{13}Si_4$ and $Li_{22}Si_5$). However, kinetic limitations lead to two-phase behaviour with metastable amorphous a-Li_xSi ($x \approx 3.4$) during the first lithiation. A large activation energy is required to break the Si−Si bonds at the reaction front where the formation of the highly lithiated a-Li_xSi gives rise to large coherency

strains. Finally a metastable phase ($Li_{15}Si_4$) with composition close to the amorphous phase crystallizes. Upon delithiation $Li_{15}Si_4$ transforms back to amorphous a-Li_xSi without crystallization of Si [39].

2.2.4 Electrolyte stability and solid electrolyte interface

The electrolyte is the medium which permits ionic charge carriers to travel from one electrode to the other. Most commercial LIBs employ a non-aqueous electrolyte solution which is commonly composed of an electrolyte salt and organic carbonate-based solvents. It should provide high ionic conductivity ($>10^{-4}$ S/cm), low electrical conductivity ($<10^{-10}$ S/cm), a large electrochemical voltage stability window, a large usable liquid range (-40 °C to 60 °C), a low vapour pressure, a low viscosity, good solvating properties, good chemical and thermal stability, low toxicity, easy biodegradability and low price [46]. The most commonly used electrolyte salt is $LiPF_6$, which combines most of the requirements for a good electrolyte-building salt. The best solvent properties with respect to these requirements are usually obtained by using blends of solvents such as ethylene carbonate (EC) and diethyl carbonate (DEC) or dimethyl carbonate (DMC). Compared to aqueous electrolytes non-aqueous electrolytes provide larger liquid ranges, larger voltage windows and better compatibility with electrode materials, but show lower ionic conductivities, are less safe due to flammability and have higher cost [46]. A lot of research efforts are currently devoted to solid electrolytes because they could enable larger voltage windows and diminished flammability in comparison to non-aqueous liquid electrolytes. However, achieving the required combination of a large voltage window and high ionic conductivities as well as maintenance of a permanent interfacial contact at the electrodes remains a challenge [46, 47].

Figure 2.7 illustrates the energy diagram of a LIB (SIB) at open circuit. The band gap (E_g) between the lowest unoccupied molecular orbital (LUMO) and the highest occupied molecular orbital (HOMO) of the electrolyte components will determine the electrochemical stability range of the electrolyte. It indicates where no electrochemical oxidation ($\mu_{\mathrm{Li}}^{+} > HOMO$) or reduction ($\mu_{\mathrm{Li}}^{-} < LUMO$) of electrolyte solvent or ions takes place when a voltage is ap-

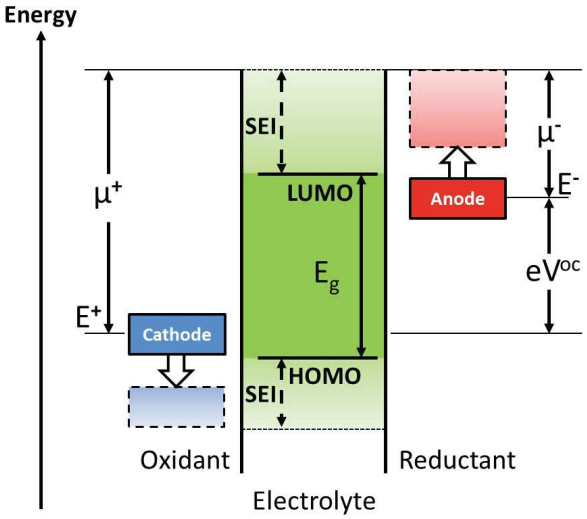

Figure 2.7: Schematic equilibrium energy diagram of a non-aqueous battery. E_g represents the stability range of the electrolyte against oxidation and reduction at the electrodes. The stability range might be increased by the formation of a passvating SEI. Energies and potentials are represented against Li/Li^+.

plied at the electrodes unless a passivation layer blocks the electron transfer between electrode and electrolyte bands (electrochemical potentials, $\mu_{Li}^{+,-}$, and open circuit voltage, V^{oc}, relations were introduced in Section 2.2.2). A unimolar ($1\,M = 1\,mol/L$) solution of $LiPF_6$ in EC/DMC (1:1) has an electrochemical stability range between 1.3 V and >5 V (*vs.* Li/Li^+) [48].

The electrochemical potentials of Li metal commonly used in half cells to measure $\mu_{Li}^{+,-}$ of a practical electrode material and commonly used anode materials such as graphite (Figure 2.2) often lie above the LUMO of the electrolyte ($\mu_{Li}^{-} > LUMO$). However, a passivation layer commonly referred to as an solid electrolyte interface (SEI) forms due to reduction of the electrolyte. This process occurs mainly, though not exclusively, at the beginning of cycling, especially during the first cycle. The SEI prevents further decomposition of the electrolyte. Additives to the electrolyte solution such as vinylene carbonate (VC) are commonly used in LIBs to create a more stable SEI [49].

SEI formation and stability on graphite have recently been reviewed [50]. If the battery is charged above the upper limit ($\mu^{+}_{\mathrm{Li}} < HOMO$) an SEI may form at the cathode due to oxidation of electrolyte components. The operating voltages of common cathode materials are within the oxidation stability limit of the electrolytes, however, if the stability limit of the electrolyte is exceeded significantly and on overcharge, parasitic sustained electrolyte decomposition may take place [49]. Sustained decomposition of the electrolyte components leads to battery failure. It may further be accompanied by the evolution and accumulation of gases which can lead to swelling of the battery and present a safety hazard [51].

The formation of a passivating SEI leads on one hand to loss of Li from the "Li inventory" of cathode and electrolyte salt in the initial cycle, reducing the reversible energy density of the battery, but on the other to higher energy densities, because of the larger practically achievable cell voltage (V^{oc}). A stable, rapidly forming passivating SEI is thus highly desirable. The SEI should ideally block any interaction with the electrolyte other than fast Li ion transfer without impeding electron transfer between the active particles and current collectors. The SEI should further be unbreakable or rapidly self-healing when broken *e.g.* by volume changes in the active particles during cycling [48].

2.3 Battery performance characteristics

To assess the performance of electrode materials for use in LIBs or SIBs, their most defining features need to be compared:

The theoretical **specific capacity** (C_t) was introduced in Section 2.2.1. The practical specific capacity, however, will depend on the applied current and on the chosen voltage range ("voltage window", see Section 2.4). In this context it is useful to introduce the concept of a discharge/charge rate ("**C-rate**"). A C-rate of fC defines the specific current (I) that is required to discharge or charge the electrode material with a nominal capacity C in τ

hours

$$f\mathrm{C} = \frac{\mathrm{C}}{\tau} = I \qquad \text{and} \qquad f = \frac{I}{\mathrm{C}} = \frac{1}{\tau} \tag{2.15}$$

The nominal capacity is commonly either set to the theoretical capacity or to a practically achievable capacity when discharged and charged at very low currents (close to open circuit conditions) in a certain voltage window. By discharging and charging at higher currents the practical capacity (C) becomes lower due to kinetic limitations (Section 2.2.3). This is shown for $LiFePO_4$ at various C-rates in Figure 2.8(a). The **capacity utilization** at the different currents can then be compared as follows

$$u_C(I) = \frac{C(I)}{\mathrm{C}} \tag{2.16}$$

Cut-off voltages are set to limit irreversible processes in the active material (*e.g.* $Li_{1-x}CoO_2$ is limited to 4.2 V where $x = 0.5$ [52]) or other parasitic side reactions such as electrolyte decomposition which lead to loss of reversible capacity and may be accompanied by gas evolution and heat production [51, 53]. However, not all capacity losses can be avoided by setting voltage limits and are subject to electrode and electrolyte optimization. In the first cycle some capacity is commonly lost due to the formation of a beneficial SEI preventing further electrolyte decomposition (Section 2.2.4). The first cycle reversible and irreversible capacities of $LiFePO_4$ are represented in Figure 2.8(b). Irreversible processes will affect the **Coulombic efficiency** which is defined as the ratio of the released and loaded charge during discharging and charging

$$\eta_C = \frac{C_{\text{discharge}}}{C_{\text{charge}}} \tag{2.17}$$

In other words the Coulombic efficiency is less than 1 if the conversion of charging current into utilizable reaction products is incomplete.

The **cycle life** of the electrode material corresponds to the achievable number of discharge and charge cycles (N) before reaching a lower limit,

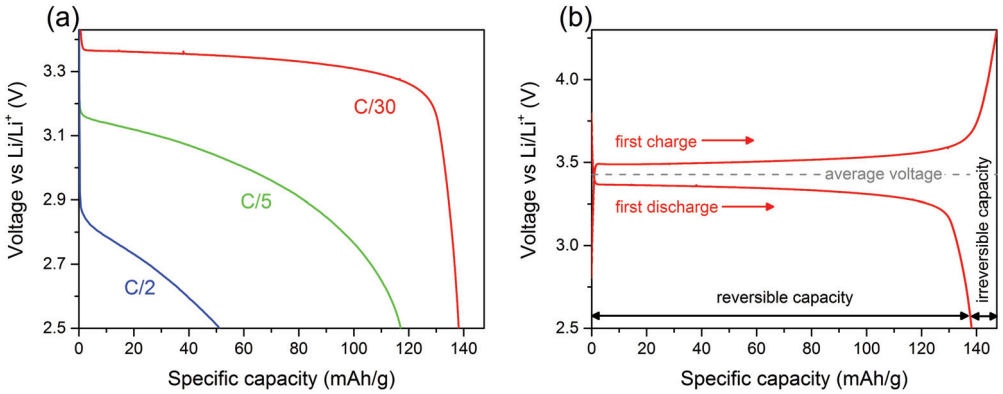

Figure 2.8: (a) Discharge voltage profiles of $LiFePO_4$ at various C-rates and (b) first cycle voltage profiles of $LiFePO_4$ at C/30 illustrating reversible and irreversible capacities as well as average operational voltage (1C corresponds to 170 mA/g).

normally set between 70 % and 80 % capacity retention which is defined as

$$R_N = \frac{C_N}{C_1} \tag{2.18}$$

If a battery (*e.g.* of an EV) should be used for 8 years with a full discharge and charge cycle every three days the Coulombic efficiency of the battery should in average be greater than 99.97 % in order to retain at least 70 % of its capacity over this period. Batteries can also degrade because of chemical side reactions during storage ("**self-discharge**") which will affect the **shelf life** and the capacity retention of the battery. The shelf life of a battery is affected by parameters such as temperature and state of charge during storage, cell design and the electrochemical system.

The equilibrium **cell voltage** is a function of the change in Gibbs free energy of the electrode material (Section 2.2.2). Typical cathode and anode materials will exhibit high voltages (>2 V) and low voltages (<2 V) *vs.* Li/Li^+ (Na/Na^+), respectively. Kinetic limitations will give rise to overpotentials (see Section 2.2.3). During discharging the voltage will be lowered and during charging it will be increased with respect to equilibrium. Average

operational voltage ($\overline{V}$) and voltage hysteresis ($\overline{\Delta V}$) are defined as

$$\overline{V} = \frac{\overline{V}_{\text{charge}} + \overline{V}_{\text{discharge}}}{2} \qquad \text{and} \qquad \overline{\Delta V} = \overline{V}_{\text{charge}} - \overline{V}_{\text{discharge}} \tag{2.19}$$

where $\overline{V}_{\text{charge}}$ and $\overline{V}_{\text{discharge}}$ are the average voltages during charge and discharge. Figure 2.8 shows the average operational voltage and voltage drop during discharge of $LiFePO_4$. The **voltage efficiency** is defined as

$$\eta_V = \frac{\overline{V}_{\text{discharge}}}{\overline{V}_{\text{charge}}} \tag{2.20}$$

The voltage efficiency is thus reduced with increasing overpotential (voltage hysteresis) *e.g.* at elevated C-rates.

The **energy density** can be expressed as $\overline{W} = C\overline{V}_{\text{discharge}}$. The greater the practical specific capacity (C) and the higher the average operational voltage during discharge ($\overline{V}_{\text{discharge}}$) the greater the battery's energy density. The larger the voltage difference between the cathode and anode the higher the cell voltage. Cathode and anode materials should thus operate at the highest and lowest possible voltages *vs.* Li/Li^+ (Na/Na^+), respectively, within the stability range of the electrolyte to yield the highest energy density. The **energy efficiency** is given as

$$\eta_W = \eta_C \cdot \eta_V \tag{2.21}$$

and will thus be affected by the same factors as Coulombic and voltage efficiencies.

Safety is a serious issue in LIB and SIB technology. Approaches to reduce safety hazards (*e.g.* venting, rupture or explosion of the cell) will depress the energy density by setting limits to C-rates and the exploitable voltage ranges. This will reduce gas production and overheating. Further, battery operation at too high or too low temperatures and short circuiting should be avoided.

The **environmental impact** such as toxicity, biodegradability, recyclability and resource depletion of battery (precursor) materials is yet another important aspect in battery technology [54].

The **cost** of a battery material / system is of crucial importance for com-

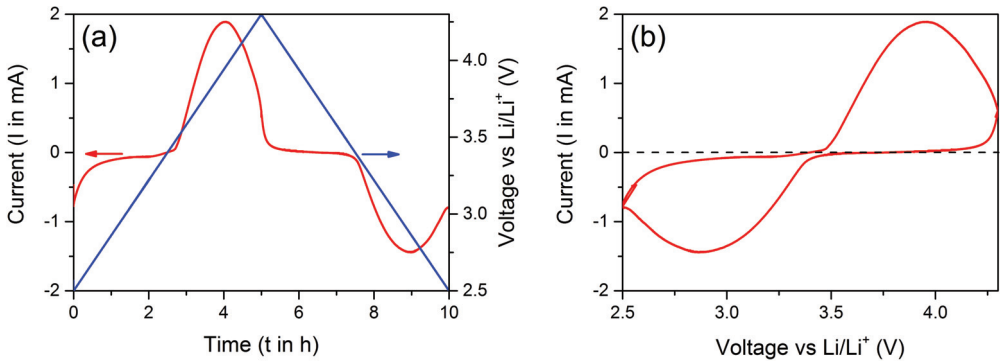

Figure 2.9: (a) Illustration of a cyclic voltammetry measurement where the voltage is controlled and the current response is measured as a function of time; (b) corresponding cyclic voltammogram of $LiFePO_4$ showing the magnitude of the current flow as a function of voltage at a sweep rate of 0.1 mV/s.

mercial applications. It is closely related to the materials energy density, voltage efficiency, cycle and shelf life as well as safety and environmental concerns.

2.4 Electrochemical methods

The electrochemical properties of battery electrode materials introduced in the previous section (Section 2.3) can be determined by simple measurement of voltage and current as a function of time of which one is commonly controlled whilst the other is monitored [37].

2.4.1 Cyclic voltammetry

In cyclic voltammetry (or linear sweep voltammetry) measurements a linearly changing voltage (ramp voltage), within set voltage limits (V_{min}, V_{max}), is applied to an electrode whilst the current response is recorded (Figure 2.9(a)). A typical cyclic voltammogram of $LiFePO_4$ is presented in Figure 2.9(b). Negative and positive current responses correspond to reduction and oxidation reactions at the electrode, respectively. The practical specific discharge

and charge capacities (C) can be obtained from

$$C = \int_{V_{\min}}^{V_{\max}} I(V) \cdot \mathrm{d}V \tag{2.22}$$

which corresponds to the area enclosed by the current response curve and the voltage abscissa at 0 mA as indicated by the dashed line in Figure 2.9(b). As the applied voltage approaches the equilibrium voltage of the redox reaction (Section 2.2.2) the magnitude of the current flow increases rapidly before becoming restricted due to limited mass transport (diffusion) capabilities in the electrode material (Section 2.2.3). Then, as the voltage is continuously swept away from the equilibrium voltage of the redox reaction, the magnitude of the current flow is decreasing. The position of the current peaks can be used to determine the reaction voltages of the redox step during reduction and oxidation. Diffusion limited reactions show an approximately symmetrical pair of current peaks with a sweep rate independent voltage separation (*e.g.* $LiFePO_4$, Figure 2.9(b)). Their voltage separation increases with the sweep rate if other kinetic limitations of the electrode processes such as charge transfer are present.

2.4.2 Galvanostatic discharge and charge

During a galvanostatic (or chronopotentiometric) discharge and charge experiment a constant current is applied to the test cell (commonly a half cell) and the voltage variation (V *vs.* Li/Li^+ (Na/Na^+)) within set voltage limits ($V_{\min}$, $V_{\max}$) is recorded as a function of time (t). The current (I) is inverted between discharge and charge. It is commonly chosen specific to the mass of active material in the electrode and the C-rate. A typical galvanostatic measurement of $LiFePO_4$ at C/30 is shown in Figure 2.10(a). Several discharge and charge cycles are performed repeatedly. The practical specific discharge and charge capacity (C) is obtained as

$$C = \int_{t(V_{\min})}^{t(V_{\max})} I(t) \cdot \mathrm{d}t = I \cdot [t(V_{\max}) - t(V_{\min})] \tag{2.23}$$

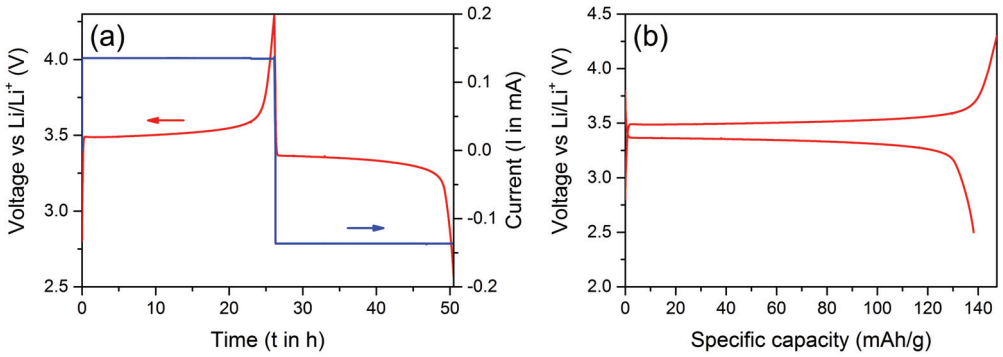

Figure 2.10: (a) Illustration of a galvanostatic measurement where the current is controlled and the change in voltage is recorded as a function of time; (b) corresponding voltage profile *vs.* specific capacity of $LiFePO_4$ at a C-rate of C/30.

The voltage response under constant applied current indicates changes in Gibbs free energy of the active material (Section 2.2.2) and in electrode processes (Section 2.2.3). The voltage profiles are commonly compared as a function of the specific capacity (Figure 2.10(b)) or the amount of Li (Na) per unit formula (x) according to Equation 2.8.

The reaction voltages during discharge and charge can best be compared by plotting the derivative of the capacity with respect to the voltage (commonly referred to as "differential capacity plot", "dC/dV plot" or " dQ/dV plot") as shown in Figure 2.11. Reaction voltages during discharge and charge are associated with negative and positive peaks in the differential capacity plot, respectively. Sharp peaks in the differential capacity plots are typical of crystalline materials showing first-order phase transitions for which the voltage plateaus are well defined whereas broadened features are associated with increasing disorder in the materials as the crystallite size decreases as well as with amorphous materials and insertion materials showing solid solution behaviour for which the voltage profiles appear more sloped (Section 2.2.2 and Figure 2.10).

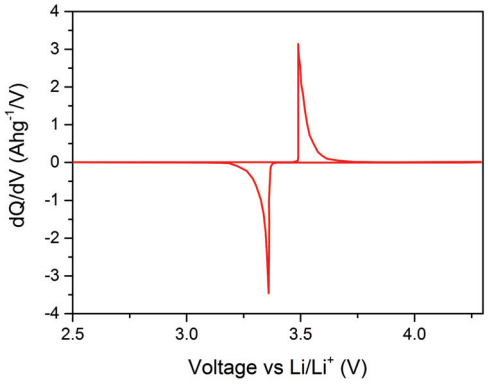

Figure 2.11: Differential capacity plot of $LiFePO_4$ at C/30 corresponding to Figure 2.10(b).

2.5 Review of sodium-ion battery materials

SIBs were initially investigated in parallel with LIBs through the 1980s [20, 55]. The lower energy densities for the same host structure (owing to the lower electrochemical potential and the higher mass of Na) and the lack of suitable anode materials for SIBs (Na does not intercalate sufficiently into graphite) directed research interests towards LIBs as the more promising technology [20]. In the 1990s LIBs were introduced to the portable electronics market, which has since grown exponentially. In recent years LIBs have also become the power source of choice for EVs and will potentially be used for large-scale stationary electrochemical energy storage. This trend raises concerns about limits to the availability of Li and transition metal (*e.g.* Co) precursor materials.

Recently SIB research regained momentum due to the discovery of hard carbons as suitable anode materials in 2000 [56] and the unique electrochemical activity of the Fe^{3+}/Fe^{4+} redox couple in 2006 [20]. SIBs could thus be made of environmentally sustainable and economically viable materials. This also includes the possibility to use inexpensive and lighter Al instead of Cu as the anode current collector since Na, unlike Li, does not alloy with Al. The main application of SIBs is foreseen in stationary electrochemical energy storage where the energy density is not as much a concern as cost.

However, recent reports have shown that some SIB systems are approaching the energy densities of LIBs [29] and they might thus also have the potential to enter the market for low-cost portable applications.

The key obstacles that need to be overcome on the way towards commercialization of SIB technology are the discovery of new electrode materials with high energy densities and their improvement, especially in terms of cycle life. Most cathode materials are based on Na insertion chemistry which means that the number of available sites in the host structure (*i.e.* the specific capacity) is limited. For cathode materials operating at high voltages another limitation is the stability range of the electrolytes. The energy densities of the most common cathode materials are thus inherently restricted by their chemistries. Anode materials on the other hand are not bound to insertion or intercalation mechanisms and much higher energy densities can be obtained using alloying and conversion materials. The greatest progress towards higher energy densities can thus be expected in the field of high performance anode materials. A remarkable number of new materials (Figures 2.12 and 2.16) and approaches were reported in the recent years which were summarized in numerous review articles [20, 21, 23, 25, 26, 28, 55, 57–64]. Some of these findings are highlighted in the following sections which focus on cathode and anode materials. Some information on Na electrolytes can be found in [55]. The oxidative stability of carbonate electrolytes is good and compatibility with cathodes is not a major concern. Due to the lack of a widely accepted anode material, systematic electrolyte studies are still scarce. The electrolytes should thus be be optimized individually for every new anode material. For many anode systems the use of fluoroethylene carbonate (FEC) as electrolyte additive can improve cycling stability.

2.5.1 Cathode materials

This section summarises some findings on insertion based SIB cathode materials such as layered oxides, polyanionic frameworks and Prussian blue analogues. Their specific capacities, average operation voltages and energy densities are compared in Figure 2.12. All families of cathode materials are in competition and represent a trade-off between energy density and long-term

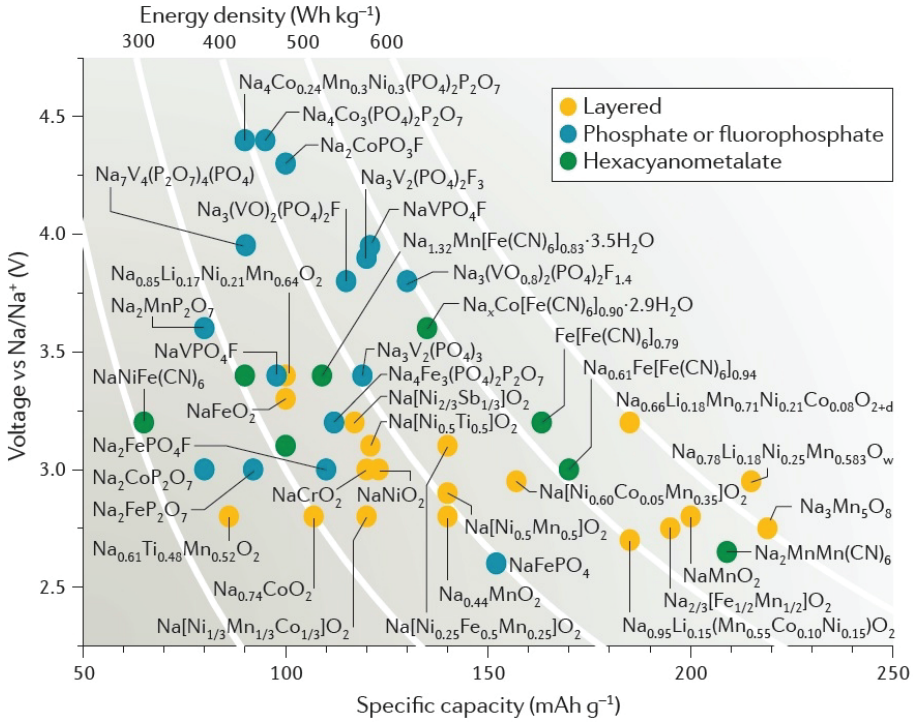

Figure 2.12: Approximate voltage, specific capacity and energy density ranges of most common SIB cathode materials [25].

cycling stability.

In the literature a few examples are also found of high voltage conversion based materials, *e.g.* fluorides [65–67]. In these materials the transition metals can be fully reduced which offers potentially greater specific capacities compared to insertion materials. On the other hand they suffer from lower cycling stability, pronounced voltage hysteresis and thus low energy efficiency. The conversion reaction mechanism is described in the section for anode materials.

Layered transition metal oxides

Layered transition metal oxides of type $NaMO_2$ (M = transition metal) are a promising family of insertion host structures for SIBs. They provide suit-

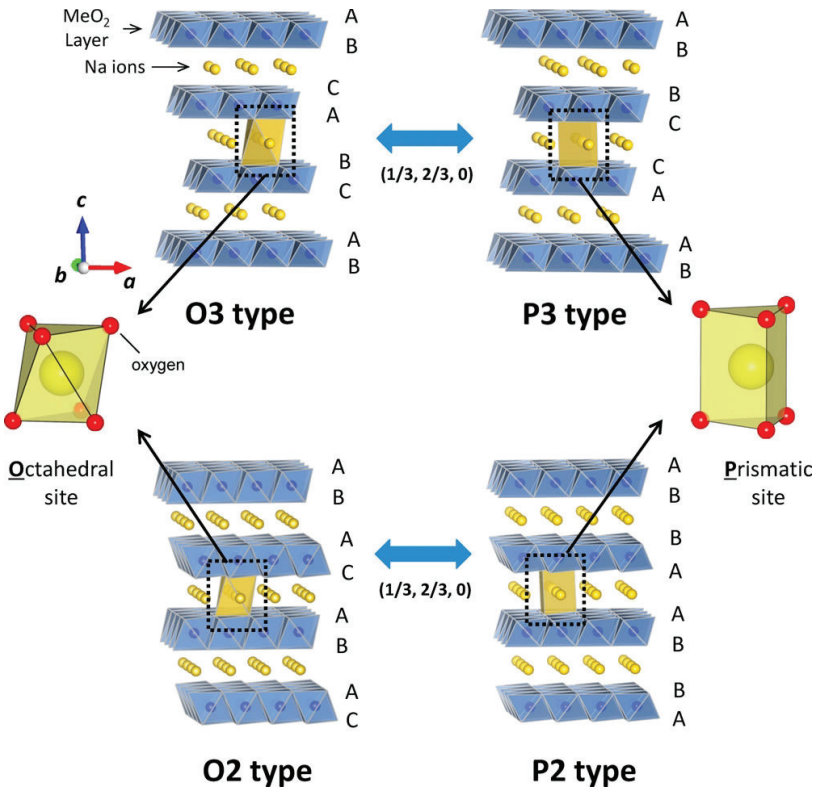

Figure 2.13: Illustration of the various layered $NaMO_2$ structure types [20].

able energy densities because of their high specific capacities at appropriate operation voltages. M can at least partially be selected from sustainable elements such as Fe and Mn and thereby reduce the use of Co. $NaMO_2$ can, depending on the close-packed oxygen layer stacking, be categorized as one of several polytypes in which the Na ion adopts either a prismatic (P) or an octahedral (O) coordination environment (Figure 2.13). The polytypes are O3 (ABCABC stacking), P2 (ABBA stacking) or P3 (ABBCCA stacking) [68]. $NaMO_2$ will most likely adopt the O3-type in which the Na and M ions are separated into different layers due to their large difference in ionic radii. Na deficient $Na_{2/3}MO_2$ adopts the P2-type because of Na vacancy ordering interactions which are more pronounced due to the large ionic size of Na. With the layered transition metal oxides further care should be taken to

avoid air/moisture contamination. The larger interlayer spacing compared to Li analogues and the empty prismatic sites in the P2-type make them prone to the uptake of gases, hydration or even decomposition [29, 55].

O3-$NaMnO_2$ can exchange 0.8 electrons per formula unit which corresponds to a capacity of 185 mAh/g but with relatively pronounced loss of capacity over the initial cycles [69]. The step-like voltage profile is associated with several two-phase regions which are more common for SIBs than for LIBs due to stronger Na vacancy ordering [69]. These structural transitions involve gliding of the oxygen planes to optimize the Na coordination in both octahedral and trigonal prismatic sites. Fewer and smoother structural transitions upon desodiation and sodiation were found for O3-$NaCrO_2$ resulting in an almost flat voltage profile in the vicinity of 3 V with a capacity of 120 mAh/g [70]. Carbon coating of the latter material resulted in similar rate performance and cycling stability compared to LIB analogues. While O3-$NaFeO_2$ shows low reversible capacities ($\sim$85 mAh/g). The capacity and cycling stability could be improved by Ni substitution [71]. O3-$NaFe_{0.3}Ni_{0.7}O_2$ exhibits 135 mAh/g capacity and the more stable cycling performance might be attributed to solid solution behaviour in contrast to a two-phase process which was observed for O3-$NaFeO_2$ [71]. Although the energy density will always be lower in $NaMO_2$ compared to $LiMO_2$ it was found for O3-$NaNi_{1/2}Mn_{1/2}O_2$ that better solid state diffusion for Na ions compared to the Li counterpart resulted in better capacity retention at elevated rates [72]. O3-$NaFe_{1/3}Mn_{1/3}Ni_{1/3}O_2$ shows a sloped voltage profile in the 1.5 V to 4 V region giving rise to a retained capacity of 100 mAh/g over 150 cycles [73].

P2-type structures can generally deliver higher capacities compared to the O3 analogue. On the other hand most P2-type structures (unlike the O3-type) are commonly synthesized in a Na deficient form which is detrimental for the energy density of full cells. Increasing the energy density would require Na compensation by strategies such as predischarge with metallic Na or the use of sacrificial salts. P2-$Na_{2/3}Mn_{1/2}Fe_{1/2}O_2$ is one of the most promising layered cathode materials [74]. It exhibits reversible capacities of 190 mAh/g and energy densities comparable to commercial $LiFePO_4$. Additionally it is made of environmentally benign and low-cost transition metals. Due to the

activity of the Fe^{3+}/Fe^{4+} redox couple a higher average operation voltage can be achieved than in P2-$Na_{2/3}MnO_2$ [75]. P2-$Na_{2/3}Ni_{1/3}Mn_{2/3}O_2$ also shows promising capacities (150 mAh/g) at high operation voltages based on Ni^{2+}/Ni^{4+} redox reaction but suffers from pronounced capacity degradation [76]. It was shown that Mn substitution by Ti could improve the cycling stability considerably. P2-$Na_{2/3}Ni_{1/3}Mn_{5/6}Ti_{1/6}O_2$ delivers 127 mAh/g reversible capacity at average operation voltage of 3.7 V [76]. It was also demonstrated that substitution of the transition metals by Li or Mg could improve battery performance. P2-$Na_{0.8}[Li_{0.12}Ni_{0.22}Mn_{0.66}]O_2$ shows solid solution behaviour and delivers 115 mAh/g reversible capacity with a retention of 90 % over 50 cycles [77]. P2-$Na_{2/3}[Mg_{0.28}Mn_{0.72}]O_2$ delivers 150 mAh/g with 96 % capacity retention over 25 cycles [78].

Polyanionic frameworks

Polyanionic compounds offer diverse open framework structures with facile Na diffusion, possibilities of tuning the operation voltage by altering the local environments, and favourable structural conditions for a flat voltage profile and good long-term cycling stability. Typically they are based on phosphates, fluorophosphates and sulphates composed of tetrahedral XO_4 or trigonal XO_3 (where X is P or S and the oxyanion may be substitued by F ions) combined with octahedral transition metal centres of the type MO_6 (or other coordination centres where M is a transition metal). An example structure is shown in Figure 2.14. The covalent nature of the polyanionic frameworks makes them thermally stable and ensures good oxidative stability at high charging voltages [55]. The greater mass of the polyanions per active transition metal results in smaller specific capacities compared to the layered oxides. The higher operation voltages attributed to the inductive effect however give rise to energy densities similar to those of the layered oxides (Figure 2.12).

$NaFePO_4$ has the highest theoretical capacity among the polyanionic compounds. It was recently shown that the stable maricite structure shows electrochemical activity. During the initial desodiation it is irreversibly transformed to amorphous $FePO_4$ which delivers reversible capacities of about 140 mAh/g over 200 cycles [79]. The metastable olivine-type structure shows

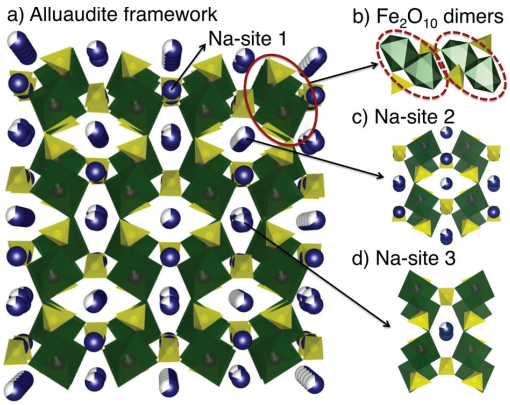

Figure 2.14: Illustration of (a) the $Na_{2+2x}Fe_{2-x}(SO_4)_3$ crystal structure consisting of interconnected FeO_6 octahedra (green) and SO_4 tetrahedra (yellow) having Na atoms (blue) in three distinct sites, (b) bridging of neighboring edge-sharing Fe_2O_{10} dimers by SO_4 units and (c/d) local coordination of Na in different partially occupied sites [29].

low average operation voltage (2.7 V) and large volume changes (∼18 %) during cycling [80]. Both materials show sluggish kinetics.

NASICON (sodium super ion conductor) compounds (corner-sharing XO_4 and MO_6 polyhedra) were initially explored as solid electrolytes due to their fast Na ion conduction along the large tunnels, but also attracted interest as cathode insertion materials [81]. Their poor electrical conductivity resulted at first in insufficient practical capacity, but this could be overcome by nanostructuring and carbon-coating [82–84]. $Na_3V_2(PO_4)_3$ is a promising candidate. It shows a flat voltage profile at 3.4 V associated with the V^{3+}/V^{4+} redox couple with a theoretical capacity of 117 mAh/g giving rise to an energy density of about 400 mWh/g. It further shows impressive rate performance as well as extremely long cycle life (50 % capacity retention over 30000 cycles at 40C) [82, 84].

Replacing one of the phosphate groups by highly electronegative fluorine lifts the voltage of the active redox couple due to stronger inductive effects in these fluorophosphates. $Na_3V_2(PO_4)_2F_3$ shows higher average operation voltage (3.9 V) compared to its NASICON counterpart [85]. $Na_3(VO_{0.8})_2(PO_4)_2F_{1.4}$ (layer-like structure) shows similar energy density,

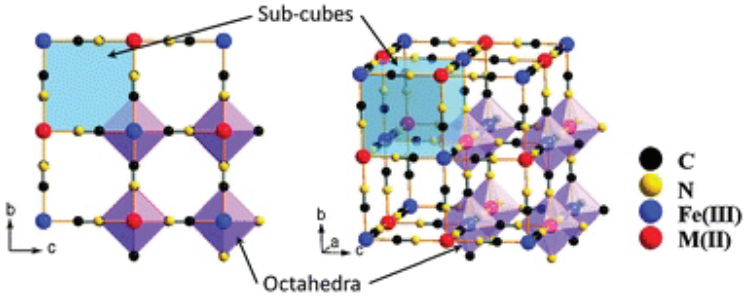

Figure 2.15: Illustration of the PBA (hexacyanometalate) framework structure [88].

low overpotentials and excellent cycling stability (84 % capacity retention over 500 cycles at 1C) are associated with fast Na diffusion and low volume changes during cycling [86].

In pyrophosphates (P_2O_7 units) even higher operation voltages can be found, but lower specific capacities limit the energy densities. A few examples are shown in Figure 2.12.

Sulphate and fluorosulphate compounds also show some promising electrochemical performance features, such as higher operation voltages due to stronger inductive effects compared to their phosphate counterparts. However, their synthesis needs to be performed in non-aqueous media due to moisture sensitivity of the sulphates. $Na_2Fe_2(SO_4)_3$ (Figure 2.14) is the most promising polyanionic compound: it has the highest reported Fe_2^{+}/Fe_3^{+} redox voltage at about 3.8 V, a solid solution process with very low volume changes (∼2 %) and good rate performance [29, 87]. It delivers a reversible capacity of 102 mAh/g and is comparable to P2-$Na_{2/3}Mn_{1/2}Fe_{1/2}O_2$ in terms of energy density [29].

Prussian blue analogues

Prussian blue analogues (PBAs), also referred to as hexacyanometalates, with general formula, $Na_xM_A[M_B(CN)_6]_y \cdot z\,H_2O$ ($M_{A,B}$ = transition metal, $x = 4y-2$, $y \leq 1$) are promising high energy density, high rate, long cycle life and low cost cathode materials for SIBs. $M_{A,B}{}^{2+}/M_{A,B}{}^{3+}$ reside on alternate corners of cage-like subunits of corner-shared octahedra linked by $(C{\equiv}N)^-$

bridges (Figure 2.15). In the M_AN_6 and M_BC_6 octahedra M_A and M_B adopt high-spin (HS) and low-spin (LS) configuration, respectively. Coordinating water resides in the randomly distributed $(1-y)$ $[M_B(CN)_6]$ vacancies (6 H_2O molecules per vacancy), while zeolitic water and Na ions can be found in the nanosized voids of the framework structure [88].

High specific capacities can in principle be achieved due to a theoretical two-electron exchange per formula unit during cycling. Reversible Na insertion and extraction has been demonstrated for M_A = Mn, Fe, Co, Ni, Cu, Zn and M_B = Fe [88–94] as well as for $Na_2Mn[Mn(CN)_6]$ [89]. Although conventionally sodiated cathode materials are preferred, the framework structure can also be synthesized free of Na (*e.g.* $Fe[Fe(CN)_6]$ [95]). Specific capacities of up to 150 mAh/g with a single plateau at 3.5 V for $Na_2Mn[Fe(CN)_6]$ [92] and 170 mAh/g with a two-staged voltage profile associated with HS and LS Fe^{2+}/Fe^{3+} at 3.1 V and 3.3 V, respectively, for $Na_2Fe[Fe(CN)_6]$ [90] were reported. For $Na_2Mn[Mn(CN)_6]$ a surprisingly high reversible capacity of 209 mAh/g was achieved [89]. This was associated with the formation of $Na_3Mn^{2+}[Mn^{+}(CN)_6]$ upon initial sodiation which allows for three-electron exchange per formula unit during cycling. The three-staged voltage profile is associated with the LS Mn^{1+}/Mn^{2+} redox couple at 1.8 V, with LS Mn^{2+}/Mn^{3+} at 2.7 V and HS Mn^{2+}/Mn^{3+} at 3.6 V. PBAs with high energy densities can thus be achieved due to high specific capacity and high operation voltages. The Na ions diffuse in the three dimensional tunnel network across the open faces of the cage-like subunits formed by the $(C{\equiv}N)^{-}$ ligands which compared to O^{2-} ions interact less with diffusing Na^{+} ions [89]. This results in high rate capabilities for this class of materials, see for example [89, 90, 92–95]. Due to their open structure, volume changes are expected to be smaller than in the other insertion compounds which should result in more stable cycling stability [55]. It was found that the cycling stability could be improved considerably by improving synthetic conditions which affect the water content, the number of vacancies and the crystallite size. High cycling stability over several hundreds of cycles was observed for samples with composition $Na_2M_A[M_B(CN)_6]$ [89, 90, 92] and other samples with only small fractions of $[M_B(CN)_6]$ vacancies and high crystallinity [93–95]. Another advantage is the use of inexpensive transition metals and the simplicity

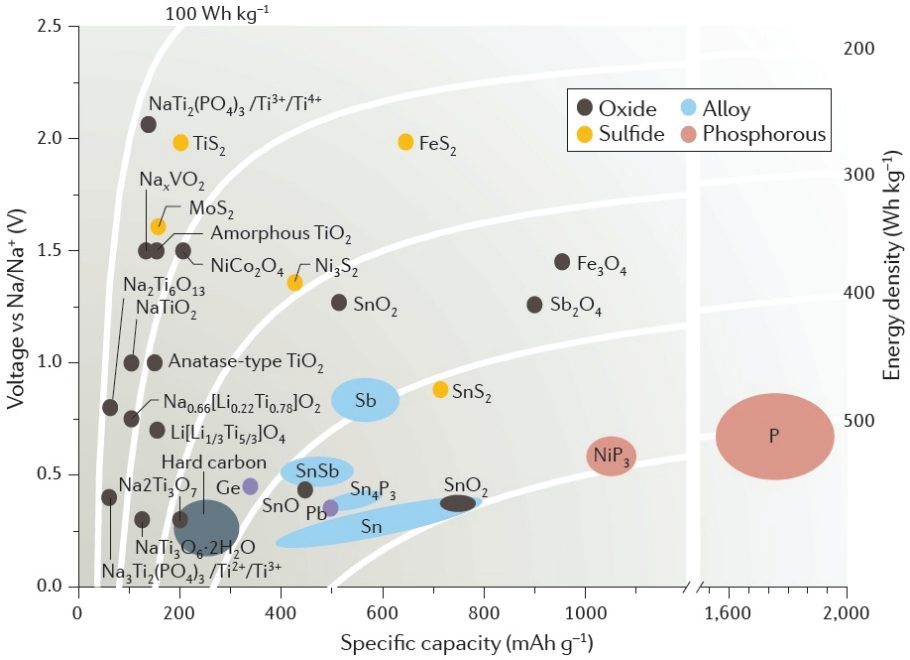

Figure 2.16: Approximate voltage, specific capacity and energy density ranges of most common SIB anode materials [25].

of synthesis of the PBAs, which gives rise to low cost per energy unit.

2.5.2 Anode materials

This section summarises some findings in the field of SIB anode materials. Depending on their reaction mechanisms (*i.e.* insertion, alloying, conversion) they span different ranges in specific capacity, voltage and energy density as compared in Figure 2.16.

Hard carbon is currently the state of the art anode used in full cells. It has, however, issues related to safety and rate performance. The aim is therefore to develop other anode materials with high specific capacity, optimal operating voltage in the 0.2 V to 0.6 V range, high initial Coulombic efficiency (above 85 %), long cycle life, and high rate capability. The suggested voltage range is a compromise between safety and energy density. A high initial Coulombic efficiency is important for full cells with a limited Na

inventory. A low initial Coulombic efficiency will therefore give rise to a low overall cell capacity.

Metallic Na

Metallic Na is not suitable as anodic material for SIBs because of interface ageing problems and voltage polarization effects due to the high reactivity of metallic Na with the organic electrolyte solvents [96], dendrite formation during metal deposition (plating which can lead to internal short circuiting of the electrodes), exothermic reaction releasing hydrogen if exposed to moisture and further safety hazards related to the low melting point of Na metal (98 °C *vs.* 181 °C for Li) [21, 57].

Carbon-based materials

Several carbon-based anodes other than graphite have been suggested for SIBs. The best performance was found for disordered hard carbons, *e.g.* prepared by the pyrolysis of biomasses such as sucrose [28]. Hard carbon is the most commonly used material in full cells (*e.g.* [97]) and serves as a reference for studies of other anode materials. Hard carbons exhibit reversible capacities of up to 300 mAh/g in SIBs which are comparable to those of graphite in LIBs (372 mAh/g or 750 mAh/cm^3 for LiC_6) at a relatively low average operation potential and with relatively high initial Coulombic efficiency (∼80 %) [63]. Two different insertion mechanisms were associated with the sloping and plateau regions in the voltage profile shown in Figure 2.17 [56, 98]. Intercalation in the graphitic regions with varying insertion-site potentials gives rise to the sloping region between 1 V and 0.2 V. The plateau region close to the Na plating potential (∼ 0.1 V) is observed due to Na absorption within the nanopores of hard carbon [28]. However, the low operation voltage is problematic with respect to safety concerns and high-rate capability due to risk of Na plating (≤ 0.1 V) during sodiation and removal of Na from enclosed pores in the "house of cards" structure. The low volumetric capacity (450 mAh/cm^3) is a further disadvantage.

Due to its larger ionic size Na does not intercalate sufficiently into graphite [21, 99]. However, if the spacing between the graphene layers is expanded *e.g.*

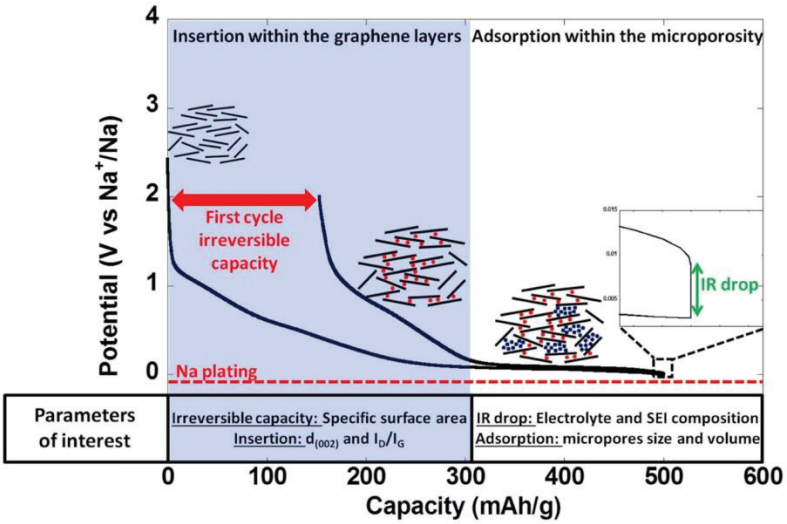

Figure 2.17: Typical voltage profile of hard carbon and illustration of insertion mechanisms [63].

by partial reduction of graphene oxide Na can enter the interlayer spaces [100, 101]. At an optimal interlayer spacing of 4.3 Å expanded graphite exhibits a reversible capacity of 284 mAh/g at a current density of 20 mA/g dropping to 184 mAh/g at 100 mA/g. At the higher current density 74 % of the initial capacity is retained after 2000 cycles [101]. During Na intercalation a sloping voltage profile is observed from 1.5 V to 0 V. This voltage profile is associated with increased safety but lower energy density compared to hard carbon.

Other disordered soft carbons with a degree of graphitization obtained by pyrolysis of aromatic compounds or polymers such as petroleum cokes [99], carbon black [102], ground pitch-derived carbon fibers and graphite [103] can accommodate Na insertion. These materials generally show sloping voltage profiles and reversible capacities of up to 120 mAh/g. Their low first cycle Coulombic efficiency is due to their low surface area and is mainly attributed to irreversibly trapped Na in the soft carbon and not to SEI formation; commonly the dominating effect in nanostructured materials with high surface areas. Other types of carbonaceous anodes such as nanostructured and doped carbons are reviewed in [28]. Conductive carbons are commonly ad-

ded as part of the electrode formulation, *e.g.* reduced graphene oxide is often used to anchor alloying or conversion anode materials (see below).

Low voltage insertion materials

Carbon-free insertion materials based on transition metal (*i.e.* V and Ti) oxides and phosphates show improved safety due to higher average operation voltages and higher volumetric energy densities compared to hard carbons. On the other hand a limited number of available sites in the host structure and relatively high insertion voltages restrict the gravimetric energy densities of this class of anode materials. In comparison to other materials they range lowest in energy density (Figure 2.16). Their long-term cycling stability also remains an issue, though in some cases this can be improved by carbon coating and nanostructuring [28].

V-based examples are P2-$Na_{0.7}VO_2$ or O3-$NaVO_2$ with a theoretical capacity of about 120 mAh/g and average operation voltage of 1.7 V [104]; and $Na_3V_2(PO_4)_3$, which shows a capacity of 60 mAh/g with an average operation voltage of 1.6 V [105]. These average operational voltages are too high for practical anode materials.

Lower voltages can be obtained using Ti-based compounds. $Na_2Ti_3O_7$ exhibits capacities of 177 mAh/g close to its theoretical value with an extraordinarily low average operation voltage of ∼0.3 V [106]. $Na_2Ti_3O_7$ thereby possesses the highest energy density among the non-carbonaceous insertion anode materials. Other examples based on the Ti^{3+}/Ti^{4+} redox couple include $NaTiO_2$ (152 mAh/g at ∼1.1 V) [107] and $Na_2Ti_6O_{13}$ (65 mAh/g at ∼0.8 V) [108]. In $NaTi_2(PO_4)_3$ both the Ti^{3+}/Ti^{4+} and the Ti^{2+}/Ti^{3+} redox couples were found to be active. This results in a two-staged voltage profile with 132 mAh/g at ∼2.1 V and 60 mAh/g at ∼0.4 V, respectively, allowing for setting up a symmetrical cell with an operation voltage of ∼1.7 V [109]. The operation voltage of the Ti^{3+}/Ti^{4+} redox couple is higher compared to the oxides, due to the inductive effect in phosphate when the same redox couple is used. More examples of insertion anode materials can be found in [20].

Alloying materials

Alloying anode materials such as Si, Ge, Sn, Pb, P, Sb, Bi and some of their composites yield higher gravimetric and volumetric capacities compared to insertion-based materials since one anode atom can combine with several Na atoms. They further operate at low redox voltages which results in the highest energy densities for this class of anode materials. At the same time alloying materials suffer from multiple phase transitions and large associated volume changes during sodiation and desodiation. This can lead to cracking of the alloy particles (also referred to as "pulverization" or "electrochemical grinding") or detachment of parts of the electrode film and thereby cause loss of reversible capacity [23, 28]. Careful selection of binder and carbon matrix plays a key role in compensating for the large volume changes and the low electrical conductivity of all or some phases present during electrochemical cycling. Stability can also be improved by lowering the upper cut-off voltage and the addition of FEC to the electrolyte in many alloying systems. FEC helps to form a stable SEI on the electrode particles even when expansion and shrinking mean that new surfaces can be exposed to the electrolyte in each cycle [23].

The highest theoretical capacity (2596 mAh/g and 5893 mAh/cm^3) in these systems is found for Na alloying with red P to Na_3P which is associated with a volume expansion of 308 %. Experimental results show that an amorphous red phosphorus/carbon nanocomposite exhibits as much as 1890 mAh/g capacity at an optimal average operating voltage of 0.4 V with high initial Coulomb efficiency (85 %), high rate capability, and considerable cycling stability [110, 111]. About 1000 mAh/g were retained after 140 cycles [111]. Reversible cycling was also reported for red P mixed with carbon nanotubes (CNTs) [112]. The large expected volume changes were accommodated by the carbon matrix and the poly(acrylic acid) (PAA) and carboxymethyl cellulose (CMC) binder, respectively. Recently progress was made for black phosphorus by forming a composite with carbon black and CNTs [113]. A very high initial Coulombic efficiency of 90 %, good high rate capabilities and a capacity retention of 1700 mAh/g after 100 cycles were found. Another interesting approach is the use of hybrid materials made out of phosphorene-graphene layers, which show good cycling stability [114]. *Ab*

initio calculations predict possible phases forming during sodiation of phosphorus [115, 116]. Apart from the crystalline Na_3P phase their often amorphous/nanocrystalline nature makes it difficult to verify them experimentally. It is noteworthy that Na_3P as the reaction product releases flammable and toxic phosphine (PH_3) upon hydrolysis which might limit its practical use [20].

Sn can alloy with Na to $Na_{15}Sn_4$ giving a theoretical capacity of 847 mAh/g (1210 mAh/cm^3). Multiple phase changes and high volume expansion of 420 % may pose a problem for long-term cycling stability [61]. Furthermore, most of the sodiation takes place at voltages below 0.2 V which increases the risk of Na plating and might reduce rate performance. Stable cycling for the first 10 cycles with high capacities of about 610 mAh/g was found using a conducting polymer (poly(9.9-dioctylfluorene-co-fluorenone-co-methylbenzoic ester) (PFM)) [117]. A sloped voltage profile, high-rate capabilities and stable capacity of about 415 mAh/g over 500 cycles at 1000 mA/g were reported for Sn nanoparticles embedded in carbon [118]. In both cases the initial Coulombic efficiency is relatively low (about 70 %). Wang *et al.* used *in situ* transmission electron microscopy to verify that the Sn particles could accommodate the volume changes without cracking [119]. *In situ* structural analysis revealed that the reaction mechanism depends on the degree of crystallinity and that kinetic effects prevent the formation of the thermodynamically stable phases present in the Na–Sn phase diagram [119–121].

Sb can form a Na_3Sb alloy resulting in 660 mAh/g (1120 mAh/cm^3) theoretical capacity with a volume expansion of 290 %. High cycling stability at capacities of about 600 mAh/g at an average operation voltage of 0.8 V and high initial Coulombic efficiency (about 80 %) were reported for antimony/carbon nanocomposites and micrometric Sb (slurry prepared by planetary milling of Sb, CMC and vapour ground carbon fibres) in combination with FEC as electrolyte additive [122, 123]. Different lithiation and sodiation mechanisms for Sb result in better cycling stability of Sb *vs.* Na [123, 124]. The lithiation of Sb follows the Li–Sb equilibrium phase diagram, with the formation of Li_2Sb and Li_3Sb, while during delithiation Li_3Sb converts directly back to Sb. During sodiation and desodiation of Sb several intermediate amorphous phases are formed between Sb and Na_3Sb [125]. The amorphous

intermediate phases help to reduce the anisotropic mechanical stress during cycling and thereby contribute to more stable cycling behaviour [124].

Pb can alloy with Na to form $Na_{15}Pb_4$ giving rise to a theoretical capacity of 485 mAh/g (1182 mAh/cm^3) at an average voltage of 0.4 V with a volume change of 360 %. Pb was investigated as early as 1987 as an alloying anode for SIB and showed stable cycling performance starting from the sodiated compound and limiting the voltage window [126]. The reaction mechanism was later assigned to reversible formation of $NaPb_3$, NaPb, Na_9Pb_4 and $Na_{15}Pb_4$ corresponding to the four steps in the voltage profile [127]. In this study Pb was used as the starting compound and low reversibility was attributed to catalytic electrolyte decomposition at the Pb surface [127].

Bi alloys with Na to form Na_3Bi, which gives a theoretical capacity of 385 mAh/g (1075 mAh/cm^3) at an average voltage of 0.6 V with only 250 % volume expansion. Bi particles embedded in graphene exhibited 358 mAh/g specific capacity within a voltage range of 0.9 V to 0.3 V with reasonable cycling stability and good rate performance [128]. Lithiation and sodiation mechanisms for Bi have been reported. The lithiation of Bi follows sequential formation of LiBi and Li_3Bi according to the Li–Bi equilibrium phase diagram. In contrast to the delithiation of Li_3Sb, the delithiation mechanism of Li_3Bi was found to be is fully reversible [129]. Reports on the sodiation mechanism for Bi are inconsistent. Ellis *et al.* reported that the sodiation and desodiation mechanisms reversibly follow the Na–Bi equilibrium phase diagram with the formation of NaBi and Na_3Bi [127]. Su *et al.* suggested Na intercalation in between Bi layers along the *c*-axis [128].

Si and Ge are the two most promising alloying anode materials for LIBs but are less attractive for SIBs. Si and Ge can theoretically be alloyed with Na to NaSi (954 mAh/g) and NaGe (369 mAh/g) at voltages of ∼0.1 V and ∼0.4 V, respectively [130]. The low sodiation voltage of Si is problematic with respect to polarization, giving rise to safety concerns and low achievable capacities compared to the theoretical value. The highest obtained reversible capacity in Si nanoparticles was 279 mAh/g [131]. Ge nanorods and thin films could deliver capacities close to the theoretical value [132, 133].

Battery performance can in many cases be improved by forming "inactive-active" binary alloys such as $Sn_{0.9}Cu_{0.1}$ [134], AlSb [135], Mo_3Sb_7 [136], and

Cu_2Sb [137, 138] as well as "active-active" binary alloys such as Sn_4P_3 [139–141], SnSb [142–144] and SbBi [145]. In the inactive-active binary alloys some capacity is lost due to the introduction of inactive mass but the inactive element can help to suppress aggregation of the nanoparticles during repeated sodiation and desodiation cycles, resulting in better cycling stability. In the active-active binary alloys higher capacities are achieved and, in addition to (usually) better cycling stability, the voltage profile can be positively affected. For Sn_4P_3 average operational voltage is lowered *vs.* P, resulting in higher energy density and raised *vs.* Sn, increasing safety.

Conversion materials

High capacities can also be achieved in materials (*e.g.* oxides, sulfides, phosphides) undergoing so-called conversion reactions with Na. They can be divided into two types. The first type is described by

$$\mathrm{M}_a\mathrm{A}_b + (bc)\,\mathrm{Na}^+ + (bc)\,\mathrm{e}^- \rightleftharpoons a\,\mathrm{M} + b\,\mathrm{Na}_c\mathrm{A} \tag{2.24}$$

where M is an "inactive" transition metal (*e.g.* Fe, Ni, Co or Cu) and A is a non-metal (*e.g.* F, O, S, N, P, H). The full reduction of the transition metal during sodiation generally leads to higher capacities compared to insertion based materials. In the second type M is an "active" alloying metal (*e.g.* Sn, Sb, Bi) which results in even higher capacities due to a combination of conversion and alloying reactions. These can be expressed as

$$\mathrm{M}_a\mathrm{A}_b + (bc)\,\mathrm{Na}^+ + (bc)\,\mathrm{e}^- \rightleftharpoons a\,\mathrm{M} + b\,\mathrm{Na}_c\mathrm{A} \tag{2.25}$$

$$a\,\mathrm{M} + b\,\mathrm{Na}_c\mathrm{A} + (ad)\mathrm{Na}^+ + (ad)\,\mathrm{e}^- \rightleftharpoons a\,\mathrm{Na}_d\mathrm{M} + b\,\mathrm{Na}_c\mathrm{A} \tag{2.26}$$

$$\mathrm{M}_a\mathrm{A}_b + (bc{+}ad)\,\mathrm{Na}^+ + (bc{+}ad)\,\mathrm{e}^- \rightleftharpoons a\,\mathrm{Na}_d\mathrm{M} + b\,\mathrm{Na}_c\mathrm{A} \tag{2.27}$$

In these equations intermediate phases that might form during sodiation depending on the parent compound were intentionally omitted. During the conversion of $\mathrm{M}_a\mathrm{A}_b$ the metal forms nanoparticles which are embedded in a $\mathrm{Na}_c\mathrm{A}$ matrix. Distances, thereby, remain small enough to allow for a reversible reaction of the otherwise non-conducting $\mathrm{Na}_c\mathrm{A}$. The mechanism is

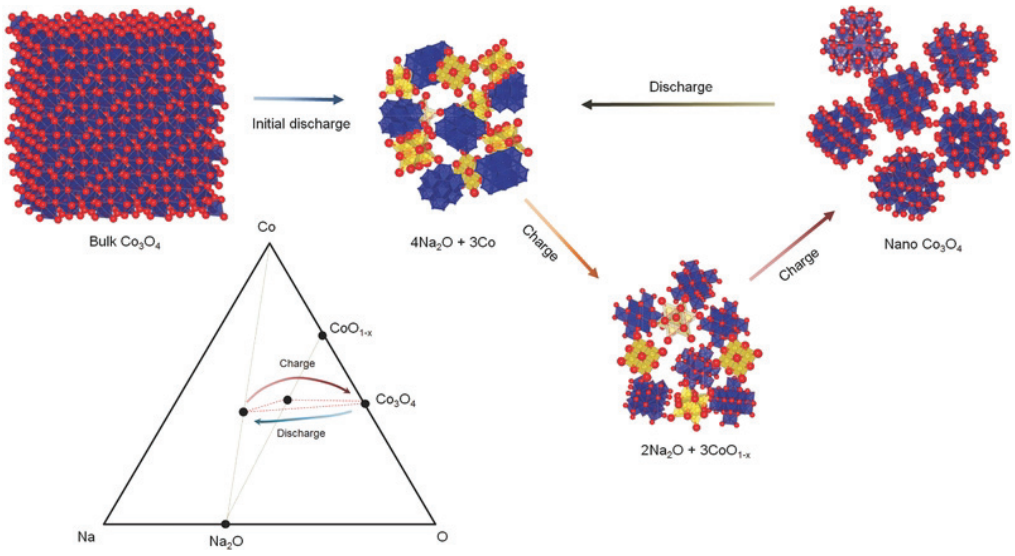

Figure 2.18: Illustration of the Na conversion reaction mechanism in Co_3O_4. Co, O and Na atoms are shown in blue, red and yellow, respectively [44].

illustrated in Figure 2.18. Often the practical capacities exceed the theoretical ones which might be associated to a capacitive effect at the interfaces of the nanoparticles and electrolyte decomposition. For the same M the voltage generally decreases with the ionicity of the bond, *i.e.* fluorides exhibit the highest voltages (∼3 V) and are commonly studied for use as cathode materials [65–67]. Oxides, sulphides and phosphides operate below 2 V which is in the range suitable for anodes. Conversion reactions generally suffer from low first cycle Coulombic efficiencies (<75 %), insufficient cycling stability and poor energy efficiency due to large overpotentials [146]. The overpotential also increases with the inonicity of the M−A bond. In LIBs with Co_aA_b the voltage hysteresis decreases in the order F (∼1.1 V), O (∼0.9 V), S (∼0.7 V), N (∼0.6 V), P (∼0.4 V), H (∼0.3 V) [147]. Klein *et al.* compared thermodynamic properties (cell voltages, capacities, energy densities) of possible cell reactions of conversion materials in SIBs and LIBs. The cell voltage for oxides is theoretically expected to be lowered by as much as 1 V, while it is only reduced by 0.4 V for fluorides, sulphides and hydrides in a SIB with respect to the LIB analogue. Oxides might thus be of particular interest due to the

increased energy density.

Many transition metal oxide anodes inspired by the LIB technology did not have the same success in SIBs [28]. Examples with relatively small capacities (mainly below 400 mAh/g in spite of their high theoretical capacities) and low cycling stability include Fe_2O_3, Mn_3O_4, Co_3O_4 and NiO [148], MoO_3 [149], $NiCo_2O_4$ [150] and Fe_3O_4 [151]. Progress with respect to the cycling stability and rate performance was recently reported for nanodots of $MnFe_2O_4$ in carbon nanofibers [152]. As much as 90 % of the capacity was retained over 4200 cycles when cycled at a specific current of 2000 mA/g in a voltage range of 0.01 V to 3 V. It is commonly found that the oxide anodes are cycled to voltages of up to 3 V with considerable capacity contribution above 2 V which makes these systems only suitable in conjunction with high voltage cathodes. Transition metal sulphides include FeS_2 [153], Ni_3S_2 [154], MoS_2 [155] and WS_2 [156]. The nanostructuring and embedding of the sulphides in carbon nanofibers or on graphene is crucial for the battery performance.

Several reports on alloying oxides and sulphides are found in the literature. These include Ni_3P [157], Bi_2O_3 [158], Bi_2S_3 [159], Sb_2O_4 [160], Sb_2S_3 [161], SnO_2 [162], SnS_2 [163]. Better cycling stability was generally obtained for the sulphides. Remarkable rate performance and cycling stability was recently reported for a SnS/SnO_2 heterostructure [164]. At a specific current of 2430 mA/g about 76 % of the capacity is retained over 500 cycles.

2.6 Review of advanced *operando* characterization

Understanding of the working and degradation mechanisms of both electrode materials and electrolyte solutions is fundamental to develop better batteries with longer cycle life. The key to this is the investigation of these mechanisms *in situ* during operation (also called *operando*).

Ex situ characterization also plays an important role in the analysis of battery materials but has several drawbacks when compared to *operando* measurements: during preparation of samples for *ex situ* characterization the highly reactive electrode species may have relaxed, been short circuited or contaminated with atmospheric species. Further, a limited number of samples of the same material at different charge states for *ex situ* character-

izations may miss a lot of fine details between the sampling points. *Operando* characterization avoids these problems: short-lived intermediates and non-linearities in behaviour can be resolved (subject to the time resolution of the measurements); different charge rates can be applied and time dependent processes under non-equilibrium conditions can be studied; long term cycling experiments become practically feasible and activation/degradation processes can be investigated. However, in order to perform *operando* measurements on batteries, specially designed electrochemical cells and set-ups are normally required. The *operando* battery configurations might in some case have limited comparability to conventional cells [165]. In some cases beam damage to the electrode material, electrolyte or polymeric binder *e.g.* by exposure to hard X-rays, may affect the results [166].

Operando studies are a significant part of current battery research. A broad range of advanced characterization techniques is currently available for these *operando* investigations. These methods and how they contributed to our understanding of electrode systems have been reviewed in several articles [165–173]. Harks *et al.* list the available *operando* methods and the materials that have been investigated since 2009 using the respective methods in Table 1 of their review article [165]. They further provide a short description of each method and the electrochemical cell designs. Weker and Toney focus on the emerging *operando* imaging techniques [166]. In the following, some key examples of *operando* studies (with a focus on X-ray based methods) will be presented in the context of the information they reveal on working and degradation mechanisms in batteries.

As introduced in the previous sections of this chapter, lithiation/sodiation of electrode materials can involve the formation of solid solutions, phase transitions, or conversion reactions. Powder diffraction and total scattering (with X-rays or neutrons) are perfectly suited to pinning-down the nature of the reaction process (single *vs.* multi-phase), its associated structural changes (atomic arrangement, volume) and its reversibility upon cycling. These are critical factors affecting the battery performance *i.e.* the voltage profile and capacity retention. Different reaction paths during discharging and charging will lead to voltage hysteresis and hence to loss in energy efficiency (Section 2.2.3). X-ray and neutron diffraction are the *operando* techniques

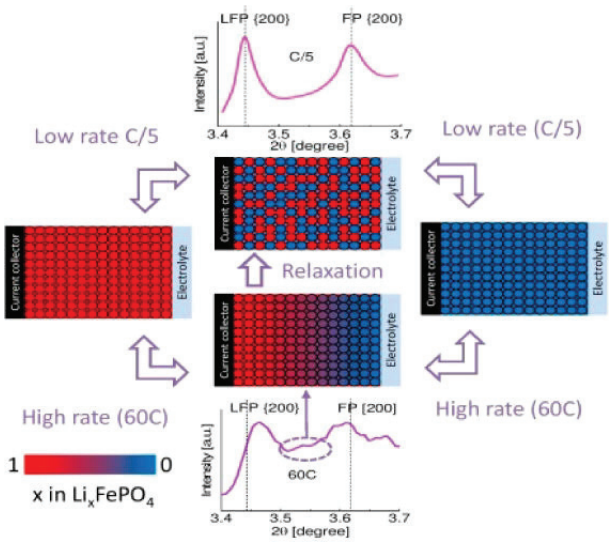

Figure 2.19: Model for the phase distribution in $LiFePO_4$ electrodes at high and low rates and upon relaxation [174].

most commonly used to study the working mechanisms of a broad range of crystalline electrode materials (Table 1 in [165]). Further examples are provided in this dissertation in which different material-related properties such as vacancy and water content, crystallite size and nanostructuring were found to affect the structural chemistry during cycling (Chapter 5). As indicated in Section 2.2.3, the structural response of the electrode material upon cycling might deviate from what is know for equilibrium conditions if large C-rates (giving rise to overpotentials) are applied to an electrode. Zhang *et al.* provided a thorough investigation on the effect of increasing C-rates on the phase transformations in $LiFePO_4$ (Figure 2.19) [174]: at equilibrium conditions (<2C) they observe a first order phase transition between the end members $FePO_4$ and $LiFePO_4$; at intermediate rates they find a metastable phase with composition $Li_{\sim 0.6}FePO_4$; and solid solution behaviour at elevated rates (>10C). Using *operando* microbeam XRD Zhang *et al.* studied the rate-dependent phase transition mechanism within individual electrode grains [175]: at low rates (<C/5) individual electrode grains transform very slowly and concurrently via coexisting platelet-shaped phase

domains and at high C-rates (>2C) the platelet-shaped domains make room for diffuse interphases proving a distribution of instable intermediate phases within a single electrode grain. Microbeam/Nanobeam diffraction has also been applied to lithium-oxygen batteries [176, 177]. *Operando* total scattering provides a means of studying the working mechanism in electrode systems involving non-crystalline amorphous (intermediate) phases. This method was first employed by Borkiewicz *et al.* [178].

Operando XAS including XANES and EXAFS has increasingly been used to study the changes in electronic and local structure of electrode materials during cycling [179–181]. XAS methods are well established for insertion electrodes [182–185] and were central in the elucidation of reaction mechanisms in conversion materials [186–188]. EXAFS probes the short range order in the vicinity of specific elements and enables us to follow the evolution of inter-atomic distances (*e.g.* geometric distortions due to Jahn-Teller active transition metal species) in the electrode materials as a function of charge state (`Paper I`).

Nuclear magnetic resonance spectroscopy (NMR) is another method for probing changes in element specific local environments during cycling [189]. Ogata *et al.* used *operando* NMR to reveal the working mechanism of a Si nanowire electrode by identifying various amorphous and crystalline intermediate phases formed during electrochemical cycling [190].

Combining complementary techniques to study electrode systems provides deep insights into their working mechanisms: Allan *et al.* combined *operando* total scattering and *ex situ* NMR analysis to elucidate the working mechanism in the Na–Sb system [125]. Sodiation and desodiation evolve via the formation of composites of crystalline and amorphous phases (Figure 2.20). The combination of the two methods allowed solution of the structure of previously uncharacterised amorphous phases; Wiaderek *et al.* used *operando* total scattering and small angle X-ray scattering (SAXS) to probe the atomic and nanoscale structure, respectively, in Fe-based conversion electrodes [191]. By this combination they could understand the link between chemistry and structure across multiple length scales of different Fe anion and mixed anion systems. They found that the anion chemistry of the initial electrode governs the Fe particle size and nanostructure by influencing

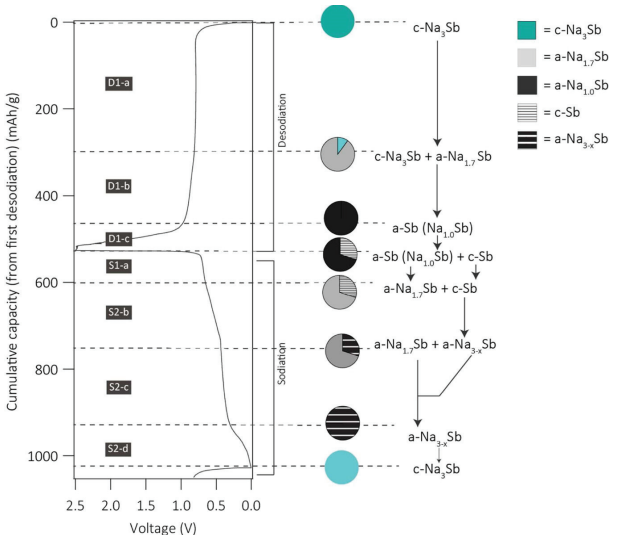

Figure 2.20: Total scattering and NMR-derived working mechanism of Sb from the first desodiation during galvanostatic cycling at a rate of C/20. Amorphous phases are labelled with a, while crystalline phases are labelled with c[125].

defect formation, annealing, atomic mobility and particle growth rates; Lee *et al.* report similar findings for NiF_2 and NiO-doped NiF_2 conversion electrodes obtained using combined XAS and total scattering analysis [192]; Hu *et al.* combined *operando* total scattering, XAS and *ex situ* NMR characterization to identify the major sources of the additional capacity that has been observed in the RuO_2/Li cell [187]. RuO_2 undergoes a conversion reaction to form Ru nanoparticles and Li_2O. The excess capacity was attributed to OH groups on the surface of the RuO_2 particles reacting with Li to form LiOH which is further reversibly converted to Li_2O and LiH; In this dissertation we use combined *operando* XRD and XAS analysis to study the reaction processes of various cathode and anode materials (Chapter 5).

Degradation mechanisms in a battery are associated with chemical and mechanical changes in the electrode or electrolyte decomposition at the interface between electrode and electrolyte [25, 51] (Figure 2.21).

Large volume changes and pronounced structural phase transitions are often held responsible for loss of reversible capacity due to pulverization of

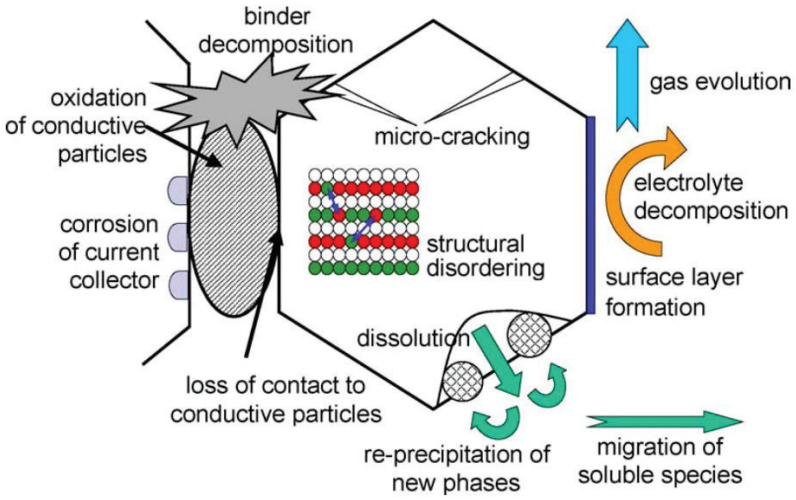

Figure 2.21: Overview of basic mechanisms reducing the cycle life of a battery [51].

electrode particles (micro-cracking) and detachment of active materials from the electrode film. This will lead to the observation of inactive residual phases and crystallite size reduction in the diffraction pattern. The precipitation of new phases after dissolution of some species can also be detected.

Morphological evolutions during cycling can be probed by *operando* X-ray absorption tomography. Ebner *et al.* observed the cracking of SnO particles (initially $\sim$10 μm) in a conversion electrode during cycling using micrometre resolution X-ray tomography (Figure 2.22) [193]. They could further obtain chemical information on the working mechanism by plotting the normalized attenuation coefficient during cycling. Weker *et al.* studied the evolution of Ge particles in an alloying electrode during cycling but using nanometre resolution X-ray tomography [194]. They found that the small and medium particles formed during the first cycle due to particle cracking remain electrochemically inactive (no volume changes) during subsequent cycles, suggesting that they became electrically disconnected from the electrode.

Many chemical and microstructural changes in electrode particles occur without significant morphological changes. These can be locally resolved

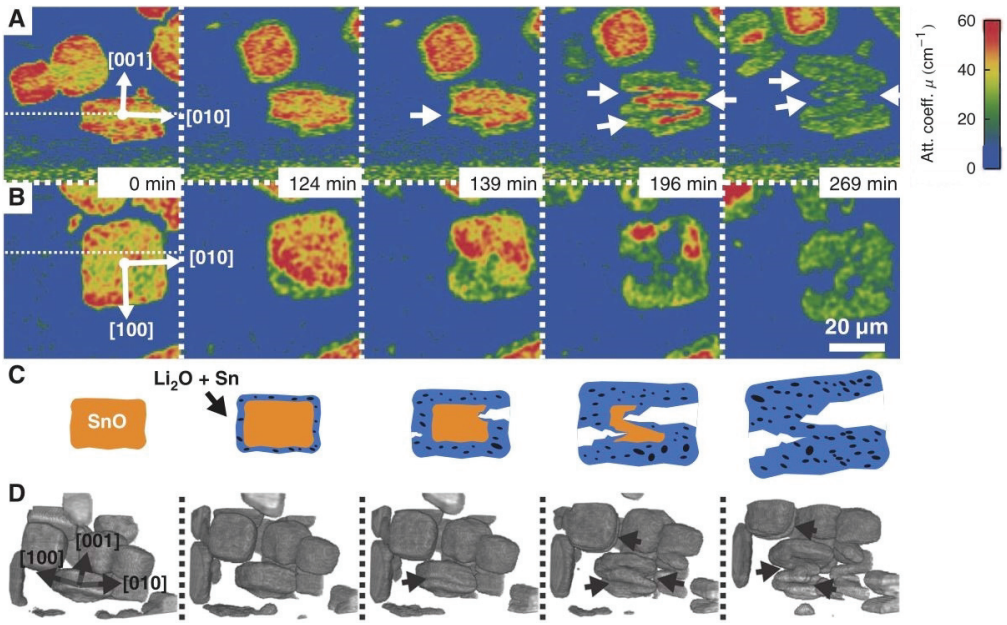

Figure 2.22: X-ray tomographic images of SnO particles: (a) vertical and (b) horizontal cross sections; (c) schematic representation of the phase evolution and particle cracking; and (d) sub-volume of the electrode rendered in three dimensions. Adapted from [193].

with nanometre resolution using *operando* X-ray microscopy. A description of the available X-ray microscopy techniques and *operando* electrochemical cells can be found in [166]. Chemical changes are commonly obtained using XANES. Wang *et al.* used X-ray microscopy coupled with XANES to investigate the phase transformation behaviour in $LiFePO_4/FePO_4$ electrodes at different C-rates [196]. They found that the transformation of the particles (200-300 nm) occurs concurrently from multiple sites at slow C-rates, while at fast rates there are distinct $LiFePO_4$ and $FePO_4$ regions extending from one site. Due to overlapping of many particles it was, however, impossible to resolve the chemistry of individual particles. Yu *et al.* studied single crystals of $Li_{1+x}Mn_{2-x}O_4$ using X-ray microscopy coupled with XANES [197]. They could thereby reveal the origins of the cracking in $Li_{1+x}Mn_{2-x}O_4$ during structural phase transitions and non-equilibrium pathways owing to the

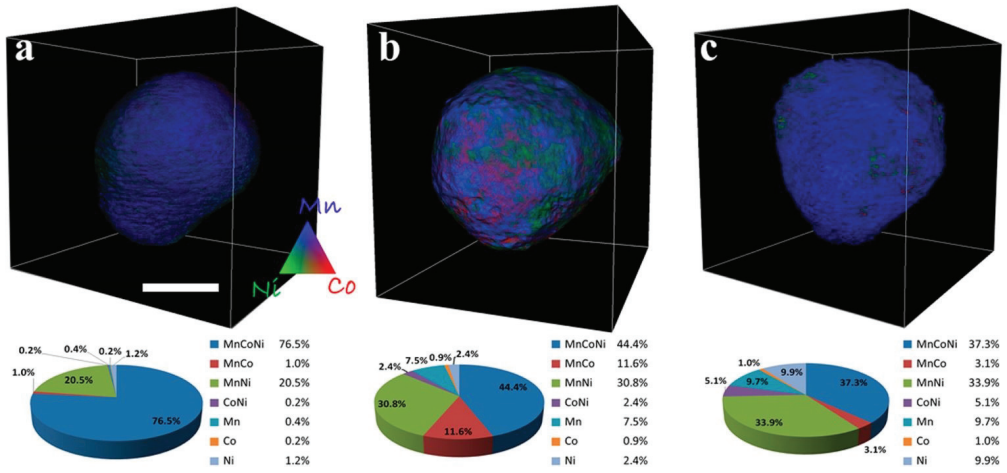

Figure 2.23: Elemental three-dimensional rendering of Mn, Ni and Co in a particles of $Li_{1.2}Mn_{0.525}Ni_{0.175}Co_{0.1}O_2$ in pristine state (a), after the first cycle (b) and after 200 cycles (c) between 2.5 V and 4.9 V at a rate of C/10. The scale bar shown in (a) is 5 μm. The pie charts show the relative concentrations of different elemental associations within each particle[195].

coexistence of phases at short length scales. Finally, the knowledge gained about the crystallographic directionality of the phase transitions can be used to design electrode particle morphologies which are less prone to cracking. Three dimensional chemical imaging (element sensitive tomography) is currently too time consuming (also giving rise to a high radiation dose) to use in *operando* experiments. The *ex situ* study by Yang *et al.*, however, illustrates the depth of information that can be obtained by this method [195]. They revealed significant changes in the Mn chemistry in individual particles of $Li_{1.2}Mn_{0.525}Ni_{0.175}Co_{0.1}O_2$ during cycling forming other compositions in the particle due to transition metal segregation. The changes observed were associated with the voltage fading (lowering) in this class of cathode materials with increasing cycling number. Dynamic XRD and total scattering computed tomography have a great potential to spatially resolve structural information of battery materials in three dimensions as demonstrated by Jensen *et al.* in an *ex situ* study of commercial cylindrical and coin cells of nickel metal hydride and lithium-ion batteries, respectively [198]. These

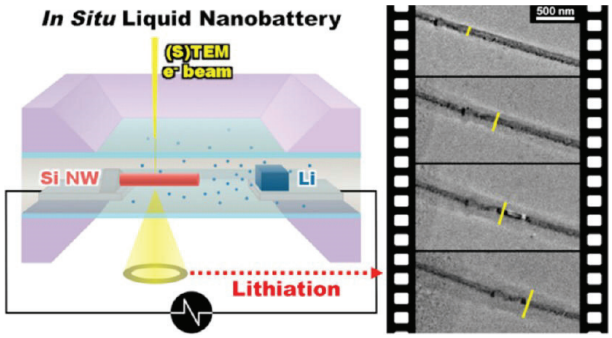

Figure 2.24: Schematic drawing showing the TEM liquid cell design which can be used to image individual Si nanowires during lithiation [204].

methods were first applied for *operando* investigations of catalyst systems [199, 200]. Coherent X-ray diffraction imaging can be used to map the local three dimensional strain evolution within a single particle during cycling as was demonstrated for $LiNi_{0.5}Mn_{1.5}O_4$ by Ulvestad *et al.* [201–203].

Other imaging techniques such as atomic force microscopy (AFM), scanning electron microscopy (SEM) and TEM spanning spatial resolutions from atomic to macroscopic distances can also be used to study morphological changes in batteries during operation [165, 166]. TEM is especially powerful since it in addition to morphology can reveal information about structural and chemical changes using electron diffraction and electron energy loss spectroscopy (EELS), respectively. On the other hand, the comparability to conventional battery configurations and testing methods is not as high as, for example, with X-ray based methods. An open cell configuration is often chosen for TEM analysis [205–208]. This configuration requires the use of electrolyte with low vapour pressure (solid or ionic electrolyte) which is in some cases only partly in contact with the electrode. Usually the electrode is emerged in organic electrolyte. Recent studies have, however, demonstrated a cell geometry where the electrode material is emerged in electrolyte (liquid cell) [204, 209]. Both open and liquid cells are used to image individual nanostructures. The small amount of active material implies that very low currents have to be used in the *operando* experiment. For this reason potentiostatic instead of the commonly used galvanostatic cycling

control is preferred. The liquid cells provide a more realistic cell configuration, while the open cell is easier to implement and allows for higher spatial resolution. Using the liquid cell it is possible to study electrolyte-electrode interfaces [204, 209] (see next paragraph), while *e.g.* anisotropic swelling of Si nanowires and migration of the 1 nm crystalline Si/amorphous Li_xSi interface [206] as well as size dependent cracking of the Si nanoparticles [207] were observed in the open cell.

Electrode voltages commonly exceed the stability range of organic electrolytes. Electrolyte reduction and oxidation will then occur at the interfaces between the electrolyte and the negative and positive electrodes, respectively. A stable passivation surface film the SEI containing organic as well as inorganic compounds may form and protect from further electrolyte reduction (Section 2.2.4). This may be accompanied by some gas evolution (*e.g.* ethylene, H_2, CO_2). Oxidative decomposition of the electrolyte, *e.g.* on overcharge, may cause considerable gas formation, presenting a safety hazard. *Operando* differential electrochemical mass spectrometry (DEMS), Fourier transform infrared spectroscopy (FTIR) and/or Raman spectroscopy can yield useful information on gas and surface film evolution [165, 173]. SEI formation on Si particles in LIB anodes was investigated using *ex situ* NMR revealing information about the local environment of H, Li, F and C in the organic and inorganic SEI species [210, 211]. Using *operando* soft X-ray microscopy element specific information on SEI species could be accessed using XAS. The elements that can be probed have to be heavier than C which means that no information can be obtained on H and Li. Na on the other hand can be probed using soft XAS. *Operando* TEM can be used to study interfacial phenomena in all solid state batteries (open cell) [212] and SEI formation in batteries using liquid electrolytes [204, 209]. As for the investigation of the working mechanisms using complementary structural characterization methods, a combination of techniques to study the morphological changes of electrode particles and the chemistry at the electrolyte-electrode interfaces will enable a deeper understanding of degradation mechanisms in batteries.

Chapter 3

X-ray Methods

The main experimental findings in this work were obtained using XRD and XAS. These techniques are introduced in this chapter.

3.1 X-ray powder diffraction

XRD is used to determine the atomic arrangement in a crystalline solid compound *i.e.* its crystal structure. The crystal structure is described by a periodically repeating unit cell containing one or more atoms in a three dimensional lattice. The lattice is defined by three non-planar basis vectors or six lattice parameters. The latter are the length of the unit cell edges (a,b,c) and the angles between them (α,β,γ). The positions of the atoms inside a unit cell are given by a set of atomic positions (x_i, y_i, z_i) measured from a selected lattice point. Each unit cell is filled by applying a set of symmetry operations to the set of atomic positions (the asymmetric unit). The set of symmetry operators is called the spacegroup (all the possible sets of operators for three dimensional symmetry are described by 230 spacegroups) and the unit cell represents the smallest unit with the full symmetry of the crystal structure. Full details concerning crystal structure description can be found in the *International Tables for Crystallography section A* [213].

X-rays are a form of electromagnetic radiation which interacts with the electrons surrounding atomic nuclei and their wavelength (λ) is in the order of interatomic distances in crystals. As a consequence X-rays which are

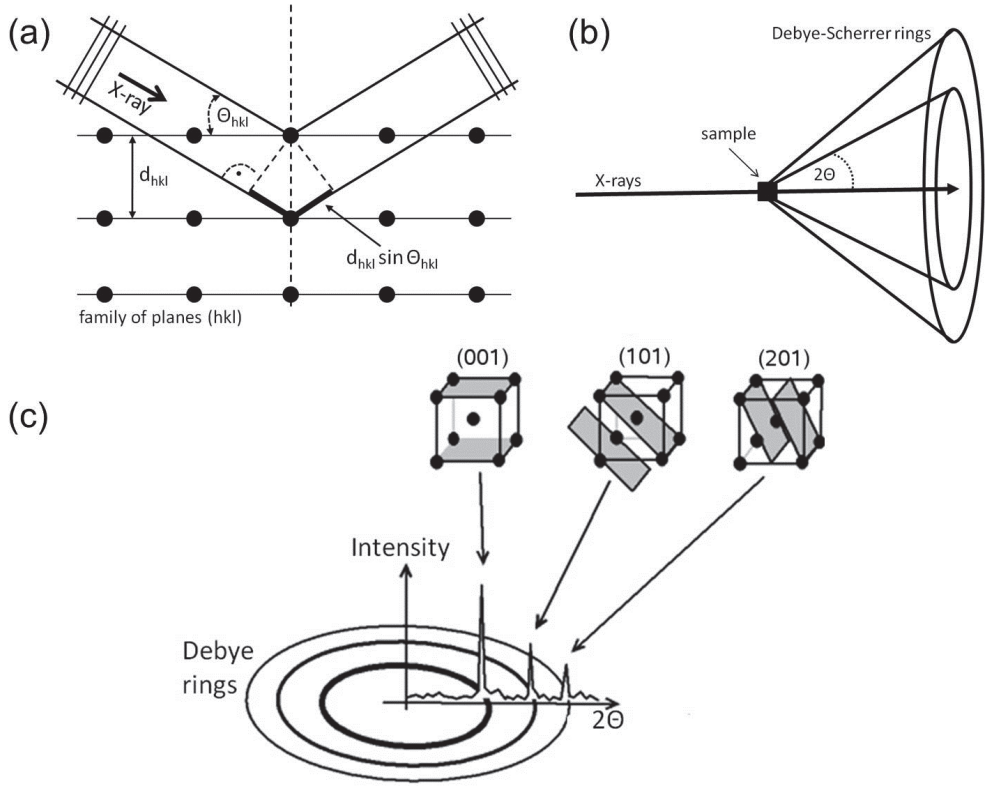

Figure 3.1: (a) Illustration of the geometry used for the derivation of the Bragg's law. (b) Scheme of the Debye-Scherrer geometry. (c) Relationship between $2D$ and conventional powder patterns. The Bragg reflections can be associated to the crystallographic planes $(h\,k\,l)$.

coherently scattered at the regularly arranged lattice planes can constructively interfere at certain well-defined angles. The condition for constructive interference is illustrated in Figure 3.1(a) and described by Bragg's law as

$$n\lambda = 2d_{hkl}\sin\theta_{hkl} \tag{3.1}$$

where n is an integer (normally 1) corresponding to the order of interference, d_{hkl} is the distance between parallel lattice planes with Miller indices $(h\,k\,l)$ (Miller indices describe the planes in terms of where they cut the unit cell axes, thus the $(h\,k\,l)$ plane cuts through the axes at $1/h.a$, $1/k.b$ and $1/l.c$, see

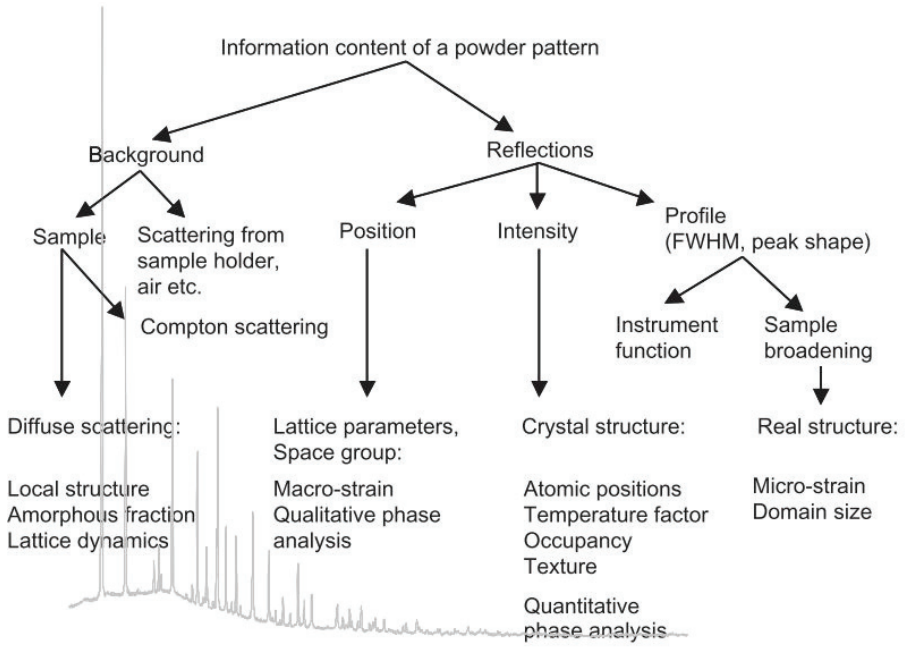

Figure 3.2: General information content of a powder pattern [214].

Figure 3.1) and θ_{hkl} the angle between the incident beam and these crystal planes. The angle of diffraction is defined as the angle between the incident and the diffracted beam which is equal to $2\theta_{hkl}$. When the sample is made of a large number of small randomly oriented crystallites (powder sample), the incident beam is scattered symmetrically in cones whose intersection with an area ($2D$) detector perpendicular to the incident beam gives rise to concentric rings called Debye-Scherrer rings (Figure 3.1(b)). The obtained $2D$ images of the Debye-Scherrer rings can be transformed into standard XRD powder diffraction patterns (scattered intensity *vs.* 2θ) by radial integration (Figure 3.1(c)). Alternatively the diffraction pattern can be obtained by scanning a point detector over a certain 2θ range.

The information contained in a powder diffraction pattern is summarized in Figure 3.2. The main information is extracted from a series of peaks (the Bragg reflections) which are characterized by their position, intensity and profile (shape). The peak positions and intensities can be used as a

fingerprint for the identification of unknown materials by comparing the diffraction pattern with patterns of a reference database. In depth analysis of the reflections can provide a quantitative description of crystal structures in terms of features such as bond lengths, bond angles and relative positions of atomic species in a unit cell as well as structural disorder. If several phases are present their relative fractions can be quantified.

The position of the reflections depends as expressed in Bragg's law (Equation 3.1) on the wavelength and the interplanar distances d_{hkl} *i.e.* the lattice. Certain Bragg reflections might, however, be extinct (systematic absences) due to destructive interference caused by the atomic arrangement. For these reflections the structure factor introduced in Equation 3.2 is zero. Extinction is a key tool in the determination of unit cell ("indexing") and spacegroup from diffraction data from the d-values. Uniform macroscopic strain changes the interplanar spacing giving rise to a shift in the average position of the diffraction peak. The intensity of a reflection for a randomly oriented powder is mainly determined by the magnitude of the structure factor, the amount of material and the absorption in the material. The structure factor is given as

$$F_{hkl} \;=\; \sum f_j(s)\; \mathrm{e}^{2\pi i(hx_j+ky_j+lz_j)}\; \mathrm{e}^{B_j s^2} \tag{3.2}$$

where $f_j(s)$ is the atomic scattering factor (form factor) of each atom j. Each atom has a characteristic scattering curve as a function of s ($= \sin\theta/\lambda$). The value of the scattering factor increases with the number of electrons of the atom and decreases with θ. The second term in the sum is determined by the set of atomic positions in the unit cell and its space group. It describes the occurrence and extinction of Bragg reflections. The last term accounts for thermal motion effects of the atoms in the crystal structure. The atoms oscillate about their equilibrium position which smears their scattering density. $B_j = 8\pi^2 < u_j^2 >$ designates the temperature factor (Debye-Waller factor) which accounts for the mean square displacement of atom j that is given by $< u_j^2 >$. In reality these factors are not the same in all directions (*i.e.* isotropic) but are better described by an ellipsoid (the anisotropic model). The intensity of a Bragg reflection is further influenced if the orientation of the crystallites is not completely random but preferentially oriented (textured) with respect to the incoming X-ray beam as a result of the crystal shape.

Preferential orientation can in most cases be avoided by appropriate sample preparation (*e.g.* the use of capillaries rather than flat sample holders). The peak shape is a convolution of instrumental and sample-related effects. If both diffractometer and sample were ideal the peak shape would be given by a simple Dirac peak profile (δ function). Instrumental effects will introduce peak profile broadening and asymmetry. The instrumental contribution to the peak shape can to a good approximation be estimated by measuring a well crystallized sample with homogeneous crystallite size larger than 3-5 μm and thus with negligible contribution to the peak shape [214]. This is commonly done using standard reference materials such as Si and LaB_6. Sample effects such as finite crystallite size (size effect) and microscopic strain (distortion) effects resulting from the defects in the crystal lattice will lead to a broadening of the peak profile. The profiles are broadened in inverse proportion to the crystal size. The relationship between the size of submicrometer crystallites and line broadening is described by the Scherrer equation as

$$\tau = \frac{K\lambda}{\beta \cos\theta_{hkl}} \tag{3.3}$$

where τ is the mean size of the crystalline domains which may be smaller or equal to the grain size, K is a dimensionless shape factor depending on the actual shape of the crystallite (0.89 for spherical shape) and β is the line broadening at half the maximum intensity (FWHM) after subtraction of the instrumental line broadening [215]. A crystallite shape independent description of the crystallite-size broadening was developed by Stokes and Wilson and can be stated as

$$\tau = \frac{\lambda}{\beta_i \cos\theta_{hkl}} \tag{3.4}$$

where β_i is the instrumentation corrected integral breadth (the width of a rectangle with the height of the peak and the same integral area as the peak) [215]. Non-uniform microscopic strain caused by defects such as dislocations, vacancies, interstitial or substitutional atoms gives rise to a distribution of d-spacings which broaden the peak profile. The strain (ε) is related to the

peak broadening due to strain (β_e) by [215]

$$\varepsilon = \frac{\beta_e}{4 \tan \theta} \tag{3.5}$$

Size and micro-strain effects may occur in preferred directions and generate anisotropic *hkl*-dependent peak broadening. The background of the diffraction pattern contains no Bragg reflections but only diffuse scattering from disordered (amorphous) materials showing no long-range order in the sample, the sample holder and air.

The information contained in the set of reflections and their features (position, intensity and profile) can be extracted using the Rietveld method [216]. This method calculates the entire powder diffraction pattern of a crystalline model including various experimental and sample dependent peak broadening effects. Parameters in the model such as phase composition, lattice parameters, macro-strain, atomic positions, temperature factors, size, micro-strain and experimental contributions that affect peak shape and background are varied, using a least-squares approach, until the difference between the calculated (Y_{calc}) and measured (Y_{obs}) intensities at each data point of the powder pattern are minimized according to the minimization function

$$M = \sum w \left(Y_{obs} - Y_{calc}\right)^2 \tag{3.6}$$

where w is a statistical weight related to the variance in Y_{obs}. The quality of the refinement is indicated by some residual functions. These include the plain pattern residual

$$R_p = \frac{\sum |Y_{obs} - Y_{calc}|}{\sum Y_{obs}} \tag{3.7}$$

which is often used in single crystal refinements; the weighted pattern residual

$$R_{wp} = \sqrt{\frac{M}{\sum w Y_{obs}^2}} \tag{3.8}$$

which is the only statistically relevant residual because it contains the minimization function M and is hence the most used residual in powder diffraction;

and the expected pattern residual

$$R_{exp} = \sqrt{\frac{N_{obs} - N_{var}}{\sum w Y_{obs}^2}} \tag{3.9}$$

where N_{obs} is the number of observations (data points) and N_{var} the number of refined variables and R_{exp} represents the smallest possible R_{wp} that can be reached. The denominator of the residual expressions contains the intensities of the powder pattern which means that the residual values (R-values) will always be low if the background is high. R_p and R_{wp} should therefore always be compared to R_{exp}. This can be done using the "goodness of fit" (GOF) also referred to as reduced χ^2

$$GOF = \chi^2 = \frac{R_{wp}}{R_{exp}} = \sqrt{\frac{M}{N_{obs} - N_{var}}} \tag{3.10}$$

which is also related to the minimization function M and will usually be greater than 1 if the weights (w) are correctly assigned. The least squares method might yield a local (false) minimum instead of a global minimum in M. It is therefore important to not only rely on the R-values but also to compare Y_{obs}, Y_{calc}, $Y_{obs} - Y_{calc}$ and background curves in a plot which might give hints on errors in the model. Another important indicator for problems in the refinement is the correlation matrix which states the degree of correlation between refined parameters.

The evolution of the XRD pattern can be followed *in situ* under variation of temperature, pressure, applied stress, electric or magnetic field, flow-gas compositions, or chemical composition *e.g.* in a battery. Many examples of XRD studies under non-ambient conditions using Rietveld methods to extract structural information exist [165, 214, 217–220]. More recently the parametric Rietveld approach, in which all powder diffraction patterns in a non-ambient series are refined in parallel, was introduced in [221].

In non-ambient *in situ* studies the use of X-rays produced by a synchrotron source coupled with fast $2D$ detectors is often preferred over home laboratory diffractometers. Synchrotron radiation has several advantages. It is extremely intense and highly collimated (*i.e.* it has a high brilliance)

which permits the design of instruments with very high angular resolution. Highly time-resolved measurements during chemical reactions *in situ* or after a perturbation are enabled by these properties in combination with modern $2D$ detectors requiring very short exposure and readout times. Synchrotron sources further provide a broad spectrum and the optimum wavelength for a particular experiment may be selected in the range 0.1 Å to 1 Å or more. At higher energies (*i.e.* short wavelength) the X-rays can penetrate deeper into absorbing samples. Varying the wavelength causes the angular position of the reflections to change. Thereby the number of measurable reflections within a given angular range and the separation between two neighbouring reflections are varied. If the wavelength is decreased more reflections can be measured at the expense of angular resolution. In a standard laboratory diffractometer the choice of wavelength is limited to the characteristic radiation emitted by a metal anode (*e.g.* Cu with $\lambda_{K_\alpha} \approx 1.54$ Å , Mo with $\lambda_{K_\alpha} \approx 0.71$ Å), the resolution and intensities are much lower and much longer counting times are required for a similar signal-to-noise ratio compared to synchrotron instruments, reducing the possible time resolution.

More details on the various aspects of powder diffraction introduced in this section can be found in [214].

3.2 X-ray absorption spectroscopy

XAS can be used to determine the oxidation state of a specific element in a compound and to study its local environment. An advantage of this method is that it can provide structural information such as bond lengths in amorphous materials and for species in solutions or gases.

The intense synchrotron X-ray radiation can be used to liberate electrons ("photoelectrons") from the low-energy bound states of the atoms in a compound. The incident X-ray photon transfers its kinetic energy to the photoelectron and is thus absorbed in the process. An X-ray absorption spectrum records the X-ray absorption (*i.e.* the absorption coefficient variation) as the energy of the incident X-ray photons is scanned across a range of energies at which the core electrons of an atom in a compound can be excited or ionized. Binding energies of core electrons in atoms range from 0.1 keV to 100 keV.

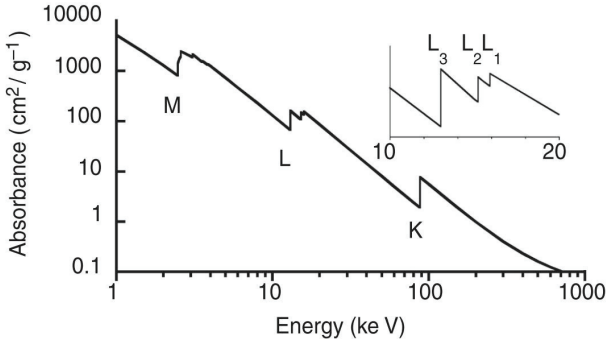

Figure 3.3: X-ray absorption spectrum of Pb. K-, L- and M-edges are observed. L- and M-edges are split as exemparily shown for the L-edge in the inset [222].

The absorption generally decreases as the X-ray photon energy increases, however, when the energy corresponds to the binding energies of different inner-shell electrons of the various elements present in the compound abrupt increases in absorption called "X-ray absorption edges" are observed. A typical low resolution X-ray absorption spectrum of Pb is shown in Figure 3.3. The absorption edges are labelled (K, L, M, *etc.*) according to the principal quantum number of the electrons ($n = 1, 2, 3, etc.$) that are excited. Excitation of a $1s$ electrons occurs at the K-edge, while excitation of $2s$ (L_1) and $2p$ (L_2 and L_3) electrons occurs at the L-edge. The $2p$ excitation is split into two edges because of spin-orbit coupling. Typical K-edge absorption spectra of Mn compounds are shown in Figure 3.4. Depending on the energy of the X-ray photons the X-ray absorption spectrum can be divided into two regions of interest as indicated in Figure 3.4(a). The XANES portion of the spectrum ($\sim$50 eV around the absorption edge) provides information about the valence state of the atom in a compound, its site symmetry and electronic structure. The EXAFS part ($\sim$50 eV to >600 eV above the absorption edge) provides information about the short range order in the vicinity of the absorbing atom in the compound in terms of type, number and distribution of neighbouring atoms.

The experimental setup for the XAS measurement is illustrated in Figure

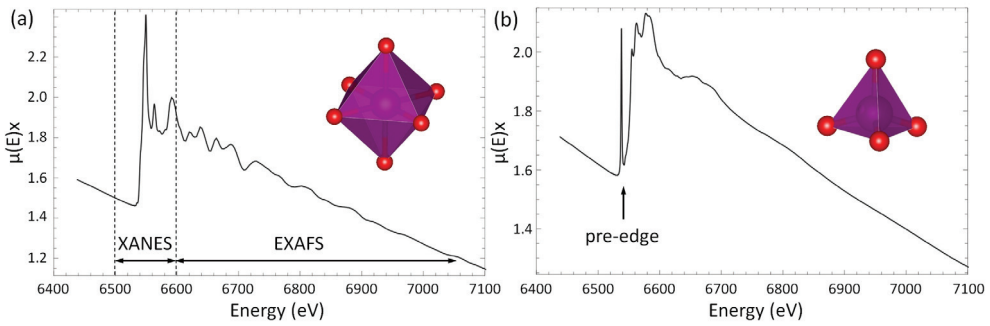

Figure 3.4: Typical K-edge X-ray absorption spectra of (a) MnO and (b) $KMnO_4$. The various characteristic regions for XANES and EXAFS as well as the pre-edge are indicated. Adapted from [223].

3.5. The energy

$$E = \frac{hc}{\lambda} \approx \frac{12.4\,\mathrm{keV/\AA}}{\lambda} \tag{3.11}$$

where $h = 4.14 \cdot 10^{-15}\,\mathrm{eV/s}$ is the Plank's constant and $c = 3 \cdot 10^{8}\,\mathrm{m/s}$ is the speed of light, is selected and varied by changing the angular orientation of a double-crystal monochromator according to Bragg's law (Equation 3.1). The second crystal is slightly offset (by $\Delta\theta$) from a perfect parallel alignment of the two monochromator crystals ("detuning") in order to reduce harmonic contamination ($n > 1$). The variation in absorption coefficient (μ) can be determined in a transmission experiment using ion chambers or in reflection geometry by measuring the variation in the intensity of a specific fluorescence line as the energy is moved over an absorption edge. The absorption is given as

$$A_t = \mu\, x = \ln\left(\frac{I_0}{I_1}\right) \qquad \text{or} \qquad A_r = \frac{I_F}{I_0} \tag{3.12}$$

where I_0 is the intensity of the incoming X-ray beam, I_1 is the intensity of the transmitted X-ray beam through a sample of thickness x and I_F is the intensity of a specific fluorescence line [222]. The use of the fluorescence detector is commonly preferred if the absorption due to the element of interest is much smaller than the background absorption (*e.g.* thin or dilute samples).

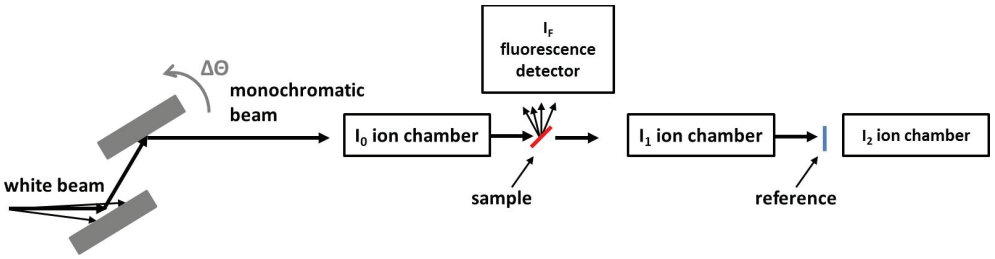

Figure 3.5: Typical experimental set-up for XAS measurements. Incident and transmitted intensities are commonly measured using ion chambers. An energy-dispersive detector can be used to measure X-ray fluorescence intensities for dilute samples.

XAS of a reference material containing the element of interest (*e.g.* a metal foil) is commonly measured simultaneously for energy calibration.

3.2.1 X-ray absorption near edge spectroscopy

In the near edge region (∼50 eV around the absorption edge) several weak transitions of core electrons to higher empty orbitals give rise to a pre-edge feature below the edge together with structured absorption on the high energy side of the edge (Figure 3.4). Above the edge the photoelectron has low kinetic energy giving it a long mean free path. This makes the XANES portion of the spectrum sensitive to longer distance absorber-scatterer interactions than the EXAFS part. These effects are reflected in the near-edge structure [222]. The absorption edge position is ill-defined in the literature. It is either taken as the energy at half-height of the edge step in the normalized spectrum or more commonly as the maximum of the first derivative with respect to energy. Unresolved transitions superimposed on the rising edge will further complicate the definition of a unique edge energy (Figure 3.4). Despite these challenges, the position of the absorption edge is useful in the determination of the oxidation state of the absorbing element in a compound. This is because the edge position increases in energy as the oxidation state of the absorbing atom increases [222]. In Figures 3.4(a) and 3.4(b) the relative shift in edge position can be compared by close inspection of the K-edge X-ray absorption spectra of MnO and $KMnO_4$ containing Mn^{2+} and Mn^{7+},

respectively. The near-edge structure, shaped by multiple scattering events of the low energy photoelectrons emitted from the absorber, can be used as a fingerprint of the compound and the absorbers coordination environment. The presence of a compound as well as its relative quantity in a mixture may be determined by spectral matching if a representative library of reference spectra is available. This can also be useful for quantitative determination of the valence state of the absorber. Calculation of XANES spectra is one of the outstanding current problems in the field and the library of references relies on experimental spectra [222].

The pre-edge structure can provide information on the energies of excited electronic states and can be used to distinguish between various coordination environments of the absorbant. Figure 3.4 compares the K-edge X-ray absorption spectra of MnO and $KMnO_4$. A negligible pre-edge is observed for Mn in octahedral coordination, while an intense pre-edge is found in the tetrahedral environment. For the first row transition metals with an open 3 d-shell the pre-edge region is associated with a weak 1 s – 3 d electric quadrupole transition. The intensity of the pre-edge is much larger for the tetrahedral and other coordinations less centrosymmetric than octahedral because of the p component in the d-p hybridized orbital. The pre-edge features in K-edge XANES for 4 d elements and L_1-edge for 5 d elements are analogous with those for the 3 d elements, but broadened due to the wider spacing of the core levels [224].

3.2.2 Extended X-ray absorption fine structure

In the EXAFS part of the X-ray absorption spectrum ($\sim$50 eV to >600 eV above the absorption edge) the ejected photoelectrons have significant energies and their wavelength are in the order of the interatomic distances. The outgoing photoelectron waves are backscattered by neighbouring atoms. Outgoing and backscattered waves may interfere constructively or destructively depending on their wavelength and the interatomic distances. The probability of absorption of an incoming X-ray photon will depend on the state of interference. Constructive interference results in a local maximum and destructive interference a local minimum in the EXAFS oscillations (Figure

3.4).

These modulations are analysed to reveal the nature (in terms of their electron density) and number of nearby atoms and the distance between the absorbing and scattering atoms.

The EXAFS data is analysed in terms of the normalized absorption coefficient

$$\chi = \frac{\mu - \mu_0}{\Delta\mu} \tag{3.13}$$

where μ is the experimentally measured absorption, μ_0 is a smooth background curve that is fit to the data to remove several extraneous contributions and $\Delta\mu$ is an estimate of the edge step. It is either expressed as a function of the energy (E) or the wave vector (k)

$$k = \sqrt{\frac{2m_e(E - E_0)}{h^2}} \tag{3.14}$$

where $m_e (= 9.11 \cdot 10^{-31}\,\mathrm{kg})$ is the electron rest mass and E_0 is the binding energy of the photoelectron. Figure 3.6 illustrates the structural information contained in the normalized absorption coefficient when plotted *vs.* k. $\chi(k)$ is commonly multiplied by k^3 (k^3-weighted) to enhance the oscillations at high k. The phase and the shape of the oscillations is determined by the energy dependence of the photoelectron scattering which depends on the identity of the scatterer. The frequency of the oscillations is inversely proportional to the absorber-scatterer distance and the amplitude of the oscillations is proportional to the number of scatterers.

The normalized oscillatory component of the absorption coefficient above the absorption edge can be estimated as

$$\chi(k) = \sum_{\mathrm{s}} \frac{N_s S_0^2 A_s(k)}{k R_{\mathrm{as}}^2} \exp\left(\frac{-2R_{\mathrm{as}}}{\lambda(k)}\right) \exp\left(-2\sigma_{\mathrm{as}}^2 k^2\right) \sin\left(2R_{\mathrm{as}}k + \phi_{\mathrm{as}}(k)\right) \tag{3.15}$$

with the summation taken over all scattering atoms [222]. N_s represents the number of scatterers (s) in a distance of R_{as} from the absorber (a). The distances might vary due to thermal displacements which are accounted for by the Debye-Waller factor ($\exp\left(-2\sigma_{\mathrm{as}}^2 k^2\right)$). The sinusoidal oscillations have a

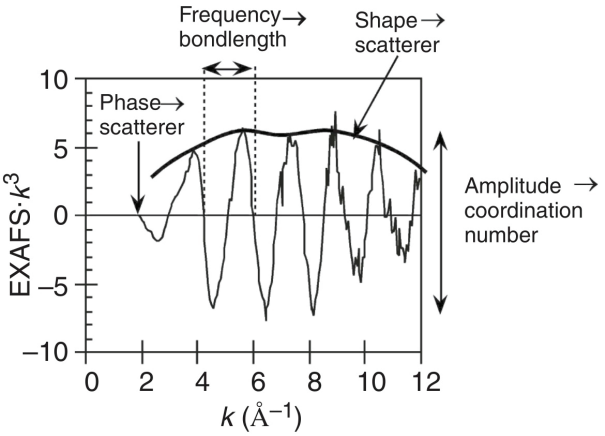

Figure 3.6: Illustration of structural information embedded in phase, shape, frequency and amplitude of k^3-weighted $\chi(k)$ [222].

frequency of $2R_{\mathrm{as}}$ which yields the average bond distances. $\phi_{\mathrm{as}}(k)$ is the phase shift that the photoelectron wave undergoes when passing through the potential of the absorber and scatterer. $A_s(k)$ describes the energy dependence of the photoelectron scattering. $A_s(k)$ and $\phi_{\mathrm{as}}(k)$ depend on the scatterer identity and are either fixed or determined. The amplitude is determined by $N_s S_0^2 A_s(k)$ where S_0^2 is a constant amplitude reduction factor and decays as $1/kR_{\mathrm{as}}^2$. The latter term shows that EXAFS is bound to be a local probe sensitive to a few Å around the absorber, due to the decline in itensity with R_{as}. The term $\exp(-2R_{\mathrm{as}}/\lambda(k))$ takes into account inelastic losses as the photoelectron propagates through the material.

The magnitude of the Fourier transformation of χ in reciprocal space (k in 1/Å) yields the radial structure function in real space (R in Å) as illustrated in Figure 3.7. The finite k range gives rise to ripples in the Fourier transform. The Fourier transformation is commonly not corrected for photoelectron phase shift ($\phi_{\mathrm{as}}(k)$) which results in a negative shift in the radial distance parameter (typically by about 0.5 Å). The radial structure function provides qualitative information about the distribution and interactions between the absorbing and coordinating atoms. Each peak corresponds to a particular coordination shell. The peak positions are related to the mean bond distances (if corrected for the phase shift). The amplitude of a peak

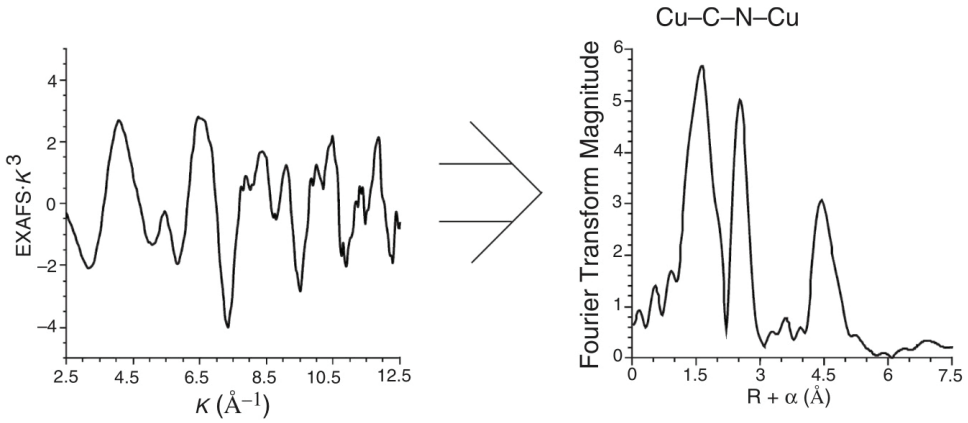

Figure 3.7: k^3-weighted $\chi(k)$ and its Fourier transform (radial structure function). The three distinct peaks in the radial structure function correspond to three absorber(Cu)-scatterer interactions as indicated. The Fourier transform was corrected for the photoelectron phase shift by addition of α to the radial distance R [222].

corresponds to type and number of atoms at that distance from the central scatterer, while the width of the peak describes the distribution (*e.g.* a distortion), of atoms in a particular coordination shell.

Chapter 4

Experimental

This chapter covers the experimental details which were most central to my work. Synthesis of active cathode materials, *ab initio* calculations (density functional theory (DFT)) and TEM were carried out by my co-workers and relevant experimental information is given in the research papers which can be found in the appendix.

4.1 Electrode preparation

4.1.1 Cathodes

PBAs, $Na_xMn[Fe(CN)_6]_y \cdot z\ H_2O$ ($x = 4y - 2$), also referred to as sodium manganese hexacyanoferrates, were prepared using the precipitation method described in `Paper II`. The materials were then dried at temperatures up to 120 °C in air or under vacuum for durations of up to 30 h. After drying the samples were stored under inert conditions to prevent rehydration.

Electrodes were prepared in a glove box (O_2 and H_2O levels <0.1 ppm, M. Braun) using fine polytetrafluoroethylene (PTFE) powder (Sigma Aldrich) as a binder. Usually 210 mg PBA were first mixed with 60 mg carbon black, Timcal Super P (C_{SP}) for 1 min in a Fritsch Mini-Mill Pulverisette 23 (P23) at 50 Hz with a ball-to-powder ratio of 13:1. Then 30 mg PTFE was added to the grinding bowl and the milling was continued for 1 min. This resulted in homogeneous electrode powder with a composition of 70 wt. % active

material, 20 wt. % C_{SP} and 10 wt. % PTFE. The electrode powder was then evenly distributed on a flat glass plate and roll pressed into a thin film with a mass loading of about 5 mg/cm^2. Thereby any exposure of the PBAs to moisture and solvent interaction during electrode preparation were avoided and no further drying was necessary. The water content of the PBAs was therefore not affected during electrode preparation.

Spinel-type $LiMn_{1.5}Ni_{0.5}O_4$ was prepared by the Pechini method. Materials synthesis and electrode preparation were carried out as described in [225] and `Paper V`. The mass loading of active material in the cathodes was about 3 mg/cm^2.

4.1.2 Anodes

Bi (99.999 %, Alfa Aesar), Bi_2S_3 (99 %, Sigma Aldrich), $Bi(VO_4)$ (99.9 %, Alfa Aesar) and $Bi_2(MoO_4)_3$ (99.9 %, Sigma Aldrich) were ground and mixed with C_{SP} by ball milling. The Bi-compound-to-carbon ratio was fixed at 7:3. Ball milling was conducted using a P23 at 50 Hz with a ball-to-powder ratio of 10:1 for 20 min (**Bi/C − 20 min**, **Bi_2S_3/C − 20 min**, **$Bi(VO_4)$/C − 20 min** and **$Bi_2(MoO_4)_3$/C − 20 min**) and a Fritsch Planetary Micro Mill Pulverisette 7 (P7) at 720 rpm with a ball-to-powder ratio of 20:1 for 24 h (**Bi/C − 24 h**, **$Bi(VO_4)$/C − 24 h** and **$Bi_2(MoO_4)_3$/C − 24 h**). Pure C_{SP} was also milled using the P7 at 720 rpm with a ball-to-powder ratio of 20:1 for 24 h (**a-C**). Grinding balls and bowls were made of steel. The samples were kept under inert conditions during and after milling to prevent oxidation.

The anode preparation was adapted from the method by Kayyar et al. [226]. 70 mg Bi-compound carbon composite, 10 mg C_{SP} and 20 mg PAA binder (Sigma Aldrich) or 80 mg **a-C** and 20 mg PAA were mixed in a 5 mL glass vial. Ethanol was added. The mixture was stirred with addition of a small glass ball in the closed vial using a vortex mixer at 3000 rpm for 2 h. The so obtained homogeneous slurry was coated on a metal foil (Al and Cu foils were used for Na and Li anodes, as appropriate) using a doctor-blade technique. Some anodes had to be prepared under inert conditions to prevent oxidation. For that purpose electrodes were prepared in a glove bag or glove box using dry and degassed ethanol. Drying of the electrodes was carried

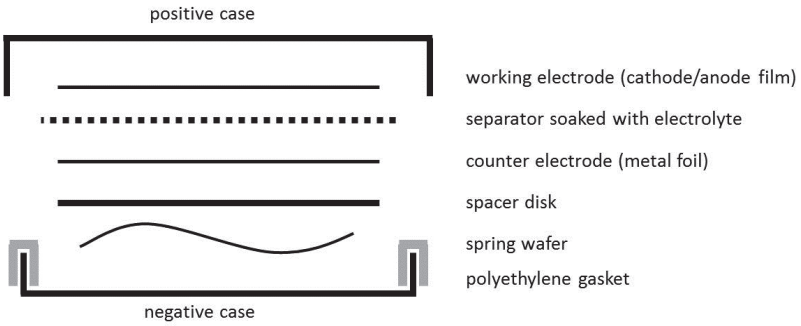

Figure 4.1: Schematic cross section of a 2032 coin cell.

out in air or under vacuum at 60 °C overnight. The electrode films were thereafter transferred to, and stored in the glove box where they were cut into disks. The mass loading of the active material in the anode was between 1 mg/cm^2 and 3 mg/cm^2.

4.2 Electrolyte

The sodium salts $NaPF_6$ (99 %, Alfa Aesar) and $NaClO_4$ (98 %, Sigma Aldrich) were dried at room temperature under vacuum until the pressure dropped below $1 \cdot 10^{-5}$ mbar. The organic carbonate solvents (Sigma Aldrich) EC and DEC were mixed in a 1 : 1 weight ratio in the glove box. 1 mmol sodium salt was added per mL solvent. The mixture was stirred until all salt had dissolved and then left to age overnight. Small amounts of the salts precipitated. The clear solution was decanted. The so obtained sodium electrolyte solution was split in two and 5 wt. % FEC were added to one portion. This resulted in a 1 M electrolyte solution of $NaPF_6$ or $NaClO_4$ in EC / DEC with or without addition of 5 wt. % FEC.

For the LIBs commercial electrolyte solution (Merck) containing 1 M $LiPF_6$ in EC / DMC (1 : 1 in weight) was used.

4.3 Electrochemical characterization

The batteries were assembled in the glove box. The working electrode (cathode or anode film) was separated from the Na or Li metal disk as counter electrode by electrolyte soaked glass fibers (GF/C, Whatman). The stack of components is pressed together for good electrical and ionic contact using a spring wafer and a spacer disc as exemplary represented for a coin cell (2032) in Figure 4.1. Hermetic sealing of the coin cell is guaranteed by applying high pressure on the polyethylene (PE) gasket and the inelastic metal casing.

Galvanostatic cycling and cyclic voltammetry (CV) experiments were performed using a Bat-Small battery cycler (Astrol). The cells were cycled at room temperature using a voltage window of 2 V to 4.2 V (*vs.* Na/Na^+) for the PBA, 3 V to 4.9 V (*vs.* Li/Li^+) for $LiMn_{1.5}Ni_{0.5}O_4$ and 10 mV to 2 V (*vs.* Na/Na^+) for the Na anodes. Specific capacity and current values are expressed on the basis of the mass of the active material. The $\mathrm{d}Q/\mathrm{d}V$ plots were prepared by taking the first derivative of the capacity (Q) *vs.* voltage (V). The average operation voltages were calculated by taking the average of all voltage values recorded in constant time intervals during charge/discharge steps. From these values average operation voltages for the complete cycles and voltage hysteresis could be determined.

4.4 X-ray diffraction

XRD profiles of the pristine or *ex situ* samples were collected on a Bruker D8 with Ge (1 1 1) Johanssen monochromator and Lynxeye detector with Cu K_{α_1} radiation in transmission geometry. High resolution XRD profiles of some pristine samples were collected at ID22, at the European Synchrotron (ESRF), using a 9 analyzer crystals detector. The wavelength ($\lambda = 0.42749$ Å) was calibrated by means of a Si NIST standard. For that purpose samples were sealed under Ar (if required) in 0.5 mm diameter thin-walled glass capillaries (Hilgenberg GmbH). *Ex situ* samples of electrodes cycled to a certain state of charge/discharge (voltage, cycle number) were prepared by disassembling the cell in the glove box and recovering the electrode powders from the electrode film.

Unknown phases were identified using the XRD pattern phase search-match-algorithm provided by EVA V3/V4, Bruker AXS based on phases reported in the PDF (ICDD) and COD crystallographic databases [227]. All profile fittings and Rietveld refinements were performed using TOPAS V4.2/V5, Bruker AXS (TOPAS). For each powder pattern zero-shift, background (Chebychev polynomial 8-13 terms), unit cell parameters, peak profile parameters for the individual phases, as well as their scale factor, were refined. Broad background features due to amorphous material (glass, carbon black, binder *etc.*) were fitted with broad peaks with refined position, Gaussian broadening and intensity. Crystallite sizes were determined using the integral breadth (L_{vol}-IB) method.

4.5 X-ray absorption spectroscopy

XAS was performed at beamline BM01B, of the Swiss-Norwegian Beam Lines (SNBL), at the ESRF. Mn K-edge (from 6460 eV to 6750 eV), Fe K-edge (from 7050 eV to 7280 eV), Ni K-edge (from 8230 eV to 8500 eV), Bi L_3-edge (from 13390 eV to 13540 eV) and Mo K-edge (from 19945 eV to 20140 eV) XANES and Ni K-edge (from 8180 eV to 9300 eV) EXAFS were collected in transmission mode using a Si (1 1 1) channel-cut type monochromator. The second crystal was detuned at about 65 % to reduce higher harmonics. The energy window of Mn K- and Fe K-edge XANES, and Bi L_3- and Mo K-edge XANES, allowed for parallel measurement of both edges using the same gas filling of the ion chambers. The XANES data were analysed using ATHENA [228] for absorption edge determination and spectrum normalization to an edge jump of unity. The absorption edge position was determined as the maximum of the first derivative of the spectrum. Mn (K-edge at 6539 eV), Fe (K-edge at 7112 eV), Ni (K-edge at 8333 eV), Ir (Ir L_1-edge coincidences with Bi L_3-edge, 13419 eV) and a Mo (K-edge at 20000 eV) foils were used as references.

4.6 *Operando* characterization

Combined *operando* XRD and XAS experiments were performed at beamline BM01B, of the SNBL, at the ESRF. *Operando* XRD experiments were also performed in house. The electrochemical cell design and the set-up at BM01B as well as in the home lab (Norwegian National Resource Centre for X-ray Diffraction and Scattering (RECX)) are presented in detail in `Paper I`. The *operando* cells were assembled in a similar manner to the coin cells in Section 4.3. It is important to prepare electrodes with sufficient mass loading in order to get sufficient contribution from the active material to the signal. The batteries were usually cycled at $C/10$ which means that a discharge/charge took about 10 h when each data point in the *operando* X-ray measurement took less than about 10 min (*i.e.* time resolution of $\sim$10 min).

All profile fittings and Rietveld refinements were performed using TOPAS. For each powder pattern zero-shift, background (Chebychev polynomial 8-13 terms), unit cell parameters, peak-profile parameters for the individual phases, as well as their scale factor, were refined. Broad background features due to amorphous material (glass fiber, carbon black, binder, Kapton *etc.*) were fitted with broad peaks with refined position, Gaussian broadening and intensity. Reflections from the textured Al foil were fitted for each individual powder pattern using a structureless phase with the lattice parameter and space group of Al metal ($a = 4.05$ Å, space group $Fm\bar{3}m$). Spot-like irregular reflections from the Li/Na metal were either masked or fitted with individual peaks (refining position, width and intensity) for the individual powder patterns. Each series of powder patterns was refined in parallel as a single dataset which allowed linking of certain refined parameters for the dataset (as in the parametric method of [221]). The most prominent examples of linked refined parameters are those accounting for the background. Another example is in electrochemical systems showing a series of two-phase reactions where cell and peak-profile parameters for the individual phases can often be assumed as constant and therefore refined to the same value for all powder patterns in the dataset.

Chapter 5

Summarising discussion

This chapter presents the key findings of this dissertation on the basis of the four main research papers (`Paper I` to `Paper IV`). It begins with a perspective on SIBs. Thereafter, the choice of SIB materials and the *operando* X-ray methods to study their working and degradation mechanisms will be motivated and the key findings of this dissertation will be summarised, discussed and viewed in a larger frame of reference. The chapter finishes with some concluding remarks and an outlook. Please note that Chapter 6 presents additional findings related to other aspects of non-aqueous rechargeable batteries, with respect to the metal ion system (Li instead of Na) and/or the methods used to study their working mechanisms, based on the supplementary research papers (`Paper V` and `Paper VI`). `Paper V` reports an *operando* synchrotron study of ordered and disordered high voltage spinel $LiMn_{1.5}Ni_{0.5}O_4$ for LIB cathodes and `Paper VI` presents a combined *ab initio* computational and experimental study of the Na and Li insertion mechanism into fully amorphous (glassy) carbon. Being related, but not central to the main findings of this dissertation on *operando* X-ray studies of SIB materials, with an emphasis on anode materials, the key findings of these supplementary research papers are not included here but are summarised, discussed and put into a broader context in a separate section. A list of the research papers and a statement of my contributions to these can be found in the front matter.

5.1 A perspective on sodium-ion batteries

The clean production, storage and transportation of energy are among the great challenges we face today. Electrochemical energy storage will certainly play an important role in the replacement of fossil fuels by intermittent renewable energy sources. In the short term LIBs show the greatest promise due to maturity and cost advantages over other currently available battery technologies. Large scale production of LIBs for EVs and stationary battery power stations gave rise to concerns over the availability of locally restricted Li resources and increasing prices. However, the cost of the Li precursors in a battery only makes up only 3 % of the cost at the cell level and it is rather the cost of the transition metal precursor in the cathode which dominates the cell cost (∼33 %) [44]. A recent study pointed out that the cell cost is not expected to increase by more than 10 % with increasing cost of the Li precursor [24]. The cost of the transition metal precursor (*e.g.* Co) on the other hand puts a fundamental limit on the cell cost [19] and it is questionable if LIB technology will be able to meet the cost requirements of large-scale stationary battery power stations. In this regard SIBs appear as a promising alternative because of the worldwide abundance of Na and similar properties to LIBs in many respects. The worldwide abundance of Na presents a geopolitical advantage of import independent production of SIBs using an alkaline ion precursor that can almost be considered free of cost. Although if analogous SIB and LIB electrode systems are compared the Na counterpart will commonly exhibit lower energy densities, differences in the Na and Li chemistries allow for a new degree of freedom in the choice of electrode materials. Here the discovery of the unique activity of the Fe^{3+}/Fe^{4+} redox-couple in SIB cathodes is significant. Fe is the most abundant transition metal in the Earth's crust which would allow for considerable cost reductions at the cell level. Another cost advantage due to differences in chemistries is given by the use of much cheaper Al foil instead of Cu foil as the anode current collector which may save about 8 % of the cell cost compared to a Li cell with the same energy density [44]. Similarities to LIB technology would enable the fast and cost efficient scale up of SIB production. Energy-cost comparisons stated that SIBs can only be cost competitive if the cost for the Li precursor

increases significantly (which seems unlikely according to the source mentioned above) or if the energy densities of SIBs can be increased significantly [19, 25]. In my view these energy-cost comparisons can be misleading, since only a few electrode systems were compared and none of these includes an Fe-based cathode which in my opinion will yield the greatest cost advantage. Certainly the energy densities of SIBs employing sustainable and low cost electrode materials need to be improved. This is especially true for the anode materials. Several high energy density Fe-based cathode systems (*e.g.* P2-$Na_{2/3}Mn_{1/2}Fe_{1/2}O_2$ [74], $Na_2Fe_2(SO_4)_3$ [29, 87], $Na_2MnFe(CN)_6$ [92]) were identified and are in competition regarding their cycling stability and rate performance. Hard carbon is currently the state of the art anode used in full cells [63]. It has, however, issues related to safety and rate performance. The greatest progress towards higher energy densities in SIBs can be expected in the field of high performance anodes. High energy densities and excellent rate performances can be obtained in alloying or conversion anode materials. The key points to be addressed in these classes of materials are the cycling stability, first cycle irreversible capacities and voltage hysteresis. The latter will affect the energy efficiency of the battery and may not be a primary concern for grid storage applications *e.g.* in the presence of negative electricity prices. Pronounced volume changes during cycling often associated with these materials may, however, pose a challenge for cell manufacture. If we could identify suitable electrode materials (especially anode materials) for SIBs with low cost per energy unit and achieve stable cycling behaviour in full cells (preferably for several thousands of cycles), SIB technology would, according to my understanding, outperform LIB technology for large-scale energy storage due to cost advantages. For portable applications and in the transport sector LIBs will remain the power source of choice due to their high energy densities and, therefore, light weight. Electrode system related cost advantages for LIBs due to higher energy densities could be achieved if the performance of Si anodes and/or Ni-rich and Li- and Mn-rich layered cathode materials can be improved, and/or if stable electrolytes for high operation voltage materials such as $LiMn_{1.5}Ni_{0.5}O_4$ (Section 6.1 and `Paper V`) can be identified. In the long term a breakthrough in other novel battery technologies such as metal-sulphur or metal-oxygen may change the picture

[19, 25].

5.2 *Operando* studies of electrode materials using X-ray diffraction and X-ray absorption spectroscopy

Understanding of the working and degradation mechanisms of electrode materials at the atomic scale is fundamental to the improvement of battery materials, especially in terms of cycling stability. The key to this is the investigation of these mechanisms under *operando* conditions. The electrochemical response of an electrode material during insertion, alloying or conversion reactions is intimately linked to its structural and electronic changes (Section 2.2.2) which can be studied using XRD and XAS (Chapter 3), respectively. The aim of this dissertation was therefore to develop an X-ray transparent electrochemical cell and a set-up that enables combined quasi-simultaneous *operando* XRD and XAS (*i.e.* XANES and EXAFS) characterization (`Paper I`). Using this instrumentation the goal was to investigate the structural evolutions, redox reactions and ageing processes during cycling of the batteries and to study the relationship between composition, structure, microstructure and electrochemical properties of a series of different compounds used as cathode and anode materials in SIBs. The compounds studied in this dissertation include the PBA $Na_{1.32}Mn[Fe(CN)_6]_{0.83} \cdot z\,H_2O$ as SIB cathode (`Paper II`) and Bi (`Paper III`), Bi_2S_3 (`Paper I`), $BiVO_4$ and $Bi_2(MoO_4)_3$ (`Paper IV`) as SIB anodes (and $LiMn_{1.5}Ni_{0.5}O_4$ as LIB cathode, `Paper V`). The choice of the materials, the material specific research questions we wanted to answer using *operando* X-ray characterization and our results will be elaborated and viewed in a broader context in later sections after introducing our *operando* instrumentation in the next section.

5.2.1 *Operando* electrochemical cell and set-up

The design of the X-ray transparent electrochemical cell for non-aqueous metal-ion batteries and the set-up (sample changer and interfacing software)

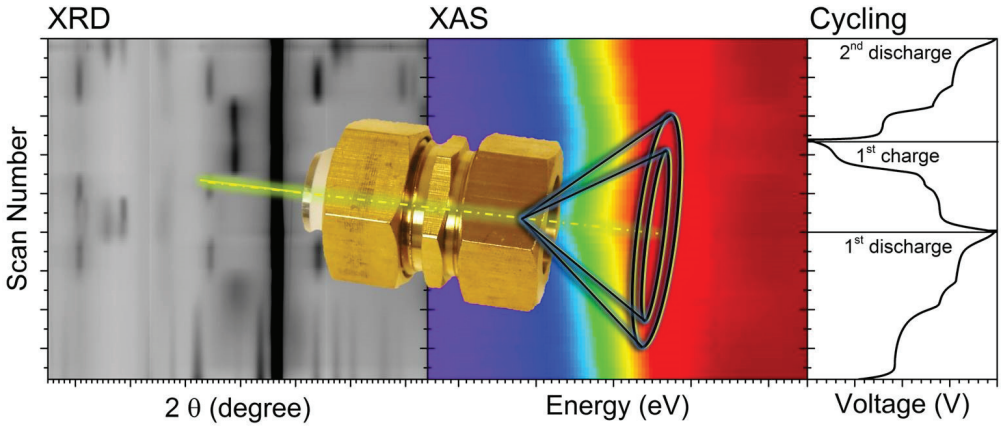

Figure 5.1: Illustration of the *operando* electrochemical cell for non-aqueous batteries and its use for combined XRD/XAS measurements coupled with electrochemical characterization [Abstract graphic of `Paper I`].

which enable *operando* X-ray characterization are described in `Paper I`. Figure 5.1 illustrates the electrochemical cell and its use for combined quasi-simultaneous *operando* XRD and XAS (such as XANES and EXAFS) measurements coupled with electrochemical characterization.

Prior to the design of the *operando* cell and set-up the advantages and disadvantages of existing cells and set-ups were accessed. An overview of reported cell designs and set-ups is presented in Table 5.1. The cell designs can be separated into disposable and reusable cells; they operate in transmission and/or reflection geometry; and employ Kapton (polyimide film), Sigradur-(G) (dense glassy carbon) or beryllium X-ray transparent windows. All are valid designs and set-ups which have been improved over the years. Our *operando* electrochemical cell and set-up were specifically designed for use at the SNBL at the ESRF. The instrumentation is supposed to be available to various user groups. Before the electrochemistry laboratory at the ESRF was established the cells had to be assembled in the home laboratory. We therefore chose to design a reusable cell which can be readily assembled/disassembled in a few steps using standard tools (Figure 5.2). The disposable cell designs are either based on pouch cells (also referred to as "coffee bag" cells) or modified coin cells. A good illustration of the pouch

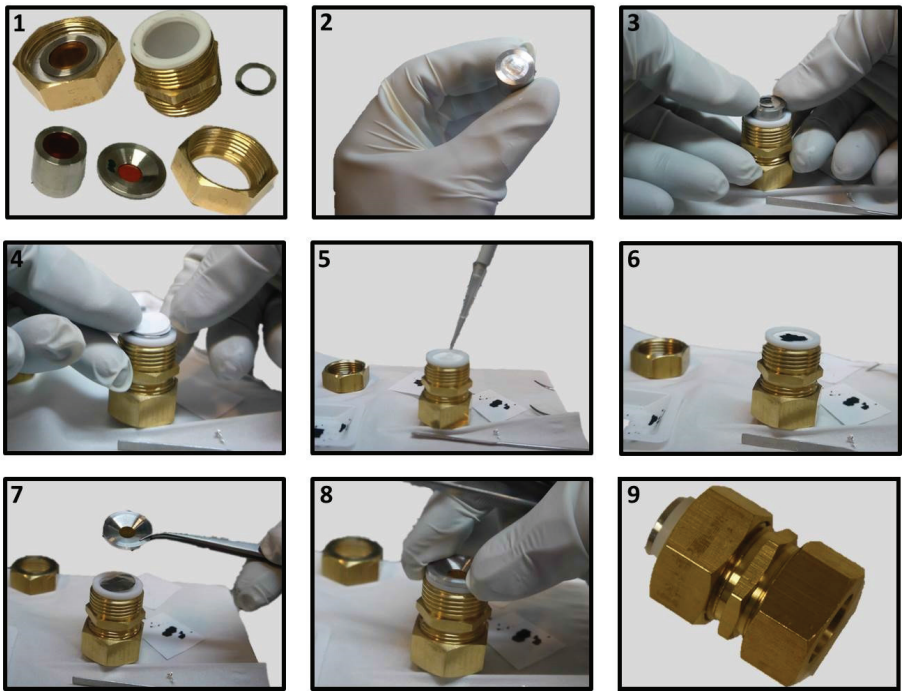

Figure 5.2: Assembly procedure: (1) Various parts of the cell are shown in the order of assembly; piston C, Teflon cylinder T, spring, piston B, battery as shown in (2)-(7); (2) Li/Na metal deposited on piston B; (3) piston B placed inside Teflon cylinder T on top of piston A and a spring; (4) glass fiber separator; (5) electrolyte; (6) self-standing electrode; (7) current collector metal foil (or electrode directly coated on metal foil); piston A; (9) closed cell [Figure S1 of `Paper I`].

cell design can be found in [229]. Preparation of the pouch cells and electrodes involves many steps. It further requires a special machine for sealing the pouches. Modified coin cells are commercially available and easy to assemble. They are, however, expansive and require a coin cell crimping tool or machine. Our cell is reusable and therefore free of charge after construction. It is, furthermore, made of a small number of standard components which are easily and cheaply manufactured. We tried to mimic a standard coin cell with respect to dimensions and applied pressure on the stack of battery components as well as electrolyte filling and void volume to avoid drying out of

Table 5.1: *Operando* electrochemical cell designs [Table 1 of `Paper I`]. For references please refer to `Paper I`.

Reference	Pouch cell	Coin cell	Swage-lock	Mode†	Source‡	XAS	Sample changer
This work, SNBL cell			×	T	S,H	×	12 cells
Herklotz *et al.* (2016)		×		T	S		8 cells
Bleith *et al.* (2015)			×	T	S	×	
Shen *et al.* (2014)			×	R	H		
Villevieille *et al.* (2014)	×			T,R	S,H	×	
Wilson *et al.* (2014)	×			R	H		
Brant *et al.* (2013)			×	T	S		
Herklotz *et al.* (2013)			×	T	S		4 cells
Borkiewicz *et al.* (2012)			×	T	S	×	6 cells
Shui *et al.* (2012)			×(Be)	R	H		
Rhodes *et al.* (2011)		×		R	H		
Leriche *et al.* (2010)				T,R	S,H	×	
Shin *et al.* (2008)		×		T	S		
Rosciano *et al.* (2007)	×			T	S		32 cells
Baehtz *et al.* (2005)			×	T	S		
Nikolowski *et al.* (2005)			×	T	S		
Deb *et al.* (2004)			×	T		×	
Braun *et al.* (2003)			×(Be)	T	S	×	
Ronci (2000), Ronci *et al.* (2001)			×	R	S		
Farley (1999)			×	T	S	×	
Gérand *et al.* (1999)	×			T	H		
Asahina *et al.* (1997)		×		R	H		
McBreen *et al.* (1997)			×	T		×	
Richard (1997)		×(Be)		R	H		
Gustafsson *et al.* (1992)	×			T	H		
McBreen *et al.* (1987)			×	T		×	
Fleischmann *et al.* (1986)	×(Be)		×(Be)	R	H		
Dahn *et al.* (1982)			×(Be)	R	H		

† T for transmission mode, R for reflection configuration. ‡ S for synchrotron and H for home laboratory X-ray source.

the electrolyte. For this purpose we integrated the spring wafer used in coin cells in our design. Other reusable designs either use no spring (*e.g.* [178]) or a spring with several coils which often gives rise to large void volumes (*e.g.* [230]). Our windows are large (8 mm in diameter) and have a wide

opening angle which allows for total scattering and X-ray measurements in both transmission and reflection geometry.

Our cell and the set-up were, as mentioned earlier, specifically designed for use at the SNBL but can in principle be implemented at any synchrotron beamline. The cells can also be used on home laboratory diffractometers with sufficient X-ray energy and intensity, as we demonstrate in `Paper I`. The cell was commissioned with windows made of sufficiently thick Kapton foil to avoid deformation of the foil when pressure is applied. In principal, any of the available window materials can be used in our design. We, however, wanted to avoid the use of toxic beryllium windows.

As pointed out by Borkiewicz *et al.* [231] it might be advantageous to employ more rigid and electrically conducting windows to ensure a more homogeneous pressure on the cell stack. For this purpose we started to commission a cell which employs Sigradur-(G) dense glassy carbon windows. These will, however, give a higher background contribution compared to the Kapton windows as was reported by Herklotz *et al.* [232]. The cell design should further be equipped with the option to use a third electrode (serving as reference electrode) in order to simultaneously characterize structural changes in both cathode and anode materials in full cells. This is possible because the X-ray beam passes through the entire stack of battery components. The X-rays thereby probe the structural changes averaged over the exposed volume as a function of time/charge state. A three-electrode option is, for example, available in the pouch cell design reported by Villevielle *et al.* [229].

Although various cell designs currently exist, very few reports about sample changers and interfacing software which enable the efficient use of beamtime are found in the literature (Table 5.1). Our sample changer and the interfacing software that is used to automate the measurements are described in detail in `Paper I`. The sample changers reported in the literature can accommodate 4, 6, 8 and 32 cells, respectively. Our sample changer at the SNBL has space for 12 cells. This number was found to be sufficient given the limitations imposed by the duration of the X-ray measurements. During our beamtimes we have not yet measured more than 8 cells, cycled at C/10, in parallel. Further, given the ease of replacing a cell in the sample changer without having to interrupt running measurements a large overca-

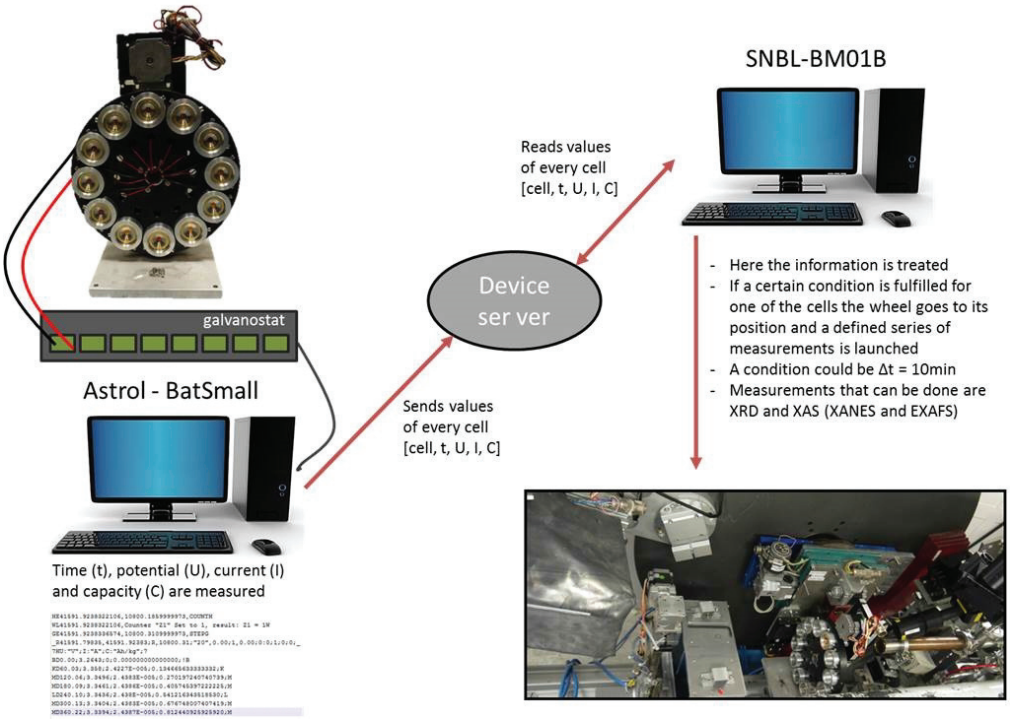

Figure 5.3: Schematic illustration of the interfacing software.

pacity of cells placed on hold in the sample changer can be avoided. How the replacement of cells in other sample changers is handled is not mentioned in the literature. For home laboratory XRD characterization no sample changer is required since XRD data collection using a position sensitive detector is relatively slow and only one cell can be measured at a time. However, if the diffractometer is equipped with an area detector and/or high intensity source the use of a sample changer may be worth considering. The interfacing software is schematically illustrated in Figure 5.3: The electrochemical measurements are controlled by a Bat-Small battery cycler (Astrol) which features easy programming and flexibility while running; A custom-made Python program fetches the current values (time, voltage, specific capacity) of each running measurement channel and sends them continuously (via a device server) to the computer from where the different X-ray measurements are coordinated; In an executable bash-like script the cell positions, the cor-

responding measurement sequence [XRD (two dimensional, one dimensional), XAS (XANES, EXAFS, at different edges)] and a condition for when a given cell should be measured are defined for each individual cell. A queuing system is implemented if the conditions are simultaneously fulfilled for several cells.

The functioning of our electrochemical cell for *operando* X-ray characterization of both LIBs and SIBs was demonstrated in `Paper I`. The hermeticity and chemical stability of our electrochemical cell for both LIBs and SIBs was proven by long term cycling experiments (up to 1 month). Similar cycling stability was achieved with other cell designs [229, 232]. The cells were found to operate stably in voltage ranges between 0.01 V and 4.9 V *vs.* Li/Li^+ in LIBs and 0.01 V and 4.2 V *vs.* Na/Na^+ in SIBs. Combined XRD, XANES and EXAFS analysis of an insertion LIB cathode material and a SIB conversion/alloying anode material are provided. These demonstrate well the level of insight into the working and degradation mechanisms of these electrode materials that can be gained using synchrotron and home laboratory X-ray sources. The cells, set-up and methods have further been essential for the findings reported in `Papers II`, `III`, `IV` and `V`. These material specific insights will be presented in the following sections (and in Section 6.1 for `Paper V`).

5.2.2 The PBA $Na_xMn[Fe(CN)_6]_y \cdot z\,H_2O$ as SIB insertion cathode

SIB cathode materials were introduced in Section 2.5.1. These include layered oxides, polyanionic frameworks and PBAs (hexacyanometalates). Their Fe-based variants show the greatest promise with respect to environmental aspects and cost. Among them the Fe-based PBAs, *i.e.* $Na_xMn[Fe(CN)_6]$ and $Na_xFe[Fe(CN)_6]$, appear as a promising class of high energy density, high rate, long cycle life and low cost SIB cathode materials. As reviewed in Section 2.5.1 many reports stress the importance of controlling the vacancy and water content of the PBA lattices to improve capacity utilization and cycling stability of these compounds. The reasons for the improved cycling stability are not fully understood.

For $Na_xMn[Fe(CN)_6]$ a higher energy density can be obtained compared to $Na_xFe[Fe(CN)_6]$ because of an about 0.3 V higher average operation voltage and similar theoretical capacities. Wang *et al.* [91] reported 134 mAh/g initial discharge capacity for a distorted PBA structure with composition $Na_{1.72}Mn[Fe(CN)_6]_{0.99} \cdot 2.3\,H_2O$. After 30 cycles 90 % of the initial discharge capacity was retained. For a non-distorted PBA cubic structure with composition $Na_{1.40}Mn[Fe(CN)_6]_{0.97} \cdot 3.3\,H_2O$ they observed lower initial discharge capacity (123 mAh/g) but improved capacity retention (96 % after 30 cycles). The capacity degradation was therefore ascribed to the expected phase transitions between distorted and cubic structure when Na is extracted from and inserted into the structure during cycling. Starting from non-distorted Mn hexacyanoferrate thin films Moritomo *et al.* observed different structural changes against Li content depending on the initial composition ($Na_xMn[Fe(CN)_6]_y$, where $y = 0.83$, 0.87 and 0.93) [233]. For $Na_{1.32}Mn[Fe(CN)_6]_{0.83} \cdot 3.5\,H_2O$ they report a single cubic phase with different lattice parameters for different Na contents. The discharge profiles of Na and Li analogues ($y = 0.83$) show different features (two well separated flat plateaus for Li and only slightly separated sloped plateaus for Na) and thus different sodiation and lithiation mechanisms might be expected. Indeed the voltage profile is intimately linked to the structural response of the electrode material during cycling (Section 2.2.2). The pronounced differences in the charge and discharge voltage profiles of $Na_xMn[Fe(CN)_6]$ reported by Wang *et al.* [91] may also indicate different desodiation and sodiation mechanisms.

Using *operando* quasi-simultaneous XRD/XANES we aimed to reveal the structural and electronic changes in $Na_{1.32}Mn[Fe(CN)_6]_{0.83} \cdot z\,H_2O$ during charge and discharge to find whether the desodiation and sodiation mechanisms of this material are different. Another aspect we wanted to investigate was the impact of varying structural modifications on the structural changes during cycling and their effect on the cycling stability. For this purpose we prepared distorted and non-distorted PBA structures similar to those observed by Wang *et al.* [91] by varying the water content ($z = 3.0$ and 2.2, sample I and II, respectively). We could thereby also study the influence of the different water content on the electrochemical performance.

Our findings are reported in detail in `Paper II`. Contrary to the previous

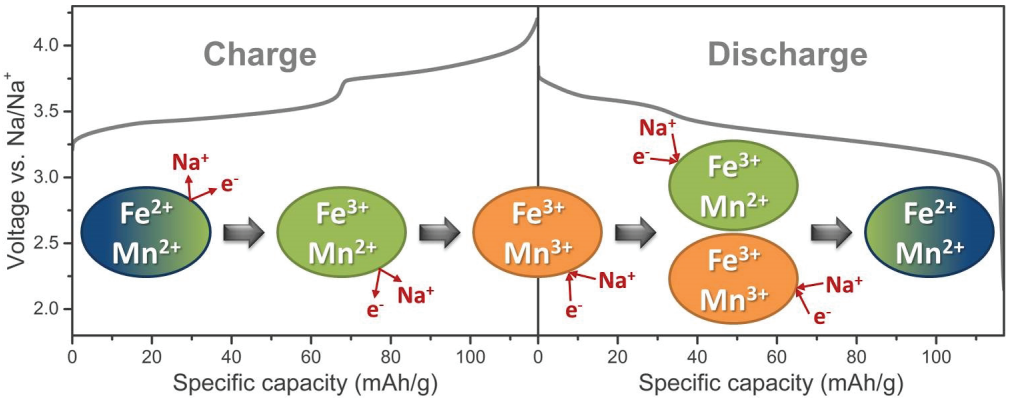

Figure 5.4: Illustration of the working mechanism of the PBA $Na_{1.32}Mn[Fe(CN)_6]_{0.83} \cdot z\,H_2O$. The different colours indicate different phases [Abstract graphic of `Paper II`].

findings of Moritomo *et al.* [233] we observed a series of reversible structural phase transitions that are clearly linked to the galvanostatic charge and discharge profiles in both samples. We found that different desodiation and sodiation mechanisms give rise to pronounced differences in the galvanostatic charge and discharge profiles. These are illustrated in Figure 5.4. Combining the knowledge gained from the *operando* synchrotron investigation with electrochemical cycling to different upper cut-off voltages and *ex situ* XRD characterization we were able to decouple possible factors giving rise to capacity degradation, such as structural changes (phase transitions and/or volume changes) and structural disintegration (transition metal dissolution and/or residual formation). The capacity degradation was not attributed to the monoclinic to cubic phase transition because of the identical cycling stability of both samples in the low voltage plateau (2 V to 3.6 V). The monoclinic to cubic phase transition takes place in this voltage range for for sample I but not for sample II. While the Fe^{2+}/Fe^{3+} redox reaction in the lower voltage plateau with a volume change of about 2 % is unproblematic, the relatively large volume changes of about 8 % between the sodiated and desodiated cubic phases (which are associated with Mn^{2+} and Mn^{3+}, respectively) in the higher voltage plateau may contribute to capacity degradation. In our samples the dominating capacity degradation mechanism was, how-

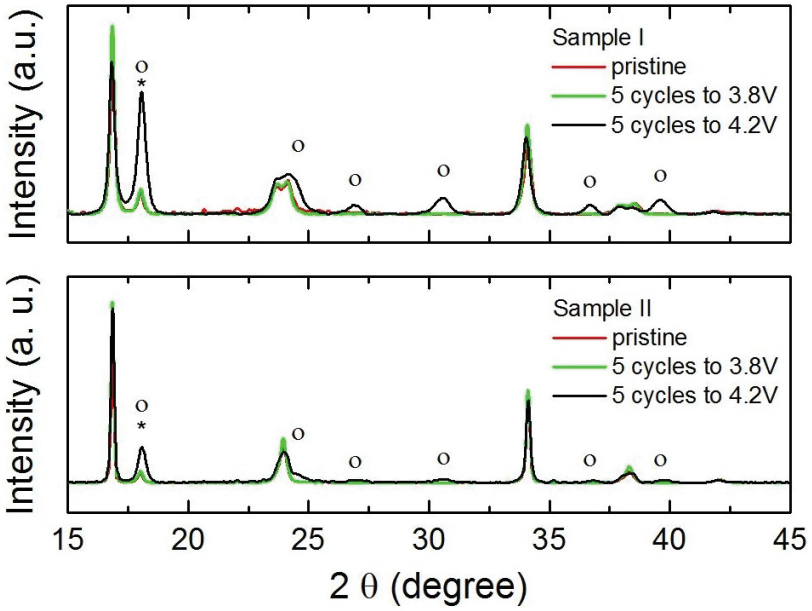

Figure 5.5: *Ex situ* XRD profiles of sample I and sample II cycled for 5 times between 2 V and 3.8 V or 4.2 V. The pristine material was loaded into a coin cell and left at open circuit voltage while the other cells were cycled. The symbols o and * mark peaks from $NaMnCl_3$ (PDF-number 01-070-1322) and the PTFE binder, respectively. Despite the loss of Mn from the PBA at high voltage no change in lattice parameters is observed [Figure S10 of `Paper II`].

ever, associated with irreversible side reactions taking place between 3.8 V and 4.2 V (Figure 5.5). With repeated cycling the active material loses Mn in the form of $NaMnCl_3$ (detected by *ex situ* XRD) accompanied by electrolyte decomposition which causes capacity degradation. Loss of capacity appears to be promoted by both coordinating water in $[Fe(CN)_6]$ vacancies and higher zeolitic water content in the pristine material. Thus, we showed why synthetic conditions influencing the amount of $[Fe(CN)_6]$ vacancies and water content are critical for the performance of PBAs in a battery. The mechanism of the residual phase formation remains to be understood.

In parallel to our efforts on the PBAs Song *et al.* [92] synthesized almost vacancy free $Na_{1.89}Mn[Fe(CN)_6]_{0.97} \cdot z\,H_2O$ with varying structural modifications. The structure was affected by the water content resulting in a mono-

clinic and rhombohedral phase for $z = 1.9$ and 0.3, respectively. The cubic phase was not observed in the pristine samples because of their high Na concentrations. The different water content in the structures influences the structural response during cycling which in turn influences the voltage profile. The monoclinic sample ($z = 1.9$) shows two voltage plateaus with a structural transformation from the monoclinic to a cubic phase in the lower voltage plateau and from the cubic to a tetragonal phase in the higher voltage plateau. In the main, this working mechanism is analogous to what we found for $Na_{1.32}Mn[Fe(CN)_6]_{0.83} \cdot 3.0\,H_2O$. Our findings, however, differ in three minor points: (1) Song *et al.* did not observe the two-phase behaviour of cubic and tetragonal phases in the higher voltage plateau because of an insufficient number of *ex situ* XRD measurements, showing the superiority of *operando* measurements; (2) We assigned a cubic rather than tetragonal phase to the fully desodiated sample. It is difficult to distinguish between these closely related phases especially if the resolution of the diffraction pattern is compromised by structural disorder due to $[Fe(CN)_6]$ vacancies and water in our samples and limited instrumental resolution. We therefore used the higher symmetry structural model (the simplest model which fitted the data), but the tetragonal distortion caused by Jahn-Teller activity of $Mn^{3+}N_6$ might be equally valid; (3) The removal of water during cycling which leads to the formation of the rhombohedral phase was not observed in our samples. Further characterization, *e.g.* neutron powder diffraction, would be necessary to verify electrochemical removal of water in our samples. The rhombohedral sample ($z = 0.3$) shows a single flat voltage plateau in which the rhombohedral phase is transformed into the desodiated tetragonal phase, showing two-phase behaviour upon Na removal. $Na_{1.89}Mn[Fe(CN)_6]_{0.97} \cdot 0.3\,H_2O$ further exhibits an initial discharge capacity of 150 mAh/g at an average operation voltage of 3.5 V, retains 75 % of its capacity over 500 cycles and shows excellent rate capabilities (*e.g.* 120 mAh/g are retained at 20C). The almost $[Fe(CN)_6]$ vacancy and water free sample reported by Song *et al.* [92] is currently one of the most promising materials for SIB cathodes with respect to energy density, cycling stability and cost.

5.2.3 Bismuth based sodium alloying/conversion anodes

The current options for suitable SIBs anode materials are limited because most known materials suffer from insufficient cycling stability and/or low energy density (Section 2.5.2). Hard carbons were found to possess suitable properties for use in SIBs and are considered to be the anode material of choice for the first generation of SIBs. However, relatively low gravimetric and volumetric capacities limit their energy densities and low voltage operation raises concerns about Na metal deposition (plating) which is associated with safety hazards.

Alloying anodes are an important class of anode materials because they allow each anode atom to combine with several charge carriers, yielding high volumetric and gravimetric capacities. Despite the fact that improved performance has been observed for alloying anode materials made of nanoparticles (Section 2.5.2), the reasons for the improvement are not fully understood.

Among the alloying anode materials for SIBs, Bi is one of the least studied materials. This might be due to its lower theoretical gravimetric capacity (385 mAh/g) compared to other alloying anode materials (Section 2.5.2). Its volumetric capacity (1075 mAh/cm^3) is, however, comparable to those of Sn and Sb and its associated volume change of 250 % is lower compared to 430 % and 290 % for Sn and Sb, respectively. Bi is furthermore an interesting alloying anode material since it has unusually low toxicity for a heavy metal. Bi is for instance used in medicines and cosmetics.

Lithiation and sodiation mechanisms for Bi have been reported. The lithiation of Bi follows sequential formation of LiBi and Li_3Bi according to the Li – Bi equilibrium phase diagram which is fully reversible upon delithiation [129]. Reports on the sodiation mechanism for Bi are inconsistent. Ellis *et al.* reported that the sodiation and desodiation mechanisms reversibly follow the Na – Bi equilibrium phase diagram with the formation of NaBi and Na_3Bi [127]. Su *et al.* suggested Na intercalation in between Bi layers along the *c*-axis [128].

Using our *operando* X-ray characterization tools we wanted to clarify the sodiation mechanism of Bi and investigate how it is affected by the Bi microstructure (micro- *vs.* nanocrystalline material). We further wished to

study the degradation mechanism in microcrystalline Bi and understand why the nanocrystallites show improved cycling stability.

Our findings are presented in detail in `Paper III`. We found that the sodiation of Bi follows different reaction paths depending on the Bi crystallite size as shown in Figure 5.6.

Our results on the reaction path of the microcrystalline Bi (Figure 5.6(a)) reversibly following the Na–Bi equilibrium phase diagram are in good agreement with the *in situ* study by Ellis *et al.* [127]. The Na intercalation mechanism in between Bi layers stacked along the *c*-axis with negligible lattice changes as suggested by Su *et al.* [128] based on *ex situ* XRD data was not observed for either microstructure. From the experimental details in [128] it is not clear whether the *ex situ* XRD samples were prepared and measured under inert conditions or in air. When exposed to air Na–Bi alloys decompose to Bi and Na_2O. It might hence be that the minor variations in the Bi crystal structure are due to sample decomposition prior to the XRD measurement which gave rise to a misleading interpretation of the results. As pointed out in Section 2.6 these and other problems can be avoided by *operando* studies.

Our findings furthermore clearly show how in a nanocrystalline Bi anode the final Na_3Bi phase has a cubic structure (Figure 5.6(b)), while for an anode containing microcrystalline Bi, hexagonal Na_3Bi is formed. In both cases NaBi was found as an intermediate phase between the fully desodiated and sodiated forms. The working mechanisms for micro- and nanocrystalline Bi are illustrated in Figure 5.7. Comparison of the structures rationalizes why this leads to improved cycling stability: the conversion path between NaBi and the cubic form requires fewer and smaller structural changes. Capacity degradation in the microcrystalline anode was associated with particle pulverization and loss of active material in form of inactive residual phases as evidenced by *ex situ* XRD.

`Paper III` shows that crystallite size effects can influence the performance of battery materials by making the structural chemistry deviate from what is predicted by the equilibrium phase diagram. Using crystallite size to direct the structural chemistry we may thus be able to improve the lifetime of high capacity batteries effectively and at low cost.

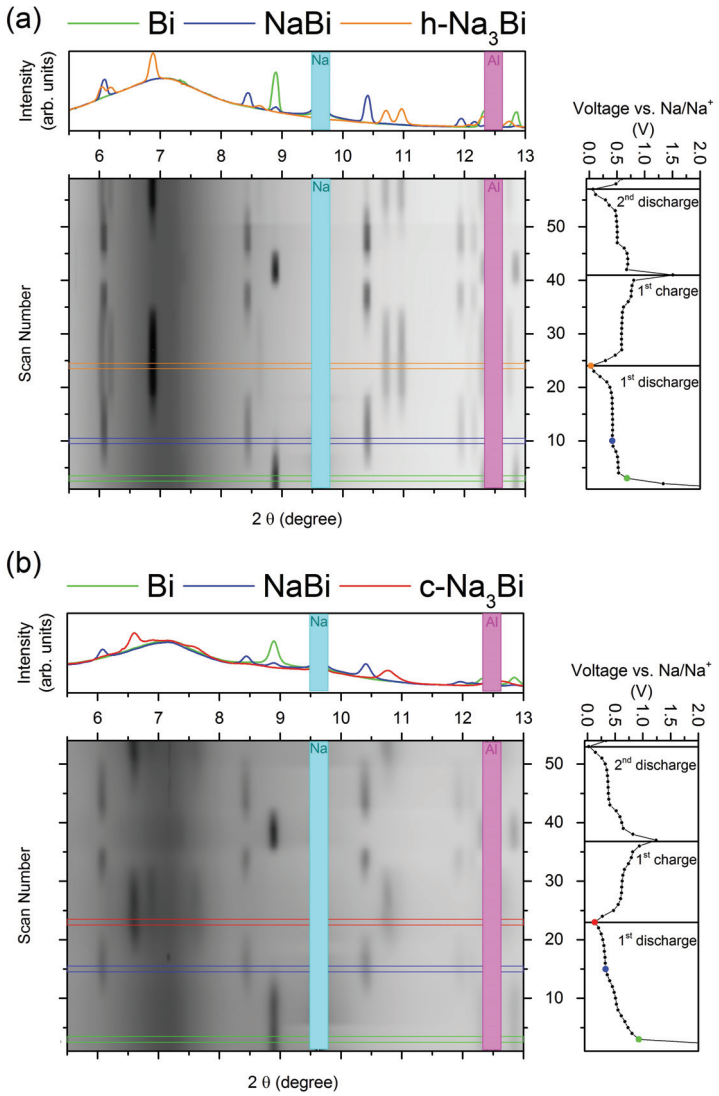

Figure 5.6: Film plots of *operando* diffraction profiles (λ =0.50648 Å) compared with the voltage profile of (a) microcrystalline and (b) nanocrystalline Bi. The diffraction profiles of selected phases are shown in the top panel. Bragg reflections from Na and Al are covered in cyan and magenta, respectively.

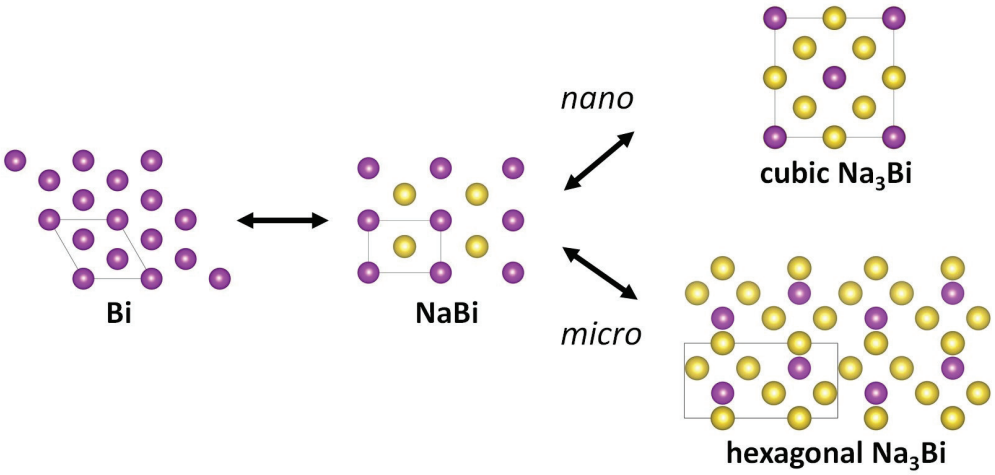

Figure 5.7: Illustration of the different reaction path during sodiation of Bi depending on its crystallite size [Abstract graphic of `Paper III`].

The working mechanism of microcrystalline Sb with Na, unlike the Li–Sb system, interestingly does not proceed via the formation of Na–Sb phases predicted by the equilibrium phase diagram. Instead the formation of several amorphous intermediate phases is observed [123, 125]. Compared to the Li–Sb system more stable cycling behaviour was observed and was attributed to reduced anisotropic mechanical stress during cycling due to the amorphous nature of the intermediate phases. In our study of the Na–Bi system we did not observe the formation of intermediate amorphous phases. Although small fractions of amorphous materials are usually neglected in XRD analysis, XAS can be used to study crystalline as well as amorphous materials. Combining XRD and XANES analysis we can exclude the coexistence of crystalline and amorphous Na–Bi phases since the trends in Na content per Bi determined from XRD analysis and in the relative Bi L_3 edge shift are in excellent agreement. Otherwise one would observe a mismatch, as for the initially present Bi_2O_3 which was not taken into account in the XRD analysis. In analogy with our findings for the microcrystalline Bi, the presence of a cubic Na_3Sb minority phase was also revealed during cycling of microcrystalline Sb. It would therefore be worth investigating the structural response of nanocrystalline Sb during cycling against Na to answer whether

nanocrystalline Sb, like nanocrystalline Bi, mainly forms cubic Na_3Sb and in how far the reaction path deviates from the one observed for the microcrystalline material. Pronounced differences in the electrochemical response (*i.e.* the differential capacity plots) of micro- and nanocrystalline materials support the presence of different working mechanisms [122, 123].

Working with the preparation and testing of Bi/C-composite electrodes we discovered that **Bi/C − 24 h** oxidises in air. The Bi/C-composite electrodes had to be prepared under inert conditions because the formed Bi_2O_3 gave rise to surplus capacity owing to a reversible conversion reaction (in addition to contributions from carbon to the reversible capacity as pointed out in the discussion of `Paper VI` in Section 6.2). Based on this observation we initiated a systematic investigation of Bi-based conversion reactions based on Bi_2O_3, Bi_2S_3, $BiCl_3$, $BiBr_3$ and BiI_3. Reversible conversion reactions, although with limited cycling stability, were found for Bi_2O_3 and Bi_2S_3, but not for $BiCl_3$, $BiBr_3$ and BiI_3. Other groups have reported on the reversible conversion reaction based on Bi_2O_3 and Bi_2S_3 in SIBs [43, 158, 159].

For Bi_2S_3 we investigated the electrochemical working and degradation mechanisms using home laboratory *operando* XRD and advanced Rietveld analysis, which were reported in `Paper I`. The working mechanism was found to involve many nanocrystalline phases which are difficult to detect and quantify using common XRD analysis. In our characterization we took advantage of the high number of powder patterns (*i.e.* 250) which we refined in parallel as a single dataset. This allowed us to link certain refined parameters for all powder patterns in the dataset. Under the assumption that the lattice parameters in the series of two-phase conversion/alloying reactions do not evolve significantly and that the change in the background is due to changes in the phase fractions of nanocrystalline phases, we refined lattice parameters for the individual phases to the same value for all 250 powder patterns and used the same background function for the entire dataset. The presence of the involved phases was verified by analysis of the summed intensities of all powder patterns collected during the first sodiation and desodiation, respectively. This advanced Rietveld analysis allowed us to track the evolution of phase fractions including nanocrystalline phases (Figure 5.8) and their average crystallite sizes. The working mechanism we

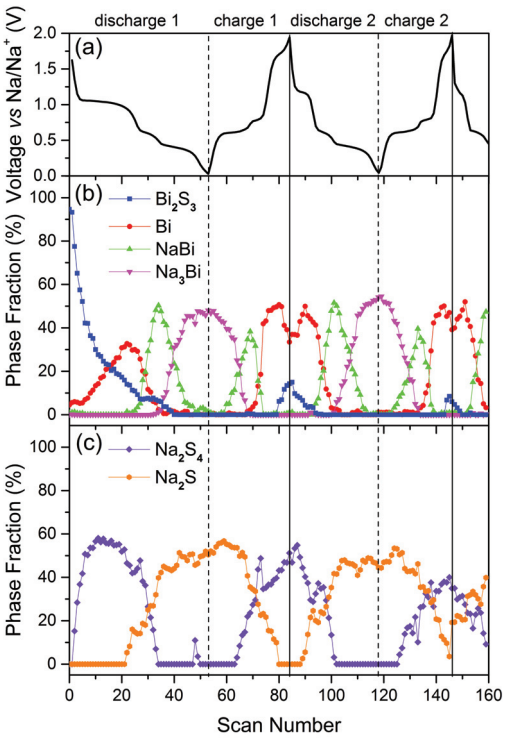

Figure 5.8: (a) Voltage profile of Bi_2S_3 compared to the phase fractions of (b) Bi_2S_3, Bi, NaBi and Na_3Bi, and (c) Na_2S_4 and Na_2S [Figure 7 of `Paper I`].

reported for Bi_2S_3 in `Paper I` is in conflict with the working mechanisms suggested by Sun *et al.* [159] and Li *et al.* [43]. Their *ex situ* analysis has similar issues as the one for the Na–Bi system discussed above.

We found that Bi nanocrystallites are formed during the initial conversion of Bi_2S_3 (Figure 5.9). The nanocrystallites could thus, with respect to our findings in `Paper III`, give rise to better cycling performance of the electrochemical alloying reaction with Na. However, capacity degradation was observed and was associated with Bi particle agglomeration during further cycling leading to a reduction of the active surface area which is necessary for a reversible conversion reaction. One might argue that capacity degradation is observed because the reversible conversion reaction of Bi_2S_3 is partially hindered by the use of too low an upper voltage limit (2 V) in our study com-

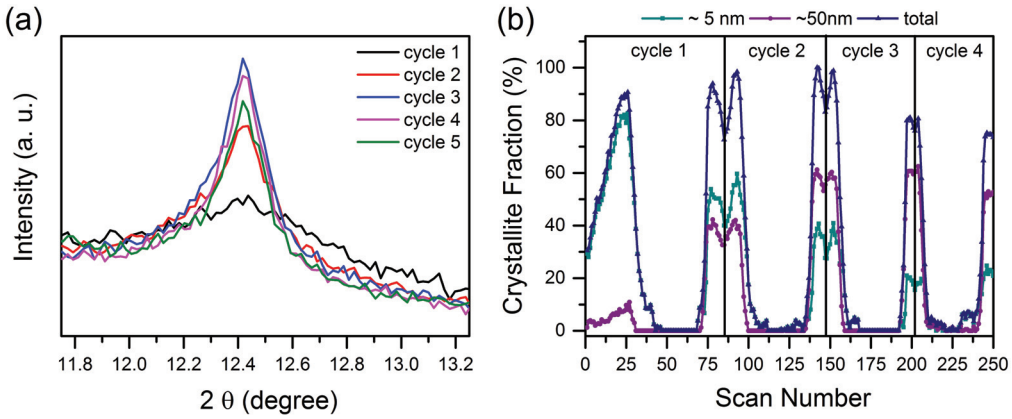

Figure 5.9: (a) Bi (0 1 2) peak broadening *vs.* cycle number (Mo radiation) and (b) evolution of the Bi crystallite size distribution during the first 4 cycles [Figure S7 of `Paper I`].

pared to 2.5 V and 3 V in the other studies [43, 159]. The conversion reaction of Bi_2S_3 is associated with the voltage plateaus at 1.20 V and 1.74 V during sodiation and desodiation, respectively. As can be seen from the change in slope at the end of this voltage plateau (Figure 5.8) it can be assumed that the reaction has finished before the cut-off voltage is reached. This voltage plateau, however, also fades even if the batteries are cycled to higher voltages as can be seen from comparison of the voltage profiles shown for several cycles in the other works [43, 159]. It is therefore reasonable to assume that the fading in their samples is due to a similar mechanism. Nanostructuring of the electrode seems to help improve the reversibility of the conversion reaction compared to the micro-sized material used in our work.

In continuation of our work on Bi-based conversion reactions we attempted a novel type of conversion reaction based on ternary Bi metalates. We were hoping for conversion of $BiVO_4$ and $Bi_2(MoO_4)_3$ to Bi and Na_3VO_4 and $Na_2(MoO_4)$, respectively, in a first step, followed by further conversion of Na_3VO_4 and $Na_2(MoO_4)$ to Na_2O and V and Mo, respectively, in a second step which would yield very high specific capacities. In order to determine their working mechanisms we used electrochemical methods, *operando* XANES and DFT characterization. XRD could not be used in this study

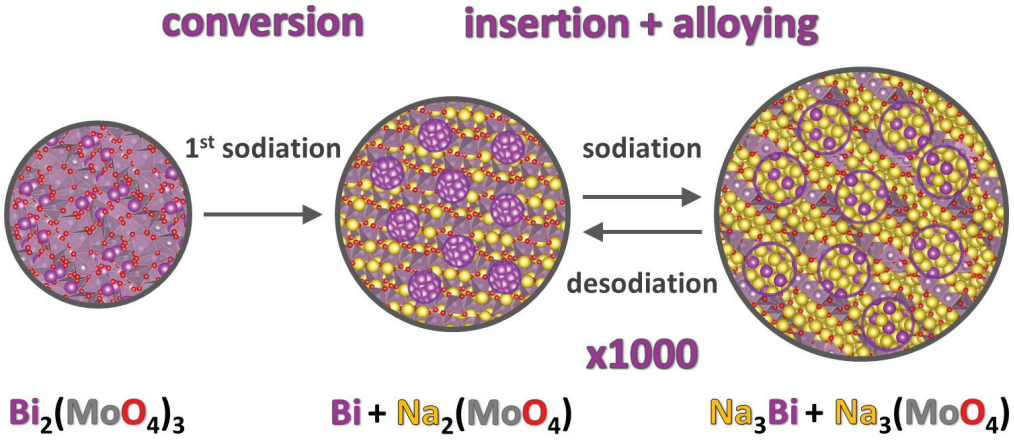

Figure 5.10: Illustration of the working mechanism of ternary Bi metalates using $Bi_2(MoO_4)_3$ as an example [Abstract graphic of `Paper IV`].

since the electrode materials were found to amorphize during the first sodiation. The working mechanism and the electrochemical performance of the ternary Bi metalates are described in detail in `Paper IV`. An illustration of the proposed working mechanism for $Bi_2(MoO_4)_3$ is shown in Figure 5.10. The first conversion was found to be present but irreversible and instead of the second conversion a reversible Na insertion mechanism in $Na_{3+x}VO_4$ and $Na_{2+x}(MoO_4)$, respectively, with $x \leq 1$ was revealed. During the initial cycle the anode is thus converted into nanocrystallites of alloying material confined in a matrix of nanocrystalline insertion compounds. The initial Coulombic efficiency and the practical specific capacity are compromised by this working mechanism, while the nanostructuring of the anode during the initial cycle gives rise to very stable capacity retention over hundreds of cycles.

$BiVO_4$ and $Bi_2(MoO_4)_3$ exhibit high specific capacities, excellent cycling stability and high-rate performance. $Bi_2(MoO_4)_3$ for example retains 79 % of its initial charge capacity of 352 mAh/g at ∼1C over 1000 cycles which is exceptionally high for alloying anodes (see for example `Paper III`). The Bi metalates operate in the optimal voltage range for SIBs with respect to safety concerns and energy density. They moreover have low environmental load and low manufacturing costs (*e.g.* $BiVO_4$ is a yellow pigment that is produced by major chemical companies). For these reasons the Bi metalates

are suitable candidates for anode materials in large-scale electrical energy storage applications.

5.3 Concluding remarks and outlook

In the course of this dissertation, a fully operational set-up (electrochemical cells, sample changer and interfacing software) that enables combined quasi-simultaneous *operando* X-ray diffraction (XRD) and X-ray absorption spectroscopy (XAS such as XANES and EXAFS) measurements coupled with electrochemical characterization was designed and commissioned. This set-up was developed to study working and degradation mechanisms of electrode materials. The understanding of these is fundamental to the optimization of electrode materials for rechargeable non-aqueous batteries. The combined approach of *operando* XRD and XAS enables deep insights into electrochemical reaction processes (*i.e.* insertion, alloying, conversion), structural stability (*e.g.* amorphization, pulverization) and voltage-composition profiles (single phase *vs.* multi-phase) along with details on the oxidation state and the local environment of the electrochemical redox-active species. Using this set-up, working and degradation mechanisms of several SIB electrode systems could be revealed in this dissertation:

- In the PBA $Na_{1.32}Mn[Fe(CN)_6]_{0.83} \cdot z\,H_2O$ SIB insertion cathode material different desodiation and sodiation mechanisms give rise to pronounced differences in the galvanostatic charge and discharge profiles. Synthetic conditions influencing the amount of $[Fe(CN)_6]$ vacancies and water content are critical factors for the performance of PBAs in a battery. They influence both the structural changes upon cycling and formation of an electrochemically inactive residual phase causing capacity degradation.

- Studying Bi as alloying anode material for SIBs, we found that crystallite size effects can influence the performance of battery materials by making the structural chemistry deviate from what is predicted by the equilibrium phase diagram. Using crystallite size to direct the struc-

tural chemistry we may be able to improve the lifetime of high capacity batteries effectively and at low cost.

- The conversion anode material Bi_2S_3 was found to form nanocrystallites of Bi which are alloyed with Na during the initial sodiation. During further cycling, agglomeration of the Bi particles gives rise to a reduction of the active surface area which leads to loss of the reversibility of the conversion reaction. To open the possibility of better cycling stability it is hence important to identify materials or formulate electrodes in which particle agglomeration during cycling is suppressed. The following class of anode materials provides such properties:

- Ternary metalates such as $BiVO_4$ and $Bi_2(MoO_4)_3$ were identified as a novel class of high performance SIB anode materials. During the first cycle the initial compounds are converted into alloying Bi nanocrystallites confined in a matrix of electrochemically active insertion hosts, *i.e.* $Na_{3+x}VO_4$ and $Na_{2+x}(MoO_4)$, respectively. The nanostructured composite anode so obtained enables excellent high rate performance and very stable capacity retention for alloying anodes over hundreds of cycles. The low initial Coulombic efficiency remains to be addressed.

As demonstrated by the various insertion-, alloying- and/or conversion-based electrode systems studied in this dissertation, our current experimental set-up for combined *operando* XRD/XAS allows us to follow atomistic changes in electrode materials during cycling and to put them into context with the electrochemical properties of the electrode systems. In this dissertation, different material-related properties such as vacancy and water content, crystallite size and nanostructuring were found to affect the structural chemistry during cycling. By tuning these properties we can improve the battery performance of the electrode materials.

As confirmed for various examples in this dissertation *operando* characterization has many advantages over *ex situ* analysis: (1) *Ex situ* samples have to be carefully prepared to avoid short circuiting of the electrodes and contamination with atmospheric species which otherwise may yield misleading results (*e.g.* studies of Bi and Bi_2S_3); (2) Limited data point density along the voltage profile may miss fine details of the working mechanism (*e.g.* study

of $Na_{1.32}Mn[Fe(CN)_6]_{0.83} \cdot z\,H_2O$); (3) Long term cycling experiments along with *operando* X-ray characterization become practically feasible and activation/degradation mechanisms can be studied (*e.g.* study of Bi_2S_3). The long term cycling stability of the *operando* cell was demonstrated in `Paper I`. Representative information for the working mechanism can usually be obtained within one full cycle. If, however, many irreversible reactions take place during the first sodiation or desodiation it is advisable to study the first 1.5 cycles or more. In long term studies the number of cycles that can be measured must be traded off against the available measurement time. It might thus be beneficial to compare selected cycles only, depending on the expected activation/degradation mechanisms. Most of the cycling would then be done *ex situ* without *operando* characterization; (4) Using *operando* X-ray characterization with sufficient time resolution it becomes possible to investigate the structural and electronic response when the battery is cycled under non-equilibrium conditions. Short-lived intermediates and non-linearities in behaviour can then be resolved. For Li_xFePO_4, for example, it was found that overpotential under high applied currents suppresses the equilibrium two-phase behaviour [174]. In this context, it would be interesting to study the influence of increasing C-rates on the working mechanism of the microcrystalline Na–Bi system and whether overpotential can stabilize the cubic Na_3Bi phase. (5) Advanced synchrotron *operando* methods can be used to disclose the cycling rate-dependent phase transition mechanism within individual electrode particles using microbeam XRD [175] or the strain evolution within individual electrode particles using coherent X-ray diffractive imaging [201–203].

In this dissertation structural changes in electrode materials during cycling were studied using XRD, a method which is limited to the determination of the atomic arrangement in crystalline solids. The best performing anodes, however, are often nanostructured, highly disordered and/or amorphous systems (*e.g.* the ternary Bi metalates). Their working mechanisms cannot be revealed using conventional XRD methods. The advanced Rietveld analysis of the Bi_2S_3 conversion anode probably represents the maximum level of information that can be extracted for a working mechanism which includes nanocrystalline materials (2-10 nm). It is worth noting that it may

not be possible to apply this type of analysis to any system. Combining XRD and XANES analysis for the Bi system we could exclude the formation of intermediate amorphous phases. Using EXAFS analysis it is possible to obtain information on the local environment of a specific element. However, if many elements are involved and multiple phases are present simultaneously this method might not be sufficient to fully understand the working mechanism of an electrode material. Generally, combining complementary methods for studying electrode systems provides the deepest insights into the working mechanism of electrode materials as was pointed out in Section 2.6. The structural evolution of nanocrystalline/amorphous materials in electrodes can hence be followed to a certain degree using combined XRD and XAS. Total scattering often in the form of pair distribution function (PDF) analysis, is a more sophisticated technique for studying non-crystalline solid materials and which provides more detailed information on the voltage composition profiles of electrode systems with amorphous (intermediate) phases. This type of analysis was demonstrated for Sb by Allan *et al.* [125]. A similar analysis would have been beneficial for studying the reaction mechanism of the ternary metalates, which lose their long range order during the initial sodiation. Total scattering is possible at the SNBL and efforts should be devoted to implementing this method using the *operando* cell presented in this dissertation. For total scattering analysis it is important to deconvolute the signal of the sample from the background scattering. However, since the X-ray beam passes through the entire stack of battery components a reliable background subtraction for data analysis is problematic.

Various methods for *operando* imaging of morphological, chemical and structural changes at the electrode particle level are being developed. Future development of instruments and methods, will enable us to obtain structural and chemical information in a spatially resolved manner, with spatial resolution on or beyond the scale of the electrode particles and time scales capable of resolving the chemical reactions taking place during cycling of the battery. Coming upgrades of synchrotron sources, to reduce divergence and increase brilliance, as well as free electron lasers, and faster area detectors with lower noise, are examples of such developments. *Operando* X-ray absorption tomographic/imaging methods [193, 194, 234] can reveal the evol-

ution of the three dimensional spatial arrangement of the active material in the electrode film and its mechanical degradation (*e.g.* volume expansions of particles or electrode film, particle cracking, particle/matrix formation during conversion reactions, dendrite formation, metal deposition). *Operando* X-ray microscopy yields chemical evolution in addition to morphological changes of electrode particles in two dimensions [196, 197]. Although yet too time consuming for *operando* investigations three dimensional chemical imaging is also possible [195]. At low X-ray energies this method could also be used to investigate the passivation layer (SEI) at the interface between electrode particles and electrolyte as indicated in [166]. Here, more information could be obtained for SIBs than for LIBs because the absorption K-edge of Na but not of Li could be probed. It, however, remains questionable whether these studies have to be performed *ex situ* or whether an electrochemical cell could be designed that allows for sufficient data quality at these low X-ray energies. Using advanced methods like dynamic XRD/total scattering computed tomography [198–200] we will be able to resolve structural and chemical information (chemical species and their bond distances, coordination numbers and hence oxidation states) in three dimensional space and in time/charge state. This may prove particularly advantageous for total scattering analysis because the data obtained for each subvolume (*e.g.* within the electrode) will intrinsically be background subtracted by the reconstruction method. XRD/total scattering computed tomography will elucidate degradation mechanisms such as transition metal dissolution and re-precipitation of new phases, as well as residual phase formation due to mechanical degradation. This method further provides an unprecedented direct means of studying the formation and degradation mechanisms of the amorphous SEI extending over at most a few micrometers by resolving its atomic structure. Additional information on the SEI species could be supplied from complementary techniques such as NMR [210, 211] and TEM [204, 209, 212]. Although the analogy to conventional battery configurations is much higher for X-ray based characterization, TEM analysis provides better spatial resolution (atomic resolution *vs.* 20-30 nm for X-ray microscopy [166]). To provide the most comprehensive understanding of the working and degradation mechanisms of batteries, *i.e.* heterogeneous multi-component systems, we need to be

able to characterize these across a range of length scales using TEM, X-ray microscopy and computed tomography, along with classic electrochemistry, diffraction, spectroscopy, and other existing and emerging techniques. The knowledge gained through synchrotron based *operando* characterization of non-aqueous rechargeable batteries is certain to play an important role in building the batteries of the future.

Chapter 6

Contributions to other aspects of non-aqueous rechargeable batteries

This chapter presents the supplementary research papers which are related to other aspects of non-aqueous rechargeable batteries, in terms of the metal ion system (Li instead of Na) and/or the methods used to study their working mechanisms. `Paper V` reports an *operando* synchrotron study of ordered and disordered high voltage spinel $LiMn_{1.5}Ni_{0.5}O_4$ for LIB cathodes and `Paper VI` presents a combined *ab initio* computational and experimental study of the Na and Li insertion mechanism into fully amorphous (glassy) carbon. These works, in particular the structural or electrochemical data collection and analysis thereof, were important for the commissioning of the electrochemical cell (`Paper I`) and for testing of the capacity contribution of carbon to the Bi and Bi metalate carbon composite anodes (`Paper III` and `Paper IV`). The key findings of these supplementary research papers are therefore summarised, discussed and put into a broader context here, in a separate chapter, because they are related but not central to the main findings of this dissertation on *operando* X-ray studies of SIB materials with an emphasis on anode materials. A list of the research papers and a statement of my contributions to these can be found in the front matter.

6.1 *In situ* synchrotron study of *ordered* and *disordered* $LiMn_{1.5}Ni_{0.5}O_4$ as lithium ion battery positive electrode

Spinel $LiMn_{1.5}Ni_{0.5}O_4$ has attracted considerable attention as high gravimetric energy density (∼700 Wh/kg) cathode material for LIBs based on inexpensive and environmentally benign materials with good cycling stability [235]. It is one of the most energy-cost efficient systems and has a lower cost per kWh than standardized systems such as $LiCoO_2$ and $LiFePO_4$ [19].

Synthetic conditions (*e.g.* the heat treatment) affect the degree of Ni−Mn ordering in $LiMn_{1.5}Ni_{0.5}O_4$, oxygen non-stoichiometry influencing the Mn^{3+} content in $LiMn_{1.5}Ni_{0.5}O_{4-\delta}$, precipitation of electrochemically inactive $Li_xNi_{1-x}O$ and particle morphology which in turn give rise to different electrochemical performances [225, 236, 237].

The space group, *P4₃32* and *Fd-3m* for ordered and disordered $LiMn_{1.5}Ni_{0.5}O_4$, respectively, can be determined qualitatively using spectroscopic methods such as Raman or FTIR spectroscopy and high quality XRD or TEM data, which reveal the presence of additional modes and superlattice reflections respectively for the ordered sample [236, 238]. More quantitative analysis of, for example, the degree of Ni−Mn ordering is possible using neutron powder diffraction [225, 237].

In the literature the electrochemical performance of $LiMn_{1.5}Ni_{0.5}O_4$, in particular its rate performance, has been discussed with respect to the degree of Ni−Mn ordering which gives rise to different structural responses upon cycling [237–246]. The structural response upon cycling has been investigated using *operando* XRD for many ordered and disordered $LiMn_{1.5}Ni_{0.5}O_4$ samples. Ordered $LiMn_{1.5}Ni_{0.5}O_4$ exhibits two-step two-phase behaviour with stable compositions of $LiMn_{1.5}Ni_{0.5}O_4$ (cubic phase I with $8.15\text{Å} \leq a \leq 8.17\text{Å}$), $Li_{0.5}Mn_{1.5}Ni_{0.5}O_4$ (cubic phase II with $a \approx 8.09\text{Å}$) and $Mn_{1.5}Ni_{0.5}O_4$ (cubic phase III with $a \approx 8.01$) [237–246]. The unit cell variation of cubic phase I in some samples is associated with a change in Mn oxidation state and the smaller size of Mn^{4+} compared to Mn^{3+}. While the literature reports on the structural changes during cycling of the ordered variant are consist-

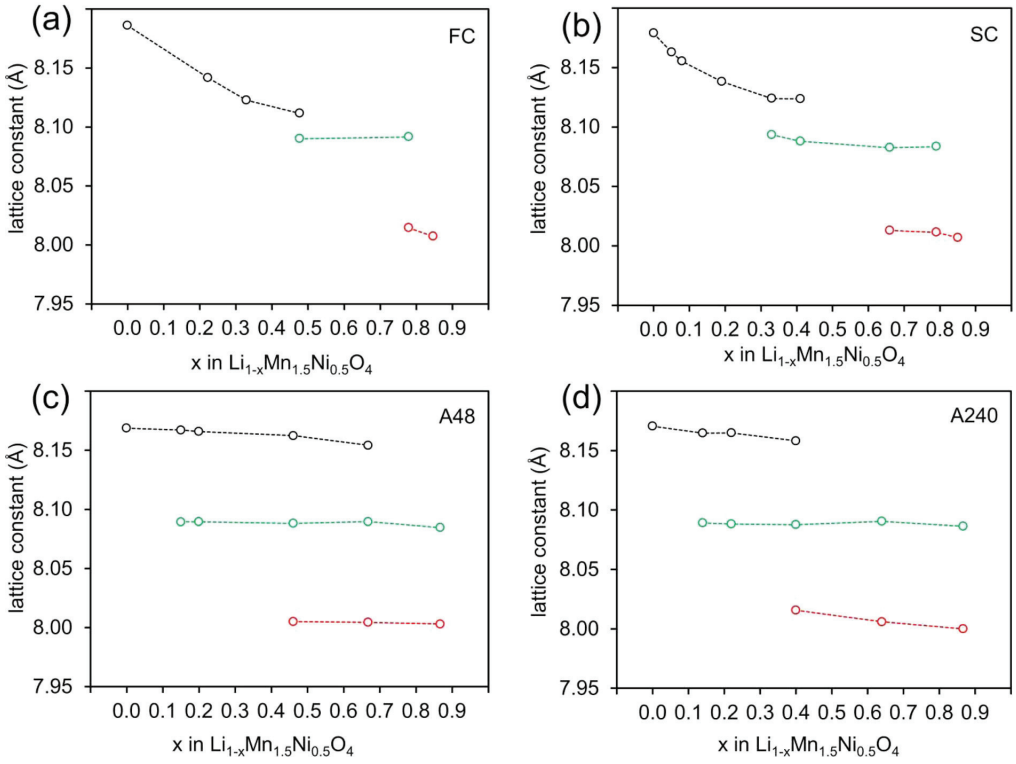

Figure 6.1: Lattice parameter of chemically delithiated $LiMn_{1.5}Ni_{0.5}O_4$ plotted as a function of Li content for various samples with increasing degree of Ni−Mn ordering from (a) to (d)[237].

ent, two different observations were made for its disordered counterpart: (1) The structural response is similar to the ordered counterpart but with extended solid solution behaviour of cubic phase I, which is also reflected in the larger variation in the cubic unit cell parameter ($8.11\text{Å} \leq a \leq 8.17\text{Å}$) [237, 240, 243, 244]; (2) The first two-phase step between cubic phases I and II is omitted and the solid solubility range is extended with the cubic unit cell parameter of phase I decreasing to that of phase II, while the two-phase step involving phase III remains [239, 241, 246]. It remains unclear why these different observations are made for the disordered samples. The XRD study by Moorhead-Rosenberg *et al.* was performed *ex situ* on chemically delithiated samples (Figure 6.1) [237]. Their diffraction patterns therefore

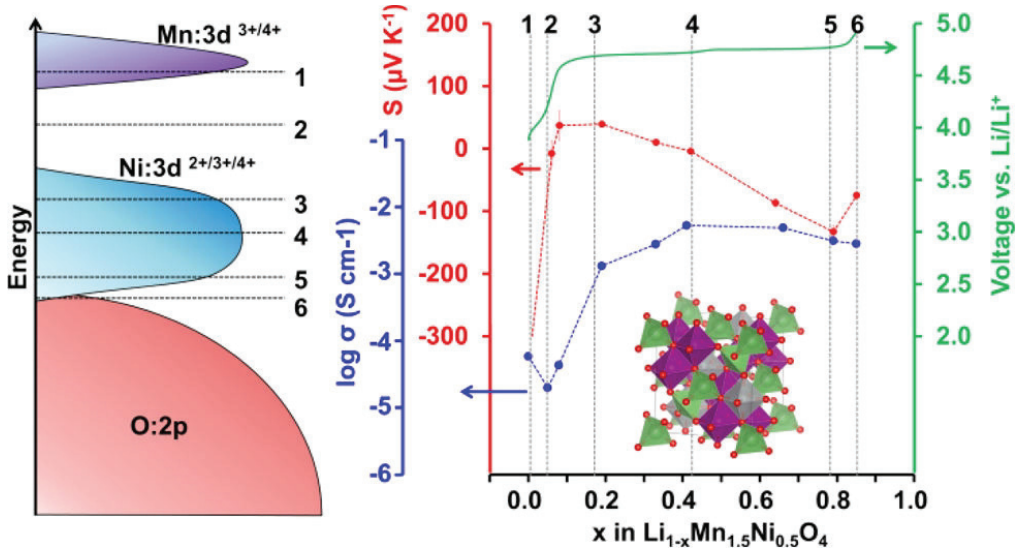

Figure 6.2: Illustration of the Fermi energy and density of states, cell voltage, Seebeck coefficient, and electronic conductivity plotted as a function of Li content inNi−Mn disordered $LiMn_{1.5}Ni_{0.5}O_4$ [237].

reveal the thermodynamically stable phases. The structural changes they observe are of type (1) for their disordered samples. Deviations for the equilibrium reaction path may occur at elevated C-rates. The *operando* studies performed at low/moderate C-rates (C/20<C/6) were found to be of type (1) [240, 243, 244], while type (2), *i.e.* solid solubility of cubic phases I and II was observed at higher C-rates (C/3<1C) [239, 241]. Note that due to the variable cubic unit cell parameter of phase I, the reduced number of XRD patterns at elevated C-rates and limited instrumental resolution of the diffraction profile, it might be problematic to distinguish between type (1) and (2). The ordered variant exhibits two-phase behaviour and its disordered counterpart shows increasing ranges of solid solution Li insertion with decreasing degree of Ni−Mn ordering. In most of the literature better rate performance was found for the disordered variant. The solid solubility of Li in disordered $LiMn_{1.5}Ni_{0.5}O_4$ is therefore commonly taken as a critical factor for fast kinetics, while two-phase behaviour in the ordered counterpart and associated interphase boundaries for Li diffusion limit the rate performance. Another

aspect that is traditionally considered when assessing the rate performance of this class of materials is the initial Mn^{3+} content [247]. The disordered material tends to have more Mn^{3+} giving rise to higher conductivity in the pristine state.

Moorhead-Rosenberg *et al.* performed a systematic study of the electronic and electrochemical properties of $LiMn_{1.5}Ni_{0.5}O_4$ as a function of Li content for several samples with different degrees of Ni−Mn ordering (Figure 6.2) [237]. By conductivity and activation energy measurements they confirmed that charge transfer takes place via small polaron hopping and that the charge carrier conduction is easier in the Ni:3d band than the Mn:3d band. Their Seebeck data confirmed that $Ni^{2+/3+}$ and $Ni^{3+/4+}$ redox couples are part of a single or highly overlapping 3d band. The highest electronic conductivity is thus observed near a Li content of 0.5 (Ni^{3+}), while the lowest electronic conductivity (about three orders of magnitude difference) was measured close to a Li content of 1 (at the gap between $Mn^{3+/4+}$ and $Ni^{2+/3+}$ redox couples) for all samples. The conductivity measurements were further compared to the phase transformation mechanisms of the various samples with different degrees of Ni−Mn ordering. Both ordered samples exhibit two separate two-phase regions and both disordered samples show solid solubility above Li contents of 0.5. The most ordered sample displays inferior rate performance over the other samples, while the slightly less ordered sample shows similar rate performance to the disordered samples. They suggest that the high rate capability of the slightly ordered $LiMn_{1.5}Ni_{0.5}O_4$ might be enabled by a kinetic solid solution at the two-phase boundary which is more likely to form than in the highly ordered variant. This would fit with the findings of Komatsu *et al.* which indicate the presence of such intermediate states in addition to the thermodynamically stable phases in disordered $LiMn_{1.5}Ni_{0.5}O_4$ [248]. The results of Moorhead-Rosenberg *et al.* challenge the previous assumptions that low Mn^{3+} content is responsible for poor rate performance and that thermodynamic solid-solubility is fundamental for fast Li diffusion.

Samarasingha *et al.* synthesised Ni−Mn ordered and disordered samples using the Pechini method followed by different heat treatment programs (Figure 6.3) and investigated their electrochemical performance [225]. The

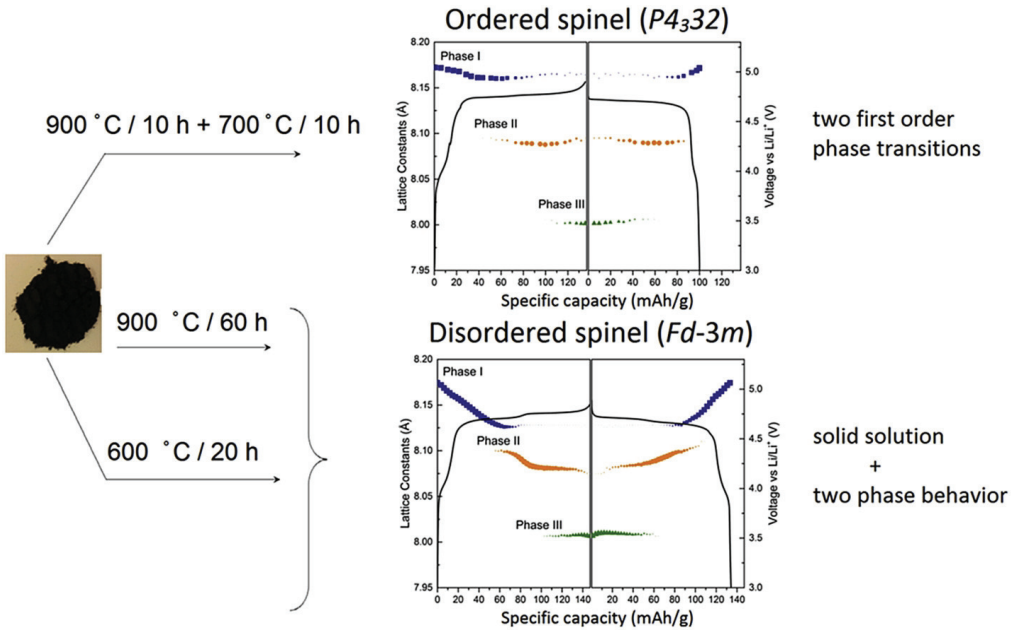

Figure 6.3: Illustration showing that different heat treatment during synthesis results in different degrees of Ni−Mn ordering in spinel $LiMn_{1.5}Ni_{0.5}O_4$ which impacts the structural response during cycling. The evolution of the cubic lattice constants of ordered and disordered $Li_{1-x}Mn_{1.5}Ni_{0.5}O_4$ are compared with their voltage profiles. The size of the symbols was scaled to the relative phase fractions. [Abstract graphic of `Paper V`].

cation ordering was determined using Raman spectroscopy and, for selected samples, using neutron powder diffraction. Surprisingly, one of the ordered variants shows the best electrochemical behaviour in terms of specific capacity, cycling stability and rate performance. This sample shows some Ni−Mn site disorder (about 5 %) in space group $P4_332$, as revealed by Rietveld refinement of the neutron diffraction pattern. `Paper V` is a continuation of the previous work by Samarasingha *et al.* [225]. In `Paper V` we studied differences in working mechanisms of Ni−Mn selected ordered and disordered structural variants of $LiMn_{1.5}Ni_{0.5}O_4$ upon cycling (Figure 6.3).

Using *operando* quasi-simultaneous synchrotron XRD/XAS a series of first order structural phase transitions (two-phase behaviour) was found and

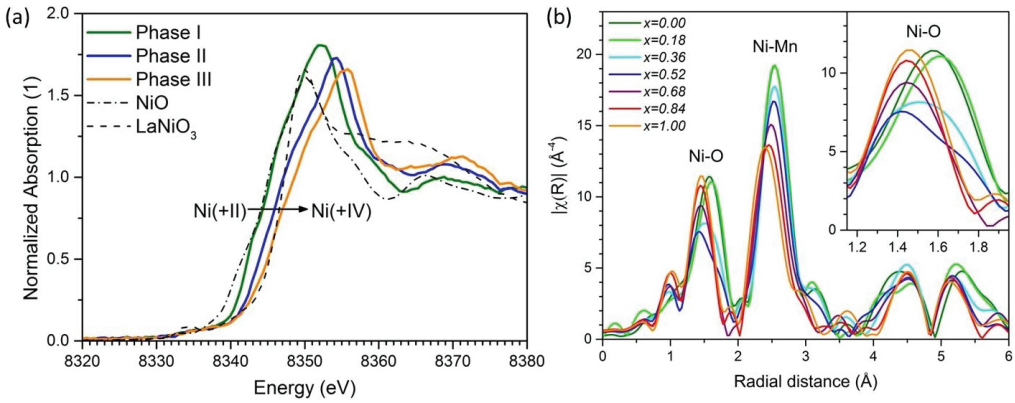

Figure 6.4: (a) Ni K-edge XANES spectra of ordered $Li_{1-x}Mn_{1.5}Ni_{0.5}O_4$ collected at the maximum phase fraction of the corresponding phases compared to Ni^{2+} and Ni^{3+} references. (b) Radial structure function for $Li_{1-x}Mn_{1.5}Ni_{0.5}O_4$ obtained from Fourier transformation of k^3-weighed Ni K-edge EXAFS oscillations ($\Delta k = 3 - 12 \text{Å}^{-1}$) without correction for the phase shift. The pronounced broadening of the Ni–O interaction at maximum phase fraction of phase II (x =0.68) indicate a distortion of the Ni^{3+}–O_6 octahedron. [Figures 4 and 5 of `Paper I`].

each phase could be linked to a different oxidation state of Ni (*i.e.* Ni^{2+}, Ni^{3+} and Ni^{4+}) in the Ni–Mn ordered compound (Figure 6.4(a)). Based on the qualitative *operando* EXAFS analysis (presented in `Paper I`) we suggested a Jahn-Teller distortion of the Ni–O_6 octahedron for Ni^{3+} while no distortion was found for Ni^{2+} and Ni^{4+} (Figure 6.4(b)). Although the same series of first order structural transitions was observed by *operando* XRD in the Ni–Mn disordered samples, the more pronounced variation in lattice parameters of cubic phases I and II indicated a higher degree of solid solubility, which seems to be enabled by the cation disorder (Figure 6.3). The structural response upon cycling seems not to be affected by different particle morphologies of the samples since both disordered samples show similar structural changes while having different particle morphologies (one being nanocrystalline in the form of platelets and the other microcrystalline like the ordered sample) [225]. This is in good agreement with the observations by Hai *et al.* on ordered $LiMn_{1.5}Ni_{0.5}O_4$ of octahedral and plate-like shapes [242].

The structural changes reported in `Paper V` are in good agreement with the previous *operando* XRD studies mentioned above. The XAS analysis agrees with previous *operando* XANES [239, 249–253] and EXAFS studies [238, 239, 250]. `Paper I` presents our first EXAFS measurements and a qualitative analysis thereof. A quantitative XAS analysis was presented by Rana *et al.* [250] which illustrates well the potential of *operando* XAS investigations of batteries. Rana *et al.* do not comment on the possible Jahn-Teller distortion of the $Ni^{3+}-O_6$ octahedron and rather associate the wider distribution of Ni–O bond distance at 4.7 V with the coexistence of multivalent Ni ions (of different ionic radii) in the material.

Here, we report for the first time a solid solubility of cubic phase II with a variation in the unit cell parameter (8.10Å $\leq a \leq$ 8.08Å) in the disordered samples. Such an observation was previously only reported for M-doped $LiMn_{1.5}Ni_{0.5}O_4$ (M=Cr, Co, Mg) [238, 254, 255]. Interestingly doping improves the rate performance and cycling stability of $LiMn_{1.5}Ni_{0.5}O_4$ and the improved electrochemical performance was attributed to the increased solid solubility of Li leading to smoother structural changes in the doped spinel [236, 238, 254]. Although our disordered samples show a similar degree of solid solubility, worse cycling stability compared to the more ordered sample with two-phase behaviour was found [225]. These observations suggest that cycling stability is not only affected by the working mechanism but also other mechanisms giving rise to degradation. These include Mn dissolution and side reactions with the electrolyte [235] which may further depend on factors such as the particle morphology and electrode preparation (not compared here). The ordered sample with its two-phase behaviour shows excellent high rate performance, which is surprising for this material [225]. The partial Ni–Mn site disorder (about 5 %) in this sample [225] may enable a kinetic solid solution at the two-phase boundary as suggested by Moorhead-Rosenberg *et al.* [237]. The rate performance of the ordered and disordered samples were probably not compared in the previous report by Samasingha *et al.* because of the limited cycling stability of the disordered samples [225].

Which of the structural modifications (ordered, partially ordered or disordered) performs best in a battery remains an open question in the literature. Further studies should hence be conducted with emphasis on the degree

of Ni−Mn ordering and associated structural changes. An *operando* XRD study of the working mechanism at elevated C-rates similar to the works of Zhang *et al.* [174, 175] and Komatsu *et al.* [248] could verify the presence of a kinetic solid solution as a function of the degree of Ni−Mn ordering in $LiMn_{1.5}Ni_{0.5}O_4$.

It is worth noting that the cycling stability is also affected by other degradation mechanisms than those resulting from difficult structural transitions upon cycling. The high operation voltage of $LiMn_{1.5}Ni_{0.5}O_4$ ($\sim$4.7 V) may result in surface destabilization, transition metal leaching and electrolyte decomposition, especially at elevated temperatures. Doping and particle surface modifications in addition to optimization of electrolytes (using additives) help to achieve high energy densities combined with long cycle life [235, 236].

6.2 Amorphous (Glassy) Carbon, a Promising Material for Sodium Ion Battery Anodes: a Combined First-Principles and Experimental Study

Carbon materials are interesting for use in SIBs because they are potentially inexpensive, environmentally benign and show good cycling stability (Section 2.5.2). Graphite is the most commonly used anode material in LIB technology [30, 31]. Na, unlike Li, does not intercalate well into graphite [21, 99]. In analogy to graphite, crystalline Si does not show a sufficient degree of sodiation in a SIB [127, 256]. The highest obtained reversible capacity in crystalline Si spherical nanoparticles (20 nm in diameter) of 279 mAh/g represents less than a third of the theoretical capacity for the formation of NaSi (954 mAh/g) [131]. Calculations (one of them by our collarborators Legrain *et al.*) indicated that amorphous Si is more favourable for reaction with Na [257, 258]. This was to some extent confirmed experimentally [259–261]. In a similar manner amorphization of carbon could improve its Na storage capabilities. Hard and soft carbons (both being disordered carbons with a certain degree of graphitization) showed improved reversible capacities of up to 300 mAh/g and 120 mAh/g respectively when cycled against Na

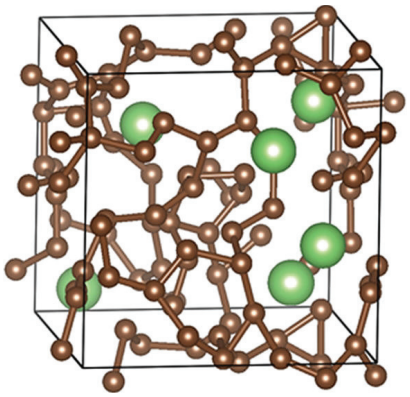

Figure 6.5: Illustration of the atomic arrangement in sodiated/lithiated fully amorphous (glassy) carbon [Abstract graphic of `Paper VI`].

[28, 63, 97, 99, 102, 103]. Amorphous carbon has previously only been investigated as a Li ion capacitor [262]. The effect of full amorphization of carbon on the energetics of lithiation and sodiation was not investigated previously.

In `Paper VI` we present a combined *ab initio* computational and experimental study of the mechanism of Na and Li insertion into fully amorphous (glassy) carbon (Figure 6.5). The calculations confirm that Na insertion into graphite is not preferred, while multiple insertion sites with binding energies stronger than the Na cohesive energy were identified in amorphous carbon. Li insertion was found to be thermodynamically favoured in both amorphous carbon and graphite. For the experimental confirmation of these results fully amorphous carbon was derived from partially ordered carbon black via high energy ball milling. A sloped voltage profile in the 0-1.6 V range and highly reversible cycling behaviour with specific capacities of 173 mAh/g and 390 mAh/g after 100 cycles for Na and Li, respectively, close to their theoretical estimates (with a metal to carbon ratio of 5/64 and 11/64, respectively) were found. Reversible capacity was improved with respect to carbon black by making it fully amorphous (Figure 6.6). Other soft carbons also exhibit lower specific capacities than the glassy carbon in a SIB [28, 99, 102, 103]. The fully amorphous carbon does not reach the energy densities of hard carbon in a SIB because of both lower specific capacities and higher average voltage operation. Additional capacity in hard carbon is available due to

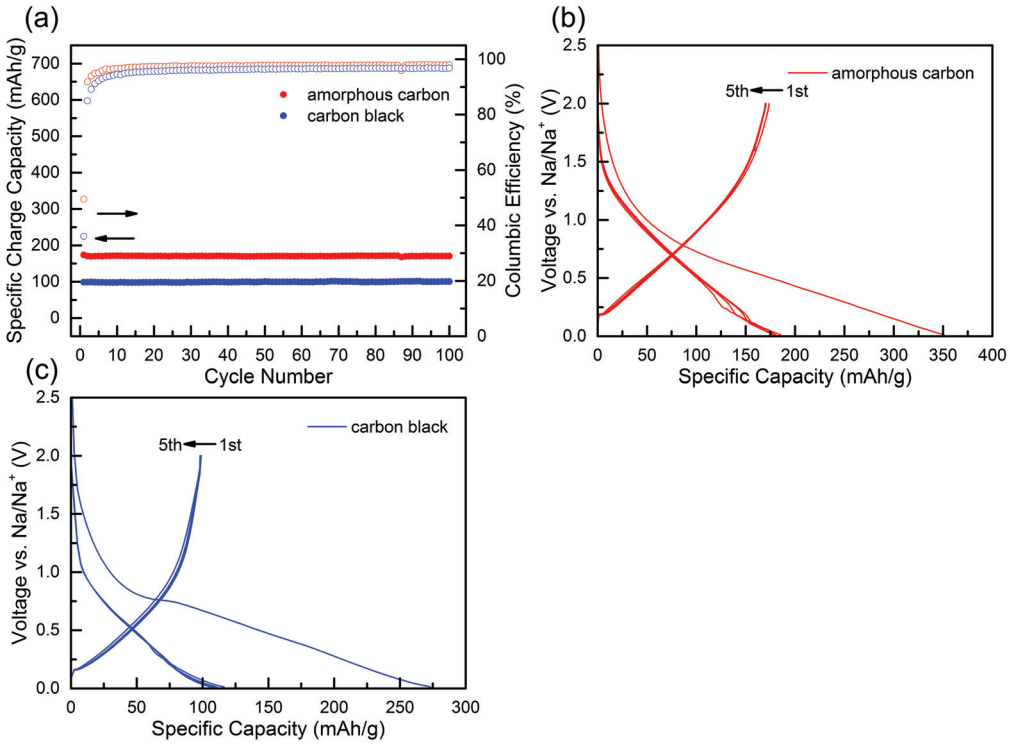

Figure 6.6: (a) Specific capacity and Coulombic efficiency as a function of cycle number, and voltage profiles for the first 5 cycles of (b) amorphous carbon and (c) Super P carbon black *vs.* Na.

Na absorption within nanopores [28, 63, 97]. The sloped voltage profile of the amorphous carbon on one hand reduces its energy density compared to hard carbon but may on the other give rise to better high-rate performance and lower risk of Na plating. Another drawback of the amorphous carbon is its low initial Coulombic efficiency of 53 %; lower than that of hard carbon (∼80 % [63]) but higher than that of carbon black (36 %). The low first cycle Coulombic efficiency may be attributed to irreversibly trapped Na in the carbon, SEI formation or other irreversible passivation processes. The use of glassy carbon in a LIB, despite its high specific capacity, is not preferred over graphite because of the higher average operation voltage and low initial Coulombic efficiency of 63 % which are associated with a lower energy

density in a full cell.

The knowledge gained in this work is also relevant to studies of other anodes employing carbon (*e.g.* Super P carbon black) as conductive additive or as a composite with alloying or conversion anode materials, *e.g.* P/C [110, 111], Sb/C [122], and Bi and Bi metalate carbon composite anodes (`Paper III` and `Paper IV`). One should keep in mind that the different carbons will contribute to both the irreversible and reversible capacities in composite anodes.

Bibliography

[1] P. Taylor, R. Bolton, D. Stone, X.-P. Zhang, C. Martin, and P. Upham, *Pathways for energy storage in the UK*, Report (Centre for low carbon futures, York, 2012) available at http://www.lowcarbonfutures.org/sites/default/files/Pathways%20for%20Energy%20Storage%20in%20the%20UK.pdf.

[2] H. H. Larsen and L. S. Petersen, *DTU International Energy Report 2013: Energy storage options for future sustainable energy systems*, Report ISBN 978-87-550-3968-1 (Technical University of Denmark, November 2013) available at www.natlab.dtu.dk/-/media/Andre_Universitetsenheder/Nationallab_for_Baeredygtig_Energi/NatLabPics/H2020/DTU%20International%20Energy%20Report%202013_Energy_storage.ashx?la=da.

[3] X. Luo, J. Wang, M. Dooner, and J. Clarke, Applied Energy **137**, 511 (2015).

[4] *Grid Energy Storage*, Report (U.S. Department of Energy, December 2013) available at http://energy.gov/sites/prod/files/2014/09/f18/Grid%20Energy%20Storage%20December%202013.pdf.

[5] B. Dunn, H. Kamath, and J.-M. Tarascon, Science **334**, 928 (2011).

[6] *DG ENER Working Paper: The future role and challenges of Energy Storage*, Report (European Commission, 2015) available at https://ec.europa.eu/energy/sites/ener/files/energy_storage.pdf.

[7] *Technology roadmap: Energy storage*, Report (IEA, 2014) available at https://www.iea.org/publications/freepublications/publication/TechnologyRoadmapEnergystorage.pdf.

[8] *Energy Storage - Proposed policy principles and definition*, Report (European Commission, June 2016) available at https://ec.europa.eu/energy/sites/ener/files/documents/Proposed%20definition%20and%20principles%20for%20energy%20storage.pdf.

[9] *Battery storage for renewables: Market status and technology outlook*, Report (IRENA, 2015) available at http://www.irena.org/DocumentDownloads/Publications/IRENA_Battery_Storage_report_2015.pdf.

[10] *Renewables and electricity storage: A technology roadmap for REmap 2030*, Report (IRENA, 2015) available at http://www.irena.org/DocumentDownloads/Publications/IRENA_REmap_Electricity_Storage_2015.pdf.

[11] G. Rohling, *Electricity: The Future of Mobility*, Report (Siemens, 1 October 2014) available at http://www.siemens.com/innovation/en/home/pictures-of-the-future/mobility-and-motors/electric-vehicles-trends.html.
[12] *Bombardier Celebrates Innovative Battery Powered Train*, Report (Bombardier, 10 February 2015) available at http://www.bombardier.com/en/sustainability/sustainability-news/details.bombardier-transportation20150210bombardiercelebratesinnovativeb0.bombardiercom.sustainability.html?
[13] U. Kreutzer, *Electric Flight Takes Off*, Report (Siemens, 4 July 2016) available at http://www.siemens.com/innovation/en/home/pictures-of-the-future/mobility-and-motors/electromobility-electric-aircraft-maiden-flight.html.
[14] K. M. Tan, V. K. Ramachandaramurthy, and J. Y. Yong, Renewable and Sustainable Energy Reviews **53**, 720 (2016).
[15] *Battery storage power station*, Web Page (Wikipedia, accessed 6 July 2016) available at https://en.wikipedia.org/wiki/Battery_storage_power_station.
[16] C. J. Barnhart and S. M. Benson, Energy & Environmental Science **6**, 1083 (2013).
[17] *Global Market for Lithium-Ion Batteries - Forecast, Trends & Opportunities 2014-2020*, Report (Taiyou Research, 2014) available at http://www.marketresearch.com/product/sample-8323376.pdf.
[18] *Mineral commodity summaries 2015: U.S. Geological Survey*, Report (U.S. Department of the Interior, 2015) available at http://minerals.usgs.gov/minerals/pubs/mcs/2015/mcs2015.pdf.
[19] E. J. Berg, C. Villevieille, D. Streich, S. Trabesinger, and P. Nov k, Journal of The Electrochemical Society **162**, A2468 (2015).
[20] N. Yabuuchi, K. Kubota, M. Dahbi, and S. Komaba, Chemical Reviews **114**, 11636 (2014).
[21] M. D. Slater, D. Kim, E. Lee, and C. S. Johnson, Advanced Functional Materials **23**, 947 (2013).
[22] *An increasingly precious metal*, Report (The Economist Newspaper Limited) available at http://www.economist.com/news/business/21688386-amid-surge-demand-rechargeable-batteries-companies-are-scrambling-supplies.
[23] Y. Kim, K.-H. Ha, S. M. Oh, and K. T. Lee, Chemistry - A European Journal **20**, 11980 (2014).
[24] R. E. Ciez and J. F. Whitacre, Journal of Power Sources **320**, 310 (2016).
[25] J. W. Choi and D. Aurbach, Nature Reviews Materials **1**, 16013 (2016).
[26] H. Pan, Y.-S. Hu, and L. Chen, Energy & Environmental Science **6**, 2338 (2013).
[27] C. Pillot, *The rechargeable battery market*, Presentation (Avicenne, Batteries 2014, Nice, France, September 2014) available at http://www.

rechargebatteries.org/wp-content/uploads/2015/01/Avicenne-market-review-Nive-2014.pdf.
[28] C. Bommier and X. Ji, Israel Journal of Chemistry **55**, 486 (2015).
[29] P. Barpanda, Chemistry of Materials **28**, 1006 (2016).
[30] N. Nitta, F. Wu, J. T. Lee, and G. Yushin, Materials Today **18**, 252 (2015).
[31] S. Goriparti, E. Miele, F. De Angelis, E. Di Fabrizio, R. Proietti Zaccaria, and C. Capiglia, Journal of Power Sources **257**, 421 (2014).
[32] M. K. Aydinol, A. F. Kohan, G. Ceder, K. Cho, and J. Joannopoulos, Physical Review B **56**, 1354 (1997).
[33] I. A. Courtney, J. S. Tse, O. Mao, J. Hafner, and J. R. Dahn, Physical Review B **58**, 15583 (1998).
[34] A. Van der Ven, J. Bhattacharya, and A. A. Belak, Accounts of Chemical Research **46**, 1216 (2013).
[35] M. Tang, W. C. Carter, and Y.-M. Chiang, Annual Review of Materials Research **40**, 501 (2010).
[36] M. Z. Bazant, Accounts of Chemical Research **46**, 1144 (2013).
[37] D. Linden and T. B. Reddy, *Handbook of batteries* (McGraw-Hill, New York, 2002).
[38] W. Dreyer, J. Jamnik, C. Guhlke, R. Huth, J. Moskon, and M. Gaberscek, Nature Materials **9**, 448 (2010).
[39] M. T. McDowell, S. W. Lee, W. D. Nix, and Y. Cui, Advanced Materials **25**, 4966 (2013).
[40] B. Lu, Y. Song, Q. Zhang, J. Pan, Y.-T. Cheng, and J. Zhang, Physical Chemistry Chemical Physics **18**, 4721 (2016).
[41] R. E. Doe, K. A. Persson, Y. S. Meng, and G. Ceder, Chemistry of Materials **20**, 5274 (2008).
[42] H. C. Yu, C. Ling, J. Bhattacharya, J. C. Thomas, K. Thornton, and A. Van der Ven, Energy & Environmental Science **7**, 1760 (2014).
[43] L. Li, R. Jacobs, P. Gao, L. Gan, F. Wang, D. Morgan, and S. Jin, Journal of the American Chemical Society **138**, 2838 (2016).
[44] H. Kim, H. Kim, H. Kim, J. Kim, G. Yoon, K. Lim, W.-S. Yoon, and K. Kang, Advanced Functional Materials **26**, 1616 (2016).
[45] M. Park, X. Zhang, M. Chung, G. B. Less, and A. M. Sastry, Journal of Power Sources **195**, 7904 (2010).
[46] H. J. Gores, J. Barthel, S. Zugmann, D. Moosbauer, M. Amereller, R. Hartl, and A. Maurer, "Liquid nonaqueous electrolytes," in *Handbook of Battery Materials* (Wiley-VCH, 2011) pp. 525–626.
[47] J. C. Bachman, S. Muy, A. Grimaud, H.-H. Chang, N. Pour, S. F. Lux, O. Paschos, F. Maglia, S. Lupart, P. Lamp, L. Giordano, and Y. Shao-Horn, Chemical Reviews **116**, 140 (2016).
[48] J. B. Goodenough and Y. Kim, Chemistry of Materials **22**, 587 (2010).
[49] K. Xu, Chemical Reviews **114**, 11503 (2014).
[50] S. J. An, J. Li, C. Daniel, D. Mohanty, S. Nagpure, and I. Wood, D. L., Carbon **105**, 52 (2016).

[51] J. Vetter, P. Nov k, M. R. Wagner, C. Veit, K. C. M ller, J. O. Besenhard, M. Winter, M. Wohlfahrt-Mehrens, C. Vogler, and A. Hammouche, Journal of Power Sources **147**, 269 (2005).

[52] H. Xia, L. Lu, Y. S. Meng, and G. Ceder, Journal of The Electrochemical Society **154**, A337 (2007).

[53] D. Larcher, S. Beattie, M. Morcrette, K. Edstrom, J.-C. Jumas, and J.-M. Tarascon, Journal of Materials Chemistry **17**, 3759 (2007).

[54] D. H. P. Kang, M. Chen, and O. A. Ogunseitan, Environmental Science & Technology **47**, 5495 (2013).

[55] D. Kundu, E. Talaie, V. Duffort, and L. F. Nazar, Angewandte Chemie International Edition **54**, 3431 (2015).

[56] D. A. Stevens and J. R. Dahn, Journal of The Electrochemical Society **147**, 1271 (2000).

[57] V. Palomares, P. Serras, I. Villaluenga, K. B. Hueso, J. Carretero-Gonzalez, and T. Rojo, Energy & Environmental Science **5**, 5884 (2012).

[58] V. Palomares, M. Casas-Cabanas, E. Castillo-Martinez, M. H. Han, and T. Rojo, Energy & Environmental Science **6**, 2312 (2013).

[59] S.-W. Kim, D.-H. Seo, X. Ma, G. Ceder, and K. Kang, Advanced Energy Materials **2**, 710 (2012).

[60] M. S. Islam and C. A. J. Fisher, Chemical Society Reviews **43**, 185 (2014).

[61] B. L. Ellis and L. F. Nazar, Current Opinion in Solid State and Materials Science **16**, 168 (2012).

[62] M. H. Han, E. Gonzalo, G. Singh, and T. Rojo, Energy & Environmental Science **8**, 81 (2015).

[63] E. Irisarri, A. Ponrouch, and M. R. Palacin, Journal of The Electrochemical Society **162**, A2476 (2015).

[64] H. Kim, H. Kim, Z. Ding, M. H. Lee, K. Lim, G. Yoon, and K. Kang, Advanced Energy Materials (2016), 10.1002/aenm.201600943, available at `http://dx.doi.org/10.1002/aenm.201600943`.

[65] I. D. Gocheva, M. Nishijima, T. Doi, S. Okada, J.-i. Yamaki, and T. Nishida, Journal of Power Sources **187**, 247 (2009).

[66] M. Nishijima, I. D. Gocheva, S. Okada, T. Doi, J.-i. Yamaki, and T. Nishida, Journal of Power Sources **190**, 558 (2009).

[67] A. Kitajou, H. Komatsu, K. Chihara, I. D. Gocheva, S. Okada, and J. Yamaki, Journal of Power Sources **198**, 389 (2012).

[68] C. Delmas, C. Fouassier, and P. Hagenmuller, Physica B+C **99**, 81 (1980).

[69] X. Ma, H. Chen, and G. Ceder, Journal of The Electrochemical Society **158**, A1307 (2011).

[70] C.-Y. Yu, J.-S. Park, H.-G. Jung, K.-Y. Chung, D. Aurbach, Y.-K. Sun, and S.-T. Myung, Energy & Environmental Science **8**, 2019 (2015).

[71] X. Wang, G. Liu, T. Iwao, M. Okubo, and A. Yamada, The Journal of Physical Chemistry C **118**, 2970 (2014).

[72] E. de la Llave, V. Borgel, K.-J. Park, J.-Y. Hwang, Y.-K. Sun, P. Hartmann, F.-F. Chesneau, and D. Aurbach, ACS Applied Materials & Interfaces **8**, 1867 (2016).
[73] D. Kim, E. Lee, M. Slater, W. Lu, S. Rood, and C. S. Johnson, Electrochemistry Communications **18**, 66 (2012).
[74] N. Yabuuchi, M. Kajiyama, J. Iwatate, H. Nishikawa, S. Hitomi, R. Okuyama, R. Usui, Y. Yamada, and S. Komaba, Nature Materials **11**, 512 (2012).
[75] A. Caballero, L. Hernan, J. Morales, L. Sanchez, J. Santos Pena, and M. A. G. Aranda, Journal of Materials Chemistry **12**, 1142 (2002).
[76] H. Yoshida, N. Yabuuchi, K. Kubota, I. Ikeuchi, A. Garsuch, M. Schulz-Dobrick, and S. Komaba, Chemical Communications **50**, 3677 (2014).
[77] J. Xu, D. H. Lee, R. J. Clément, X. Yu, M. Leskes, A. J. Pell, G. Pintacuda, X.-Q. Yang, C. P. Grey, and Y. S. Meng, Chemistry of Materials **26**, 1260 (2014).
[78] J. Billaud, G. Singh, A. R. Armstrong, E. Gonzalo, V. Roddatis, M. Armand, T. Rojo, and P. G. Bruce, Energy & Environmental Science **7**, 1387 (2014).
[79] J. Kim, D.-H. Seo, H. Kim, I. Park, J.-K. Yoo, S.-K. Jung, Y.-U. Park, W. A. Goddard Iii, and K. Kang, Energy & Environmental Science **8**, 540 (2015).
[80] S.-M. Oh, S.-T. Myung, J. Hassoun, B. Scrosati, and Y.-K. Sun, Electrochemistry Communications **22**, 149 (2012).
[81] N. Anantharamulu, K. Koteswara Rao, G. Rambabu, B. Vijaya Kumar, V. Radha, and M. Vithal, Journal of Materials Science **46**, 2821 (2011).
[82] K. Saravanan, C. W. Mason, A. Rudola, K. H. Wong, and P. Balaya, Advanced Energy Materials **3**, 444 (2013).
[83] J. Liu, K. Tang, K. Song, P. A. van Aken, Y. Yu, and J. Maier, Nanoscale **6**, 5081 (2014).
[84] C. Zhu, K. Song, P. A. van Aken, J. Maier, and Y. Yu, Nano Letters **14**, 2175 (2014).
[85] R. A. Shakoor, D.-H. Seo, H. Kim, Y.-U. Park, J. Kim, S.-W. Kim, H. Gwon, S. Lee, and K. Kang, Journal of Materials Chemistry **22**, 20535 (2012).
[86] Y.-U. Park, D.-H. Seo, H.-S. Kwon, B. Kim, J. Kim, H. Kim, I. Kim, H.-I. Yoo, and K. Kang, Journal of the American Chemical Society **135**, 13870 (2013).
[87] P. Barpanda, G. Oyama, S.-i. Nishimura, S.-C. Chung, and A. Yamada, Nature Communications **5** (2014), 10.1038/ncomms5358.
[88] Y. Lu, L. Wang, J. Cheng, and J. B. Goodenough, Chemical Communications **48**, 6544 (2012).
[89] H.-W. Lee, R. Y. Wang, M. Pasta, S. Woo Lee, N. Liu, and Y. Cui, Nature Communications **5** (2014), 10.1038/ncomms6280.
[90] L. Wang, J. Song, R. Qiao, L. A. Wray, M. A. Hossain, Y.-D. Chuang, W. Yang, Y. Lu, D. Evans, J.-J. Lee, S. Vail, X. Zhao, M. Nishijima, S. Kakimoto, and J. B. Goodenough, Journal of the American Chemical Society **137**, 2548 (2015).

[91] L. Wang, Y. Lu, J. Liu, M. Xu, J. Cheng, D. Zhang, and J. B. Goodenough, Angewandte Chemie International Edition **52**, 1964 (2013).
[92] J. Song, L. Wang, Y. Lu, J. Liu, B. Guo, P. Xiao, J.-J. Lee, X.-Q. Yang, G. Henkelman, and J. B. Goodenough, Journal of the American Chemical Society **137**, 2658 (2015).
[93] Y. You, X.-L. Wu, Y.-X. Yin, and Y.-G. Guo, Energy & Environmental Science **7**, 1643 (2014).
[94] Y. You, X. Yu, Y. Yin, K.-W. Nam, and Y.-G. Guo, Nano Research **8**, 117 (2014).
[95] X. Wu, W. Deng, J. Qian, Y. Cao, X. Ai, and H. Yang, Journal of Materials Chemistry A **1**, 10130 (2013).
[96] A. Rudola, D. Aurbach, and P. Balaya, Electrochemistry Communications **46**, 56 (2014).
[97] S. Komaba, W. Murata, T. Ishikawa, N. Yabuuchi, T. Ozeki, T. Nakayama, A. Ogata, K. Gotoh, and K. Fujiwara, Advanced Functional Materials **21**, 3859 (2011).
[98] D. A. Stevens and J. R. Dahn, Journal of The Electrochemical Society **148**, A803 (2001).
[99] M. M. Doeff, Y. Ma, S. J. Visco, and L. C. De Jonghe, Journal of The Electrochemical Society **140**, L169 (1993).
[100] Y.-X. Wang, S.-L. Chou, H.-K. Liu, and S.-X. Dou, Carbon **57**, 202 (2013).
[101] Y. Wen, K. He, Y. Zhu, F. Han, Y. Xu, I. Matsuda, Y. Ishii, J. Cumings, and C. Wang, Nature Communications **5** (2014), 10.1038/ncomms5033.
[102] R. Alcantara, J. M. Jimenez-Mateos, P. Lavela, and J. L. Tirado, Electrochemistry Communications **3**, 639 (2001).
[103] P. Thomas and D. Billaud, Electrochimica Acta **46**, 39 (2000).
[104] D. Hamani, M. Ati, J.-M. Tarascon, and P. Rozier, Electrochemistry Communications **13**, 938 (2011).
[105] Z. Jian, L. Zhao, H. Pan, Y.-S. Hu, H. Li, W. Chen, and L. Chen, Electrochemistry Communications **14**, 86 (2012).
[106] P. Senguttuvan, G. l. Rousse, V. Seznec, J.-M. Tarascon, and M. R. Palac n, Chemistry of Materials **23**, 4109 (2011).
[107] D. Wu, X. Li, B. Xu, N. Twu, L. Liu, and G. Ceder, Energy & Environmental Science **8**, 195 (2015).
[108] A. Rudola, K. Saravanan, S. Devaraj, H. Gong, and P. Balaya, Chemical Communications **49**, 7451 (2013).
[109] P. Senguttuvan, G. Rousse, M. E. Arroyo y de Dompablo, H. Vezin, J. M. Tarascon, and M. R. Palac n, Journal of the American Chemical Society **135**, 3897 (2013).
[110] Y. Kim, Y. Park, A. Choi, N.-S. Choi, J. Kim, J. Lee, J. H. Ryu, S. M. Oh, and K. T. Lee, Advanced Materials **25**, 3045 (2013).
[111] J. Qian, X. Wu, Y. Cao, X. Ai, and H. Yang, Angewandte Chemie International Edition **52**, 4633 (2013).

[112] W.-J. Li, S.-L. Chou, J.-Z. Wang, H.-K. Liu, and S.-X. Dou, Nano Letters **13**, 5480 (2013).
[113] G.-L. Xu, Z. Chen, G.-M. Zhong, Y. Liu, Y. Yang, T. Ma, Y. Ren, X. Zuo, X.-H. Wu, X. Zhang, and K. Amine, Nano Letters **16**, 3955 (2016).
[114] J. Sun, H.-W. Lee, M. Pasta, H. Yuan, G. Zheng, Y. Sun, Y. Li, and Y. Cui, Nature Nanotechnology **10**, 980 (2015).
[115] K. P. S. S. Hembram, H. Jung, B. C. Yeo, S. J. Pai, S. Kim, K.-R. Lee, and S. S. Han, The Journal of Physical Chemistry C **119**, 15041 (2015).
[116] M. Mayo, K. J. Griffith, C. J. Pickard, and A. J. Morris, Chemistry of Materials **28**, 2011 (2016).
[117] K. Dai, H. Zhao, Z. Wang, X. Song, V. Battaglia, and G. Liu, Journal of Power Sources **263**, 276 (2014).
[118] Y. Liu, N. Zhang, L. Jiao, Z. Tao, and J. Chen, Advanced Functional Materials **25**, 340 (2015).
[119] J. W. Wang, X. H. Liu, S. X. Mao, and J. Y. Huang, Nano Letters **12**, 5897 (2012).
[120] L. D. Ellis, T. D. Hatchard, and M. N. Obrovac, Journal of The Electrochemical Society **159**, A1801 (2012).
[121] Z. Du, R. A. Dunlap, and M. N. Obrovac, Journal of Alloys and Compounds **617**, 271 (2014).
[122] J. Qian, Y. Chen, L. Wu, Y. Cao, X. Ai, and H. Yang, Chemical Communications **48**, 7070 (2012).
[123] A. Darwiche, C. Marino, M. T. Sougrati, B. Fraisse, L. Stievano, and L. Monconduit, Journal of the American Chemical Society **134**, 20805 (2012).
[124] L. Baggetto, P. Ganesh, C.-N. Sun, R. A. Meisner, T. A. Zawodzinski, and G. M. Veith, Journal of Materials Chemistry A **1**, 7985 (2013).
[125] P. K. Allan, J. M. Griffin, A. Darwiche, O. J. Borkiewicz, K. M. Wiaderek, K. W. Chapman, A. J. Morris, P. J. Chupas, L. Monconduit, and C. P. Grey, Journal of the American Chemical Society **138**, 2352 (2016).
[126] T. R. Jow, L. W. Shacklette, M. Maxfield, and D. Vernick, Journal of The Electrochemical Society **134**, 1730 (1987).
[127] L. D. Ellis, B. N. Wilkes, T. D. Hatchard, and M. N. Obrovac, Journal of The Electrochemical Society **161**, A416 (2014).
[128] D. Su, S. Dou, and G. Wang, Nano Energy **12**, 88 (2015).
[129] W. Xianming, T. Nishina, and I. Uchida, Journal of Power Sources **104**, 90 (2002).
[130] V. L. Chevrier and G. Ceder, Journal of The Electrochemical Society **158**, A1011 (2011).
[131] Y. Xu, E. Swaans, S. Basak, H. W. Zandbergen, D. M. Borsa, and F. M. Mulder, Advanced Energy Materials **6**, 00 (2016).
[132] P. R. Abel, Y.-M. Lin, T. de Souza, C.-Y. Chou, A. Gupta, J. B. Goodenough, G. S. Hwang, A. Heller, and C. B. Mullins, The Journal of Physical Chemistry C **117**, 18885 (2013).

[133] L. Baggetto, J. K. Keum, J. F. Browning, and G. M. Veith, Electrochemistry Communications **34**, 41 (2013).
[134] Y.-M. Lin, P. R. Abel, A. Gupta, J. B. Goodenough, A. Heller, and C. B. Mullins, ACS Applied Materials & Interfaces **5**, 8273 (2013).
[135] L. Baggetto, M. Marszewski, J. Gorka, M. Jaroniec, and G. M. Veith, Journal of Power Sources **243**, 699 (2013).
[136] L. Baggetto, E. Allcorn, R. R. Unocic, A. Manthiram, and G. M. Veith, Journal of Materials Chemistry A **1**, 11163 (2013).
[137] L. Baggetto, E. Allcorn, A. Manthiram, and G. M. Veith, Electrochemistry Communications **27**, 168 (2013).
[138] D.-H. Nam, K.-S. Hong, S.-J. Lim, and H.-S. Kwon, Journal of Power Sources **247**, 423 (2014).
[139] Y. Kim, Y. Kim, A. Choi, S. Woo, D. Mok, N.-S. Choi, Y. S. Jung, J. H. Ryu, S. M. Oh, and K. T. Lee, Advanced Materials **26**, 4139 (2014).
[140] W. Li, S.-L. Chou, J.-Z. Wang, J. H. Kim, H.-K. Liu, and S.-X. Dou, Advanced Materials **26**, 4037 (2014).
[141] J. Qian, Y. Xiong, Y. Cao, X. Ai, and H. Yang, Nano Letters **14**, 1865 (2014).
[142] L. Xiao, Y. Cao, J. Xiao, W. Wang, L. Kovarik, Z. Nie, and J. Liu, Chemical Communications **48**, 3321 (2012).
[143] A. Darwiche, M. T. Sougrati, B. Fraisse, L. Stievano, and L. Monconduit, Electrochemistry Communications **32**, 18 (2013).
[144] L. Ji, M. Gu, Y. Shao, X. Li, M. H. Engelhard, B. W. Arey, W. Wang, Z. Nie, J. Xiao, C. Wang, J.-G. Zhang, and J. Liu, Advanced Materials **26**, 2901 (2014).
[145] Y. Zhao and A. Manthiram, Chemistry of Materials **27**, 3096 (2015).
[146] F. Klein, B. Jache, A. Bhide, and P. Adelhelm, Physical Chemistry Chemical Physics **15**, 15876 (2013).
[147] Y. Oumellal, A. Rougier, G. A. Nazri, J. M. Tarascon, and L. Aymard, Nature Materials **7**, 916 (2008).
[148] Y. Jiang, M. Hu, D. Zhang, T. Yuan, W. Sun, B. Xu, and M. Yan, Nano Energy **5**, 60 (2014).
[149] S. Hariharan, K. Saravanan, and P. Balaya, Electrochemistry Communications **31**, 5 (2013).
[150] J.-W. Lee, H.-S. Shin, C.-W. Lee, and K.-N. Jung, Nanoscale Research Letters **11**, 1 (2016).
[151] P. R. Kumar, Y. H. Jung, K. K. Bharathi, C. H. Lim, and D. K. Kim, Electrochimica Acta **146**, 503 (2014).
[152] Y. Liu, N. Zhang, C. Yu, L. Jiao, and J. Chen, Nano Letters **16**, 3321 (2016).
[153] T. B. Kim, J. W. Choi, H. S. Ryu, G. B. Cho, K. W. Kim, J. H. Ahn, K. K. Cho, and H. J. Ahn, Journal of Power Sources **174**, 1275 (2007).
[154] J.-S. Kim, G.-B. Cho, K.-W. Kim, J.-H. Ahn, G. Wang, and H.-J. Ahn, Current Applied Physics **11**, S215 (2011).

[155] C. Zhu, X. Mu, P. A. van Aken, Y. Yu, and J. Maier, Angewandte Chemie International Edition **53**, 2152 (2014).
[156] D. Su, S. Dou, and G. Wang, Chemical Communications **50**, 4192 (2014).
[157] J. Fullenwarth, A. Darwiche, A. Soares, B. Donnadieu, and L. Monconduit, Journal of Materials Chemistry A **2**, 2050 (2014).
[158] C. Nithya, ChemPlusChem **80**, 1000 (2015).
[159] W. Sun, X. Rui, D. Zhang, Y. Jiang, Z. Sun, H. Liu, and S. Dou, Journal of Power Sources **309**, 135 (2016).
[160] Q. Sun, Q.-Q. Ren, H. Li, and Z.-W. Fu, Electrochemistry Communications **13**, 1462 (2011).
[161] D. Y. W. Yu, P. V. Prikhodchenko, C. W. Mason, S. K. Batabyal, J. Gun, S. Sladkevich, A. G. Medvedev, and O. Lev, Nature Communications **4** (2013), 10.1038/ncomms3922.
[162] D. Su, H.-J. Ahn, and G. Wang, Chemical Communications **49**, 3131 (2013).
[163] Y. Zhang, P. Zhu, L. Huang, J. Xie, S. Zhang, G. Cao, and X. Zhao, Advanced Functional Materials **25**, 481 (2015).
[164] Y. Zheng, T. Zhou, C. Zhang, J. Mao, H. Liu, and Z. Guo, Angewandte Chemie **128**, 3469 (2016).
[165] P. P. R. M. L. Harks, F. M. Mulder, and P. H. L. Notten, Journal of Power Sources **288**, 92 (2015).
[166] J. Nelson Weker and M. F. Toney, Advanced Functional Materials **25**, 1622 (2015).
[167] V. K. Peterson and C. M. Papadakis, IUCrJ **2**, 292 (2015).
[168] N. Sharma, W. K. Pang, Z. Guo, and V. K. Peterson, ChemSusChem **8**, 2826 (2015).
[169] S. F. Amalraj and D. Aurbach, Journal of Solid State Electrochemistry **15**, 877 (2011).
[170] R. De Marco and J.-P. Veder, TrAC Trends in Analytical Chemistry **29**, 528 (2010).
[171] J. McBreen, Journal of Solid State Electrochemistry **13**, 1051 (2008).
[172] M. Morcrette, Y. Chabre, G. Vaughan, G. Amatucci, J. B. Leriche, S. Patoux, C. Masquelier, and J. M. Tarascon, Electrochimica Acta **47**, 3137 (2002).
[173] P. Novak, J. C. Panitz, F. Joho, M. Lanz, R. Imhof, and M. Coluccia, Journal of Power Sources **90**, 52 (2000).
[174] X. Zhang, M. van Hulzen, D. P. Singh, A. Brownrigg, J. P. Wright, N. H. van Dijk, and M. Wagemaker, Nano Letters **14**, 2279 (2014).
[175] X. Zhang, M. van Hulzen, D. P. Singh, A. Brownrigg, J. P. Wright, N. H. van Dijk, and M. Wagemaker, Nature Communications **6**, 8333 (2015).
[176] J.-L. Shui, J. S. Okasinski, P. Kenesei, H. A. Dobbs, D. Zhao, J. D. Almer, and D.-J. Liu, Nature Communications **4**, 2255 (2013).
[177] S. Ganapathy, J. R. Heringa, M. S. Anastasaki, B. D. Adams, M. van Hulzen, S. Basak, Z. Li, J. P. Wright, L. F. Nazar, N. H. van Dijk, and M. Wagemaker, The Journal of Physical Chemistry Letters **7**, 3388 (2016).

[178] O. J. Borkiewicz, B. Shyam, K. M. Wiaderek, C. Kurtz, P. J. Chupas, and K. W. Chapman, Journal of Applied Crystallography **45**, 1261 (2012).
[179] K. Yamamoto, T. Minato, S. Mori, D. Takamatsu, Y. Orikasa, H. Tanida, K. Nakanishi, H. Murayama, T. Masese, T. Mori, H. Arai, Y. Koyama, Z. Ogumi, and Y. Uchimoto, The Journal of Physical Chemistry C **118**, 9538 (2014).
[180] M. Giorgetti, ISRN Materials Science **2013**, 22 (2013).
[181] A. Deb, U. Bergmann, S. P. Cramer, and E. J. Cairns, Journal of The Electrochemical Society **154**, A534 (2007).
[182] P. Bleith, W. van Beek, H. Kaiser, P. Novák, and C. Villevieille, The Journal of Physical Chemistry C **119**, 3466 (2015).
[183] D. Lv, J. Bai, P. Zhang, S. Wu, Y. Li, W. Wen, Z. Jiang, J. Mi, Z. Zhu, and Y. Yang, Chemistry of Materials **25**, 2014 (2013).
[184] A. Ito, Y. Sato, T. Sanada, M. Hatano, H. Horie, and Y. Ohsawa, Journal of Power Sources **196**, 6828 (2011).
[185] R. Dominko, I. Arcon, A. Kodre, D. Hanzel, and M. Gaberscek, Journal of Power Sources **189**, 51 (2009).
[186] S. Permien, S. Indris, U. Schürmann, L. Kienle, S. Zander, S. Doyle, and W. Bensch, Chemistry of Materials **28**, 434 (2016).
[187] Y.-Y. Hu, Z. Liu, K.-W. Nam, O. J. Borkiewicz, J. Cheng, X. Hua, M. T. Dunstan, X. Yu, K. M. Wiaderek, L.-S. Du, K. W. Chapman, P. J. Chupas, X.-Q. Yang, and C. P. Grey, Nature Materials **12**, 1130 (2013).
[188] M. A. Lowe, J. Gao, and H. D. Abruna, Journal of Materials Chemistry A **1**, 2094 (2013).
[189] F. Blanc, M. Leskes, and C. P. Grey, Accounts of Chemical Research **46**, 1952 (2013).
[190] K. Ogata, E. Salager, C. J. Kerr, A. E. Fraser, C. Ducati, A. J. Morris, S. Hofmann, and C. P. Grey, Nature Communications **5**, 3217 (2014).
[191] K. M. Wiaderek, O. J. Borkiewicz, N. Pereira, J. Ilavsky, G. G. Amatucci, P. J. Chupas, and K. W. Chapman, Journal of the American Chemical Society **136**, 6211 (2014).
[192] D. H. Lee, K. J. Carroll, K. W. Chapman, O. J. Borkiewicz, S. Calvin, E. E. Fullerton, and Y. S. Meng, Physical Chemistry Chemical Physics **16**, 3095 (2014).
[193] M. Ebner, F. Marone, M. Stampanoni, and V. Wood, Science **342**, 716 (2013).
[194] J. N. Weker, N. Liu, S. Misra, J. C. Andrews, Y. Cui, and M. F. Toney, Energy & Environmental Science **7**, 2771 (2014).
[195] F. Yang, Y. Liu, S. K. Martha, Z. Wu, J. C. Andrews, G. E. Ice, P. Pianetta, and J. Nanda, Nano Letters **14**, 4334 (2014).
[196] J. Wang, Y.-C. K. Chen-Wiegart, and J. Wang, Nature Communications **5**, 4570 (2014).
[197] Y.-S. Yu, C. Kim, Y. Liu, A. van der Ven, Y. S. Meng, R. Kostecki, and J. Cabana, Advanced Energy Materials **5**, 1402040 (2015).

[198] K. M. O. Jensen, X. H. Yang, J. V. Laveda, W. G. Zeier, K. A. See, M. Di Michiel, B. C. Melot, S. A. Corr, and S. J. L. Billinge, Journal of the Electrochemical Society **162**, A1310 (2015).
[199] S. D. M. Jacques, M. Di Michiel, A. M. Beale, T. Sochi, M. G. O'Brien, L. Espinosa-Alonso, B. M. Weckhuysen, and P. Barnes, Angewandte Chemie International Edition **50**, 10148 (2011).
[200] S. D. M. Jacques, M. Di Michiel, S. A. J. Kimber, X. Yang, R. J. Cernik, A. M. Beale, and S. J. L. Billinge, Nature Communications **4**, 2536 (2013).
[201] A. Ulvestad, A. Singer, H.-M. Cho, J. N. Clark, R. Harder, J. Maser, Y. S. Meng, and O. G. Shpyrko, Nano Letters **14**, 5123 (2014).
[202] A. Ulvestad, H. M. Cho, R. Harder, J. W. Kim, S. H. Dietze, E. Fohtung, Y. S. Meng, and O. G. Shpyrko, Applied Physics Letters **104**, 073108 (2014).
[203] A. Ulvestad, A. Singer, J. N. Clark, H. M. Cho, J. W. Kim, R. Harder, J. Maser, Y. S. Meng, and O. G. Shpyrko, Science **348**, 1344 (2015).
[204] M. Gu, L. R. Parent, B. L. Mehdi, R. R. Unocic, M. T. McDowell, R. L. Sacci, W. Xu, J. G. Connell, P. Xu, P. Abellan, X. Chen, Y. Zhang, D. E. Perea, J. E. Evans, L. J. Lauhon, J.-G. Zhang, J. Liu, N. D. Browning, Y. Cui, I. Arslan, and C.-M. Wang, Nano Letters **13**, 6106 (2013).
[205] J. Y. Huang, L. Zhong, C. M. Wang, J. P. Sullivan, W. Xu, L. Q. Zhang, S. X. Mao, N. S. Hudak, X. H. Liu, A. Subramanian, H. Fan, L. Qi, A. Kushima, and J. Li, Science **330**, 1515 (2010).
[206] X. H. Liu, H. Zheng, L. Zhong, S. Huang, K. Karki, L. Q. Zhang, Y. Liu, A. Kushima, W. T. Liang, J. W. Wang, J.-H. Cho, E. Epstein, S. A. Dayeh, S. T. Picraux, T. Zhu, J. Li, J. P. Sullivan, J. Cumings, C. Wang, S. X. Mao, Z. Z. Ye, S. Zhang, and J. Y. Huang, Nano Letters **11**, 3312 (2011).
[207] X. H. Liu, L. Zhong, S. Huang, S. X. Mao, T. Zhu, and J. Y. Huang, ACS Nano **6**, 1522 (2012).
[208] Z. Xie, Z. Ma, Y. Wang, Y. Zhou, and C. Lu, RSC Advances **6**, 22383 (2016).
[209] M. E. Holtz, Y. Yu, D. Gunceler, J. Gao, R. Sundararaman, K. A. Schwarz, T. A. Arias, H. D. Abruña, and D. A. Muller, Nano Letters **14**, 1453 (2014).
[210] A. L. Michan, M. Leskes, and C. P. Grey, Chemistry of Materials **28**, 385 (2016).
[211] A. L. Michan, G. Divitini, A. J. Pell, M. Leskes, C. Ducati, and C. P. Grey, Journal of the American Chemical Society **138**, 7918 (2016).
[212] Z. Wang, D. Santhanagopalan, W. Zhang, F. Wang, H. L. Xin, K. He, J. Li, N. Dudney, and Y. S. Meng, Nano Letters **16**, 3760 (2016).
[213] *International Tables for Crystallography*, 5th ed., SPACE-GROUP SYMMETRY (Springer, Dordrecht, The Netherlands, 2005).
[214] R. E. Dinnebier and S. J. L. Billinge, *Powder Diffraction - Theory and Practice*, edited by R. E. Dinnebier and S. J. L. Billinge (Royal Society of Chemistry, Cambridge, UK, 2008).
[215] A. Coelho, *Users Manual - Topas Academic*, Manual (2007) available at `http://www.topas-academic.net/Technical_Reference.pdf`.

[216] H. Rietveld, Journal of Applied Crystallography **2**, 65 (1969).
[217] P. Norby, Current Opinion in Colloid & Interface Science **11**, 118 (2006).
[218] R. I. Walton and D. O'Hare, Chemical Communications , 2283 (2000).
[219] R. J. Francis and D. O'Hare, Journal of the Chemical Society, Dalton Transactions , 3133 (1998).
[220] J. Munn, P. Barnes, D. Häusermann, S. A. Axon, and J. Klinowski, Phase Transitions **39**, 129 (1992).
[221] G. W. Stinton and J. S. O. Evans, Journal of Applied Crystallography **40**, 87 (2007).
[222] J. E. Penner-Hahn, "X-ray absorption spectroscopy," in *Comprehensive Coordination Chemistry II*, edited by T. J. Meyer (Pergamon, Oxford, 2003) pp. 159–186.
[223] G. Bunker, *Introduction to XAFS - A Practical Guide to X-ray Absorption Fine Structure Spectroscopy* (Cambridge University Press, New York, 2010).
[224] T. Yamamoto, X-Ray Spectrometry **37**, 572 (2008).
[225] P. B. Samarasingha, N. H. Andersen, M. H. Sørby, S. Kumar, O. Nilsen, and H. Fjellv g, Solid State Ionics **284**, 28 (2016).
[226] A. Kayyar, J. Huang, M. Samiee, and J. Luo, Journal of Visualized Experiments , e4104 (2012).
[227] S. Grazulis, D. Chateigner, R. T. Downs, A. F. T. Yokochi, M. Quiros, L. Lutterotti, E. Manakova, J. Butkus, P. Moeck, and A. Le Bail, Journal of Applied Crystallography **42**, 726 (2009).
[228] B. Ravel and M. Newville, Journal of Synchrotron Radiation **12**, 537 (2005).
[229] C. Villevieille, T. Sasaki, and P. Novak, RSC Advances **4**, 6782 (2014).
[230] M. Herklotz, F. Scheiba, M. Hinterstein, K. Nikolowski, M. Knapp, A.-C. Dippel, L. Giebeler, J. Eckert, and H. Ehrenberg, Journal of Applied Crystallography **46**, 1117 (2013).
[231] O. J. Borkiewicz, K. M. Wiaderek, P. J. Chupas, and K. W. Chapman, The Journal of Physical Chemistry Letters **6**, 2081 (2015).
[232] M. Herklotz, J. Weiss, E. Ahrens, M. Yavuz, L. Mereacre, N. Kiziltas-Yavuz, C. Drager, H. Ehrenberg, J. Eckert, F. Fauth, L. Giebeler, and M. Knapp, Journal of Applied Crystallography **49**, 340 (2016).
[233] Y. Moritomo, M. Takachi, Y. Kurihara, and T. Matsuda, Advances in Materials Science and Engineering **2013**, 17 (2013).
[234] D. P. Finegan, M. Scheel, J. B. Robinson, B. Tjaden, I. Hunt, T. J. Mason, J. Millichamp, M. Di Michiel, G. J. Offer, G. Hinds, D. J. L. Brett, and P. R. Shearing, Nature Communications **6** (2015), 10.1038/ncomms7924.
[235] M. Hu, X. Pang, and Z. Zhou, Journal of Power Sources **237**, 229 (2013).
[236] T.-F. Yi, J. Mei, and Y.-R. Zhu, Journal of Power Sources **316**, 85 (2016).
[237] Z. Moorhead-Rosenberg, A. Huq, J. B. Goodenough, and A. Manthiram, Chemistry of Materials **27**, 6934 (2015).
[238] J. Xiao, X. Chen, P. V. Sushko, M. L. Sushko, L. Kovarik, J. Feng, Z. Deng, J. Zheng, G. L. Graff, Z. Nie, D. Choi, J. Liu, J.-G. Zhang, and M. S. Whittingham, Advanced Materials **24**, 2109 (2012).

[239] J. Yoon, D. Kim, J. H. Um, M. Jeong, W. Oh, and W. S. Yoon, Journal of Alloys and Compounds **686**, 593 (2016).
[240] H. Duncan, B. Hai, M. Leskes, C. P. Grey, and G. Chen, Chemistry of Materials **26**, 5374 (2014).
[241] S. Choi, J. Yoon, S. Muhammad, and W. S. Yoon, Journal of Electrochemical Science and Technology **4**, 34 (2013).
[242] B. Hai, A. K. Shukla, H. Duncan, and G. Chen, Journal of Materials Chemistry A **1**, 759 (2013).
[243] J. Zheng, J. Xiao, X. Yu, L. Kovarik, M. Gu, F. Omenya, X. Chen, X.-Q. Yang, J. Liu, G. L. Graff, M. S. Whittingham, and J.-G. Zhang, Physical Chemistry Chemical Physics **14**, 13515 (2012).
[244] L. Wang, H. Li, X. Huang, and E. Baudrin, Solid State Ionics **193**, 32 (2011).
[245] K. Rhodes, R. Meisner, Y. Kim, N. Dudney, and C. Daniel, Journal of The Electrochemical Society **158**, A890 (2011).
[246] M. Kunduraci and G. G. Amatucci, Journal of The Electrochemical Society **153**, A1345 (2006).
[247] M. Kunduraci, J. F. Al-Sharab, and G. G. Amatucci, Chemistry of Materials **18**, 3585 (2006).
[248] H. Komatsu, H. Arai, Y. Koyama, K. Sato, T. Kato, R. Yoshida, H. Murayama, I. Takahashi, Y. Orikasa, K. Fukuda, T. Hirayama, Y. Ikuhara, Y. Ukyo, Y. Uchimoto, and Z. Ogumi, Advanced Energy Materials **5**, 1500638 (2015).
[249] M. Lin, L. Ben, Y. Sun, H. Wang, Z. Yang, L. Gu, X. Yu, X.-Q. Yang, H. Zhao, R. Yu, M. Armand, and X. Huang, Chemistry of Materials **27**, 292 (2015).
[250] J. Rana, S. Glatthaar, H. Gesswein, N. Sharma, J. R. Binder, R. Chernikov, G. Schumacher, and J. Banhart, Journal of Power Sources **255**, 439 (2014).
[251] H. Kawaura, D. Takamatsu, S. Mori, Y. Orikasa, H. Sugaya, H. Murayama, K. Nakanishi, H. Tanida, Y. Koyama, H. Arai, Y. Uchimoto, and Z. Ogumi, Journal of Power Sources **245**, 816 (2014).
[252] U. Lafont, C. Locati, W. J. H. Borghols, A. Łasińska, J. Dygas, A. V. Chadwick, and E. M. Kelder, Journal of Power Sources **189**, 179 (2009).
[253] S. Mukerjee, X. Q. Yang, X. Sun, S. J. Lee, J. McBreen, and Y. Ein-Eli, Electrochimica Acta **49**, 3373 (2004).
[254] W. Zhu, D. Liu, J. Trottier, C. Gagnon, A. Guerfi, C. M. Julien, A. Mauger, and K. Zaghib, Journal of Power Sources **264**, 290 (2014).
[255] W. Zhu, D. Liu, J. Trottier, P. Hovington, C. Gagnon, A. Guerfi, K. Zaghib, A. Mauger, H. Groult, and C. M. Julien, in *ECS Transactions*, Vol. 58, pp. 35–40.
[256] S. Komaba, Y. Matsuura, T. Ishikawa, N. Yabuuchi, W. Murata, and S. Kuze, Electrochemistry Communications **21**, 65 (2012).
[257] F. Legrain, O. I. Malyi, and S. Manzhos, Computational Materials Science **94**, 214 (2014).

[258] S. C. Jung, D. S. Jung, J. W. Choi, and Y.-K. Han, The Journal of Physical Chemistry Letters **5**, 1283 (2014).
[259] Q. Zhao, Y. Huang, and X. Hu, Electrochemistry Communications **70**, 8 (2016).
[260] C.-H. Lim, T.-Y. Huang, P.-S. Shao, J.-H. Chien, Y.-T. Weng, H.-F. Huang, B. J. Hwang, and N.-L. Wu, Electrochimica Acta **211**, 265 (2016).
[261] M. Shimizu, H. Usui, K. Fujiwara, K. Yamane, and H. Sakaguchi, Journal of Alloys and Compounds **640**, 440 (2015).
[262] G. Gourdin, P. H. Smith, T. Jiang, T. N. Tran, and D. Qu, Journal of Electroanalytical Chemistry **688**, 103 (2013).